Filopodia-independent roles of the actin bundling protein fascin in promoting cell motility

HARVARD UNIVERSITY
Graduate School of Arts and Sciences

DISSERTATION ACCEPTANCE CERTIFICATE

The undersigned, appointed by the

Department of Molecular and Cellular Biology

have examined a dissertation entitled

"Filopodia-independent roles of the actin bundling protein fascin in promoting cell motility"

presented by Youbean Oak,

candidate for the degree of Doctor of Philosophy and hereby

certify that it is worthy of acceptance.

Signature _____

Typed name: Prof. Jeff Lichtman

Signature _____

Typed name: Prof. Daniel Needleman

Signature _____

Typed name: Prof. Jagesh Shah

Date: August 21, 2014

Filopodia-independent roles of the actin bundling protein fascin in promoting cell motility

A dissertation presented by

Youbean Oak

to

The Department of Molecular and Cellular Biology

in partial fulfilment of the requirements

for the degree of

Doctor of Philosophy

in the subject of

Biology

Harvard University

Cambridge, Massachusetts

August 2014

Dissertation Advisor: Professor Gaudenz Danuser Youbean Oak

Filopodia-independent roles of the actin bundling protein fascin in promoting cell motility

Abstract

Fascin is an actin bundling protein whose overexpression has in recent years been systematically linked to increased metastasis and poor outcome in cancer patients. It is well established that fascin expression correlates with enhanced cell migration; however, the underlying mechanisms are poorly understood. We combined various methods of high-resolution live cell imaging and computational analysis to investigate the role of fascin in increasing cell motility. We found that fascin promotes collective migration in normal epithelial cells and that this behavior is in agreement with protrusive activities at the single cell level. Traction force measurements indicated that fascin expression level is negatively correlated with traction stress levels and that a cell expressing high levels of fascin protrudes over longer distances than cells with lower levels. Together this led to the hypothesis that fascin distributes cell traction more efficiently, which lowers the load on individual adhesions and actin filaments growing against increasing membrane tension during one protrusion cycle. Measurements of adhesion formation and maturation indicate that fascin expression indeed promotes nascent adhesion formation over a wide area behind the leading edge. In metastatic cells with high fascin expression, we observed decreased invasion upon fascin knock down. These observations demonstrate a role for fascin in promoting cell motility in normal and neoplastic cells, in part by templating nascent adhesions at the leading edge.

Table of contents

Acknowledgements

I am deeply indebted to many people for helping me academically and emotionally during the long journey that is graduate school. First of all, I would like to express my gratitude to Dr. Gaudenz Danuser for giving me the chance to work with such exceptional people in his lab and for his mentoring over the years. I have learned so much from him both professionally and personally, and the lessons learned in his lab will have lasting impact on my future career.

In addition, I would like to thank my committee members—Drs. Jeffrey Lichtman, Daniel Needleman, and Jagesh Shah—for their valuable time and advice throughout my time at the Danuser lab. The feedback I received during my meetings with them were instrumental in pushing the project forward. I especially thank them for always being responsive to email communication and for never being too busy to meet with me individually.

I also had people around me from whom I could seek daily advice. Dr. Kwonmoo Lee not only provided direction for the project but also helped me with much of the coding and experimental protocols. He has been a great mentor, and for that I thank him. In addition, I thank Dr. Alexis Lomakin for making lab life a lot more interesting and Dr. Christoph Buckhardt for tirelessly pointing me toward reagents I always seem to be searching for.

I would be remiss if I didn't mention the multitude of support from friends and family, both far and near. In particular, I thank Angela, Caroline, Haegi, and Hyunkyu for being just a phone call or an email away, for listening when I needed to talk, and for worrying about me. I thank my parents for being my biggest supporters and for giving me the confidence to work towards anything I really want.

Lastly, I thank John Lee for sticking with me even when I thought all was lost. Over the past nine years, he has taught me through example so much about patience, selflessness, love, and other qualities of a "good" human being that I did not give much thought to in my early 20s. The idea of going on many more journeys, overcoming many more life obstacles, and discovering life together still excites me every day.

Introduction

Despite the promises and hopes of the Human Genome Project, cancer continues to be a leading cause of death in this post-genomic era. In fact, in 2012 alone, cancer accounted for 8.2 million deaths worldwide (World Health Organization, 2014). The cause of death for nearly 90% of cancer patients is not the primary tumor itself but rather metastasis to distant organs (Mehlen and Puisieux, 2006; Nguyen et al., 2009). As such, much research, both in academic institutions as well as industry, has focused on genomics and expression profiling of cancer cells with the hope of pinpointing precisely the gene or gene set that promotes metastasis such that targetable pathways might be identified. Despite such efforts, the tools of genomics have not been able to completely solve the "metastasis problem." One reason for this is the genetic heterogeneity of neoplastic cells. As an illustrative example, a 2004 study explored the diversity in morphology, immunophenotype, and gene expression from 30 autopsies of men who died of prostate cancer; the observed phenotypic and genetic diversity led the authors to conclude that metastasis is not a single disease but a group of diseases, even within the same patient (Shah et al., 2004).

Another reason genomics has not been able to eradicate cancer is a result of an incomplete comprehension of its biological nature. Even if genetic homogeneity does exist, this does not automatically translate to complete understanding of the cellular/molecular consequences. For example, mutations that constitutively activate K-Ras are found in almost all pancreatic ductal adenocarcinomas (PDAC), but PDAC remains one of the most fatal cancers (Kanda et al., 2012; Morris et al., 2010). It is known that when activated, K-Ras is involved in cellular pathways that promote proliferation, survival, and migration among others (Rodriguez-Viciana et al., 2005), but the exact spectrum of cell biological consequences of having all K-Ras constitutively active

is not clear. Notwithstanding such genetic diversity and an unclear link between genomics and mechanism, however, there remains functional homogeneity at the cellular level that unifies the "group of diseases" that is metastasis. Metastasis at its core requires 1) invasion of cells from primary tumor into the circulatory system, 2) extravasation at a distant site, and 3) survival of a new colony through changes in the microenvironment and angiogenesis (Birchmeier et al., 2003; Mehlen and Puisieux, 2006; Nguyen et al., 2009).

Cancer and cell motility

From the cell biologist's point view, metastasis, especially the initial step of invasion, is an immensely interesting problem. Invasion necessarily means that one or a group of cells in the original tumor becomes more motile as it/they move through the adjacent tissue and into a blood or lymph vessel by penetrating one or more basement membranes and endothelial walls (Birchmeier et al., 2003; Mehlen and Puisieux, 2006). In other words, a characteristic of the early metastatic tumor cells is the acquisition of autonomous motile properties. Various modes of cancer cell motility have been identified by both *in vitro* and *in vivo* observations (Enterline and Coman, 1950; Farina et al., 1998). Cancer cells may move as single cells, known as "individual cell migration," and this is especially characteristic of leukemias, lymphomas, and sarcomas. This mode of migration can be further segmented into *mesenchymal migration* and *amoeboid migration* (Friedl and Wolf, 2003; Yilmaz and Christofori, 2010). Mesenchymal migration is characterized by elongated, fibroblast-like cells that interact with the extracellular matrix (ECM) through focalized integrins and proteases and generates high traction forces. Such cells have relatively low rates of migration at 0.1-2 μm/min in 3D culture models (Friedl et al., 1998). Amoeboid migration, on the other hand, is characterized by round or ellipsoid cells that are

highly deformable and less adhesive due to having short-lived weak interactions with the ECM (Yilmaz and Christofori, 2010). These cells squeeze through the ECM rather than reorganizing or degrading it and can move much faster than cells using the mesenchymal migration mechanisms, up to 20 μm/min (Friedl et al., 2001).

Another mode of cancer cell dissemination is "collective migration" in which a group of cells move together in sheets, streams, or clusters (Friedl and Wolf, 2003; Yilmaz and Christofori, 2010). Collective migration is commonly seen in epithelial tumors. A group of collectively migrating cells are often composed of "leader cells" or "path-generating cells" that form active protrusions and degrade the ECM with metalloproteases and "follower cells" that are passively dragged (Friedl and Wolf, 2003). Interestingly, many tumors use both collective migration and individual cell migration simultaneously to disseminate. Additionally, epithelial tumor cells can undergo a transition in which they convert from relying on collective migration mechanisms to using single-cell migration mechanisms (Pankova et al., 2010). This is a part of epithelial-mesenchymal transition (EMT), in which epithelial cells lose the characteristic terminally differentiated phenotype and shift to a fibroblast-like, migratory phenotype. EMT increases the individual cell motility through changes in a host of signaling programs that cause the cell to lose cell-cell adhesions and its apical-basal polarity as well as reorganizing the cytoskeleton (Kong et al., 2011; Thiery, 2002). With EMT, tumors can now send out single cells to colonize other tissues or organs, which increases metastasis and worsens prognosis for patients (Moll et al., 1993; Thiery, 2002).

Although cell motility is a key feature of metastasis, it is not a property of cells that is uniquely associated with cancer cells. In fact, cell biologists have studied this process for eons, as it is a

vitally essential feature of physiological processes: In development, cells undergo a drastic spatial reorganization during gastrulation as a simple spherical ball of cells becomes a multi-layered gastrula with three germ layers. In fact, EMT has been a recognized feature of embryogenesis (especially gastrulation) since the 1980s (Greenburg and Hay, 1982). Migration continues to be important in later stages of development. For instance, the precise wiring of the neural circuitry depends on developing neurons that use growth cones to establish the direction of axonal elongation and propagate in that direction (Dent et al., 2011). Once born, an organism will no doubt be infected by microbes or be physically injured. When this occurs, the immune system reacts by activating macrophages that respond to the chemoattractant signals and migrate towards the site of injury or invasion (Sanchez-Madrid and Angel del Pozo, 1999; Stark et al., 1998). Moreover, the final steps of wound healing rely on the ability of epithelial cells to migrate across the newly formed tissue and ultimately meet in the middle to close the wound.

Given that many such interesting and crucial phenomena of life involve a form of cell motility, cell biologists have expended copious energy and time to characterize it. As with any other biological phenomena, it is a process we do not yet completely understand, but it is one we have been able to characterize in some detail as described in the next sections.

Actin and actin structures

What is the feature of a cell that allows for such dynamic remodeling of cell shape and polarity as a cell moves through its microenvironment? The advent of optical microscopy and the use of clever model systems have allowed us to determine that it is in fact the actin cytoskeleton responsible for this phenomenon, rather than directed lipid flow or microtubules (Mitchison and

Cramer, 1996). Actin is the most abundant protein in most eukaryotic cells (Pollard, 2007). The 42-kD protein is highly conserved and participates in more protein-protein interactions than any known protein (Dominguez and Holmes, 2011). As such, it plays a key role not only in cell motility but also in cell shape and polarity maintenance and even transcription regulation.

A characteristic feature of actin that allows it to carry out its functions, especially in cell motility, is the continuous turnover of subunits between monomeric (G-actin) and filamentous (F-actin) forms. This enables a rapid (on a time scale of tens of seconds) adaptation of the actin cytoskeleton structure and cell morphogenesis to motile cues. The constant state of flux is mediated by the fact that F-actin is an effective ATPase while G-actin is not, which results in the addition of ATP-bound actin monomers to the barbed (+) end of actin filaments and subtraction of ADP-bound actin monomers at the pointed (-) end. The state of constant polymerization at one end of filaments and depolymerization at the other end creates a phenomenon is known as actin filament treadmilling. This is in contrast to microtubules in which both addition and subtraction of subunits occur at the same end of the polymer. Unlike actin filaments, microtubules grow and shrink by switching between two states—stably growing and rapidly shrinking—in a state known as dynamic instability (Mitchison and Kirschner, 1984).

The limiting step in the kinetics of actin filament assembly is the nucleation step in which actin dimers and trimers are formed. Assembly itself can occur as fast as 3,000 subunits/second at the barbed end, meaning that a length relevant to the length scale of a cell (~10 μm) can be reached in less than 2 seconds(Pollard et al., 2000). Depending on the balance of polymerization and depolymerization as mediated by nucleotide hydrolysis, ions (such as calcium and magnesium), and particularly by a large number of actin binding proteins, the actin cytoskeleton can push the

cell membrane with enough force to deform the plasma membrane (Condeelis, 1993; Cramer et al., 1994; Marcy et al., 2004; Mitchison and Cramer, 1996; Mogilner and Oster, 1996a). Creating these protrusions is the necessary first step for the eventual cell translocation.

Two major types of actin networks exist in the cell, and this is dependent on how individual filaments are structured in relation to each other. Branched networks are best described as a collection of short actin filaments that resemble a very dense web, especially at the cell front (Svitkina et al., 1997; Svitkina and Borisy, 1999). Actin bundles can be either parallel, meaning that all the barbed ends of all filaments point toward the same end, or they can be made up of filaments of mixed polarities (Fletcher and Mullins, 2010). The type of actin network present depends largely on the type and abundance of crosslinking proteins. Rheology experiments have been used to measure the mechanical properties of actin networks. In these experiments, a pressure is applied to the network and the resulting deformation is observed. A material is called elastic if it returns to its original shape after removal of the force and viscous if it does not. Such experiments have shown us that actin networks are "viscoelastic," meaning elastic at short time scales and viscous at longer time scales (Chaudhuri et al., 2007; Marcy et al., 2004; Pujol et al., 2012; Wirtz, 2009).

The properties of actin described above—the existence of monomeric and polymeric forms, the ability to for networks, and the viscoelastic nature—allow it to mediate the transient formation of cell motility structures that include membrane protrusions such as lamellipodia, filopodia, and invadopodia as well as non-protrusive structures such as focal adhesions and stress fibers. Lamellipodia are thin, sheet-like protrusions of a cell that are the dominant feature of the leading edge of a protruding cell and provide the major driving force for locomotion. The underlying

actin structure of lamellipodia is the branched network that is largely assembled by the Arp2/3 complex, which is activated by the WAVE complex. The WAVE complex, in turn, is downstream of a membrane-bound GTPase called Rac (Bisi et al., 2013; Nobes and Hall, 1995; Svitkina and Borisy, 1999). This is the major mode of lamellipodia formation, but recent findings suggest that other proteins such as formins(Campellone and Welch, 2010) and Cdc42 (Block et al., 2012) are involved in the formation of lamellipodial protrusions.

Filopodia are tight bundles of long actin bundles that form fingerlike protrusions and act as the sensory and guidance organelle (Cater and Rehder, 1995; Mattila and Lappalainen, 2008; Rorth, 2003). The mechanism of filopodia extension is well-characterized. More contentious is the mode of filopodia initiation, especially with regard to the involvement of the Arp2/3 complex (Lee et al., 2010; Small et al., 1995; Suraneni et al., 2012b; Wu et al., 2012). Invadopodia are "invasive" feet of the cell membrane that extend into the ECM and are thought to be sites of high levels of proteolysis and cell signaling. These structures are somewhere between the lamellipodia and filopodia, with both branched and unbranched actin filaments (Buccione et al., 2004; Gimona et al., 2008; Weaver, 2006). Stress fibers are actin bundles made of short actin filaments of alternating polarity, found at the cell body of moving cells (Cramer et al., 1997). There are at least three types of stress fibers in the cell: ventral stress fibers and dorsal stress fibers run parallel to the direction of movement while transverse arcs run perpendicular. Ventral stress fibers are typically associated with cell-substrate adhesions at both ends while dorsal stress fibers are typically associated with one, and transverse arcs are not associated with any (Hotulainen and Lappalainen, 2006). In particular, dorsal stress fibers are thought to be the major transmitter of force to the substrate through the adhesions. Focal adhesions are mature cell-substrate adhesions,

and they are large, dynamic macromolecular protein complexes that link the actin cytoskeleton to the extracellular matrix.

Motile Forces

It is accepted that cell migration (at least in two-dimensions) is characterized as a four-step-process involving protrusion, adhesion, translocation, and retraction (Fig. 1)(Ladoux and Nicolas, 2012). During the protrusion step, the membrane at the leading edge of the cell moves forward. Then, the cell makes adhesions to the extracellular matrix in order to translate the protrusion into forward movement of the cell. Next, the cell body and nucleus translocate in the direction of migration. Finally, deadhesion and retraction of the tail end of the cell completes the process. These processes are highly coordinated and regulated by the Rho family of GTPases, CDC42, Rac, and RhoA (Nobes and Hall, 1995). Forward advancement of a cell is a result of the coordinated repetition of the four steps. What metastatic cancer cells do, then, is to somehow "hijack" one or more modules of normal cell motility mechanisms in order to attain pathologically enhanced motility.

Each of the four steps of cell migration is closely controlled and characterized by different mechanical forces present in the cell. During protrusion, protrusive forces result from actin assembly and adhesion engagement. This gives rise to small membrane protrusions called pseudopods, some of which eventually become large lamellipodia. Following this step, traction forces, which are forces that an adherent cell exerts on the underlying substrates, result from the combination of adhesion engagement, actin retrograde flow, and contractile forces from stress fibers. Such forces allow a cell to move its body and the nucleus through various extracellular

environments. Finally, deadhesion and retraction of the rear of the cell occurs due to a combination of contractile forces, actin binding proteins (Wear et al., 2000), and enzymatic reactions—phosphatases (Zeng et al., 2003), proteases (Pfaff et al., 1999; Potter et al., 1998), and focal adhesion kinase (Ilic et al., 1995a; Zeng et al., 2003), among others—that are yet incompletely understood. The coordination of these forces in timing, direction, and location allows a cell to move in the desired direction and even allow it to travel large distances.

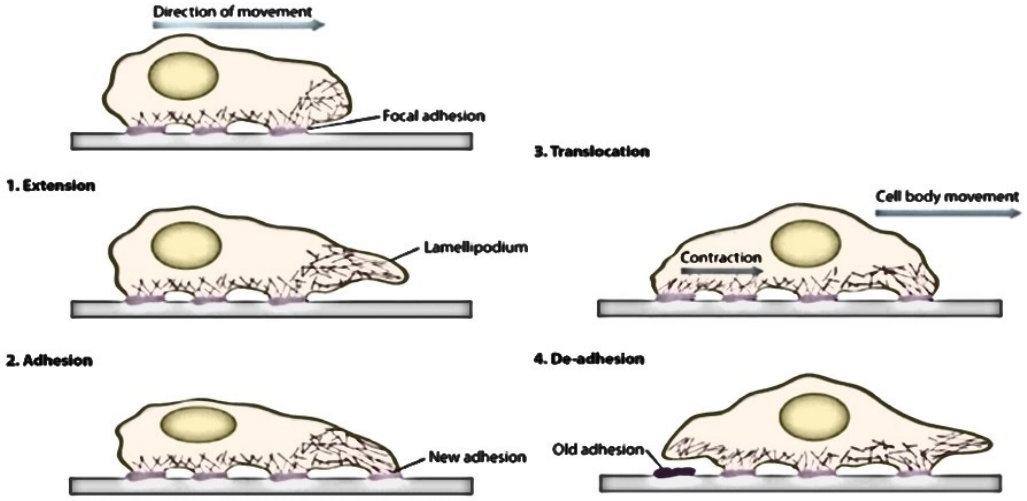

Figure 1. Steps of cell migration in 2D. 1. Polymerization of actin filaments at the leading edge is creates the protrusive force necessary for initial "blebs" that can eventually become lamellipodia. 2. The protruding front adheres to the underlying substrate through cell-substrate adhesions. The adhesions are linked to the existing actin network. 3. The combination of retrograde actin flow and contractile forces from stress fibers generates tension to pull the cell body forward. 4. Forces from the contractile network and enzymatic reactions result in deadhesion and retraction of the trailing cell edge.(Ladoux and Nicolas, 2012)

The first experimental evidence for the existence of such cellular forces came in the late 1960's and the early 1970's, when cell biologists first observed the flow of material (actin) towards the cell body in growth cones and fibroblasts (Bray, 1969; Ingram, 1970). The actual term "retrograde flow" was coined much later (Lin and Forscher, 1995). Subsequently, it was

observed that microbeads placed on surface of Aplysia bag cell growth cones were transported rearward at rates that cannot be accounted for by passive attachment to the actin cytoskeleton alone (Forscher et al., 1992). It was soon discovered that myosin II, a motor protein that binds to and "walks" along actin filaments, has a central role in this phenomenon because it can pull actin filaments past one another, similar to what happens in muscle cells (Pollard and Weihing, 1974). Following such observations, cell biologists then wondered how such retrograde flow of polymers might produce forward motion. It was discovered that the key component is the adhesion that links the actin cytoskeleton to the ECM, thereby effectively serving as a molecular clutch (Howard, 2001). These adhesions were also key to understanding cell traction force.

Traction force

Traction forces result from the combination of tension from actomyosin bridges in the cell and actin polymerization at the leading edge and are transmitted to the extracellular matrix through cell-substrate adhesions. They are thought to be a major driver of cell motility, ever since the observation was made that traction force can result in cell migration even in the absence of lamellipodia (Cramer et al., 1994). Because traction force plays such a key role in cell migration, numerous attempts were made first to observe it then to measure it. One of the first attempts at observing traction force came in 1980, when Harris and colleagues plated cells on thin silicone rubber substrata, where wrinkles appeared as cells moved on the surface (Harris et al., 1980). The disadvantage of this method was that it was impossible to quantify traction stress because wrinkling is a nonlinear and chaotic process.

Since then, other methods have been developed that allow one to quantify traction force more accurately. One method is the use of micro-pillars of known size and elasticity, the deflection of which can be used to calculate force (Li et al., 2007; Saez et al., 2005; Schoen et al., 2010; Tymchenko et al., 2007). The major disadvantage of using micro-pillars, however, is that cells must adhere to discrete substrates, which likely affects cell motility and adhesions. In addition, the stiffness of the micro-pillars needs to be very carefully calibrated and possible crosstalk between adjacent pillars needs to be corrected. The current method of choice came nearly two decades after the initial experiments by Harris: Dembo and colleagues pioneered traction force microscopy (TFM) for mammalian cells in which they used non-wrinkling polyacrylamide substrates embedded with fluorescent beads(Dembo and Wang, 1999a). Traction forces that are exerted by cells on the extracellular environment are derived from the displacement of these beads. Analysis of such data requires steps that detect and track the beads, calculate the displacements, and then calculate the traction force. Such calculations are not trivial, and various algorithms have been proposed that have allowed cell biologists to study overall force distributions of migrating cells, the effect of mechanical properties of the ECM on cellular contractility, and overall contractility in healthy and diseased cells.

Traction forces and other cellular forces are directly affected by and also affect the cellular arrangements of the cytoskeleton. These cytoskeletal rearrangements, especially those of actin, are differentially regulated by the functions of a number of actin-binding proteins defining the rates of polymer assembly and disassembly, cross-linking, and bundling and thus regulating cell motility.

Actin binding proteins

There is a great diversity in the proteins that bind actin, in terms of both structure and function. Because actin binding proteins are immediate regulators of the actin cytoskeleton, which then controls cell motility, it is not surprising that many of them have been associated with cancer (Olson and Sahai, 2009). For the purposes of this work, I will primarily focus on those actin binding proteins that have a close link to cancer. A more comprehensive review of actin binding proteins can be found elsewhere (Dos Remedios et al., 2003; Pak et al., 2008).

Arp2/3 complexes have already been mentioned above as the protein responsible for branched actin networks, which is especially crucial for the formation of lamellipodia. These complexes are composed of seven proteins (including Arp2 and Arp3) and nucleate new filaments off of existing ones at a ~70º angle. Because of the structural similarities between Arp2, Arp3, and actin, it is believed that the two proteins are directly involved in the initiation of new daughter filament by serving as an active dimer for nucleation. Many studies show correlations between metastatic processes and the expression levels of different components of the Arp2/3 complex. For example, Arp2 protein has been found to be upregulated in colorectal and breast carcinomas (Iwaya et al., 2007a; Iwaya et al., 2007b; Otsubo et al., 2004; Yokotsuka et al., 2011), and there are conflicting results regarding the direction of regulation with regards to gastric carcinoma (Kaneda et al., 2004; Zheng et al., 2008). As another example, ARPC2, another protein in the complex, has been found to be down regulated in gastric carcinoma(Kaneda et al., 2004) and upregulated in breast carcinoma (Kim et al., 2009). It is unclear at this time why conflicting data exist. It could be due to different origins of tissues and samples but it is also possible that specific temporal regulation of Arp2/3 is required to modulate invasive properties at specific times during cancer progression.

Members of the WASP superfamily of proteins (WASP, SCAR/WAVE) activate Arp2/3 by binding to both Arp2/3 and G-actin. This brings monomeric actin into close proximity to Arp2/3, greatly increasing the rate of Arp2/3-mediated actin filament nucleation and polymerization. In addition, WASP proteins are known to link Arp2/3 to upstream signals such as the Rho family of GTPases and are now recognized as the node that converts protein-protein and protein-membrane interactions to actin polymerization (Takenawa and Suetsugu, 2007). With such a crucial role in the cell, it is not surprising that members of the WASP family have been linked to cancers of the breast, esophagus, prostate, thymus, endometrium, and the liver.

Tropomyosins bind along the length of an actin filament and influence the association of actin with other actin binding proteins. Many different isoforms exist, and they have been correlated with multiple cancer types, including breast cancer, colon cancer, hepatocellular carcinoma, thyroid papillary carcinoma, and anaplastic large cell lymphoma.

Other than the proteins just mentioned, numerous actin binding proteins exist, which will be mentioned just briefly here: Formins are a class of proteins involved in the polymerization of actin at the barbed end of actin filaments and play a key role in the formation of filopodia. ADF/Cofilin plays a major role in the disassembly of actin filaments, which also has the effect of increasing the number of sites of nucleation for new actin filaments. Capping proteins bind to the barbed end of a filament and prevent the exchange of monomers.

It is not surprising that actin binding proteins have been linked to cancer since the actin cytoskeleton plays such a crucial roles in migration and cell division. Next, we will examine one

particular actin binding protein that has close links to not just cancer but to metastasis in particular.

Fascin

One actin associated protein of particular interest in the cancer field is fascin, a 55-kD monomeric protein known to cross-link F-actin into tightly packed parallel bundles (Fig. 2) (Courson and Rock, 2010; Jansen et al., 2011; Yamashiro-Matsumura and Matsumura, 1985). It was first discovered in 1970's in sea urchin extract (Bryan, 1978; DeRosier et al., 1977; Otto et al., 1979), and since then it has been established that fascin is conserved across vertebrates and invertebrates (Anilkumar et al., 2003; Duh et al., 1994). Three different isoforms of fascin have been identified in mammals. The expression of fascin-2 is largely limited to the retina and hair-cell stereocilia, and fascin-3 expression is limited to the testis (Hashimoto et al., 2011; Zhang et al., 2008). For the rest of the present work, "fascin" is used to denote fascin-1.

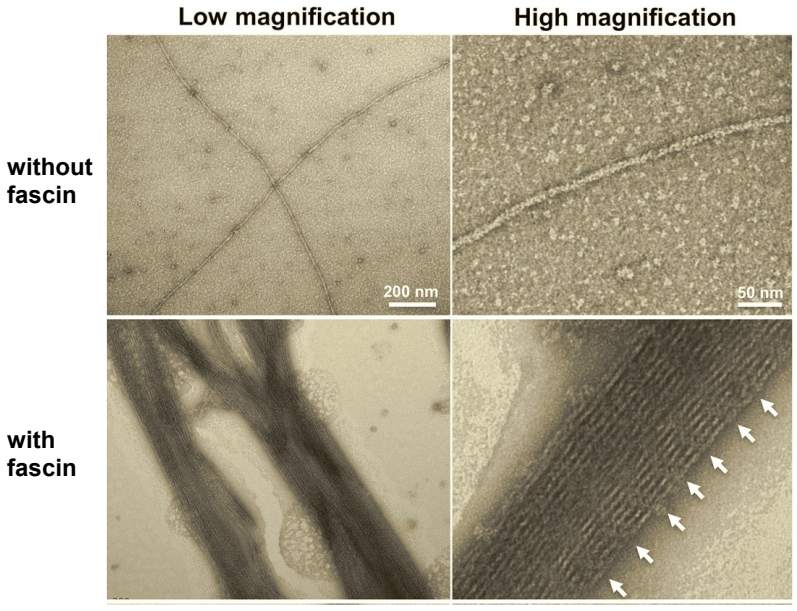

Figure 2. Transmission electron micrographs of negatively stained actin filaments alone and in the presence of fascin. Low magnification images (*left*; *scale bar*, 200 nm) show that nearly all the actin filaments are incorporated into bundles in the presence of fascin. High magnification images (*right*; *scale bar*, 50 nm) show examples of a thick ordered bundle with periodic striations (indicated by *arrows*) formed by fascin. (Jansen 2011)

Fascin is unique among actin bundling proteins in that it is able to function as a monomer due to having at least two separate actin-binding sites, one at the N-terminal and one at the C-terminal region (Jansen et al., 2011). It localizes to a number of actin-based structures, especially the filopodia (Aratyn et al., 2007; Jaiswal et al., 2013; Jansen et al., 2011; Otto et al., 1979; Schafer et al., 2011; Yang et al., 2013). Expression is highly regulated spatially and temporally during embryonic development. High levels of fascin expression are found in motile embryonic cells such as *Drosophila* border cells. Among normal mammalian tissues its expression is highest in neuronal and glial cells, microcapillary endothelial cells, and antigen-presenting dendritic cells, but it is largely absent or present in very low levels in epithelial cells (Yamashiro, 2012; Zhang et al., 2008). Within the cell, fascin is a well-established marker of filopodia (Aratyn et al., 2007; Otto et al., 1979; Yamashiro et al., 1998). Others have also seen fascin localize to structures such as stress fibers and invadopodia (Hashimoto et al., 2011; Xu et al., 2011; Yamashiro, 2012).

Contrary to its low expression levels in normal epithelial cells, fascin is significantly upregulated in a number of human epithelial carcinomas and has been a top hit in screens for genes that mediate metastasis to the lungs or the brain (Minn et al., 2005; Nguyen et al., 2009). Such a feature makes the protein a particularly attractive target for cancer research, as a drug that selectively targets fascin will likely have the ability to selectively target cancer cells over normal cells. A myriad of papers were published in the last 10 years that indicate that fascin expression is highly correlated with cancer progression and metastasis in multiple cancer types. In fact, fascin has been found to be a good biomarker for carcinomas of the biliary duct, bladder, brain, breast, colorectum, endometrium, kidney, liver, lung, neck, esophagus, pharynx, ovary, pancreas, prostate and stomach by various vitro, in vivo, and immunohistochemical studies (Al-Alwan et al., 2011; Darnel et al., 2009; Gao et al., 2012; Hanker et al., 2013; Hashimoto et al., 2004;

Hashimoto et al., 2006; Kim et al., 2012; Kulasingam and Diamandis, 2013; Ma et al., 2013; Mao et al., 2013; Pelosi et al., 2003; Samimi et al., 2013; Teng et al., 2013; Xu et al., 2011; Yoder et al., 2005; Zigeuner et al., 2006). A meta-analysis of the available literature confirmed high fascin expression level to be associated with increased risk of mortality or increased risk of metastasis in five most common carcinomas (Tan et al., 2013). Furthermore, it is highly likely that the level of fascin expression is tightly linked to the process of migratory phases of metastasis, as it was shown in human colon carcinomas that fascin level seemed to return to more basal levels once the cells reach their destination (Vignjevic et al., 2007).

Recent studies have shed some light on the regulation of fascin. It has been shown to be downstream of the Rac and Rho proteins through the PAK1 pathway or the p-Lin-11/Isl-1/Mec-3 kinases, respectively (Jayo et al., 2012). In addition, the activation of IGF-1 and TNF-alpha pathways have been shown to upregulate the expression of fascin. There is more extensive research on post-translational modification of fascin through the protein kinase C (Anilkumar et al., 2003). When phosphorylated at serine-39 within the N-terminal actin-binding domain, fascin becomes inactive and unable to bundle actin filaments, providing a means by which the protein can be regulated in the cell. This characteristic has implications for the regulation of fascin both in diseased and healthy states.

However, to date, very little is known about the direct molecular or cell mechanical mechanisms by which fascin might promote migration in a tumor environment. What effect, if any, fascin might have on each of the four steps of cell motility (protrusion, adhesion, translocation, and retraction) is unknown. Ever since fascin was recognized to be a filopodial marker, many fascin studies have been done in the context of filopodia. However, it is unlikely that completely

explains what is observed clinically with cancer patients. We can foresee that the bundling of actin will change the mechanical properties of the viscoelastic cytoskeleton. This can, for instance, lead to cells with properties that allow it to withstand more protrusive forces. Such a scenario also does not rule out the possibility that the protein has currently unknown functions that affect cell motility. This thesis work will aim to elucidate some of the cellular mechanisms that may link fascin to enhanced motility in the context of metastasis.

Model systems

It is indeed true that much cell migration in epithelial cells is a two-dimensional phenomenon. However, this is not always the case, especially not in the case of tumor cells which are defined by uncontrolled abnormal growth. Thus, another goal of the project was to corroborate some of the results in a three-dimensional setting. For the three-dimensional culture studies described here, MDA-MB-231 cells were used. MDA-MB-231 cells were derived from human breast adenocarcinoma. Previous studies have shown the cells to be highly metastatic and express high levels of fascin. This makes them the ideal system in which to knockdown fascin and observe differences from the control case. Additionally, given that these cells are neoplastic and that PtK1s are normal epithelial cells, the two systems complement each other very well.

The choice model systems described in the study are PtK1 cells and MDA-MB-231 cells. For the high-resolution imaging studies, PtK1 cells were used. These cells were established in 1962, derived from the kidney epithelial cells of species of rat kangaroo found in Australia, *Potorous tridactyl (*Walen and Brown, 1962). This cell line has been heavily used in the field of cell division for imaging studies because the cells are very flat and remain so even when they divide

(Heneen, 1970; Levan et al., 1966; Levan, 1970). This characteristic makes them ideal for imaging especially for high-resolution studies. Moreover, many of the proteins involved in cell motility have been spatially and temporally characterized in PtK1 cells, meaning that I will be also able to fit the results of my work into a known framework. For this project, these cells have proven to be ideal for the high resolution two-dimensional studies.

Concluding Remarks

Given fascin's well-studied correlations to cancer metastasis and progression, the goal of this thesis work is to tease apart the molecular/cellular mechanism by which fascin might bring about such outcomes. We start with the hypothesis that fascin's role as the actin bundler in filopodia cannot completely explain the enhanced metastasis seen in cancer patients with tumors that express high amounts of fascin. Since fascin is a structural protein, any changes in its levels will change the properties of the viscoelastic actin cytoskeleton, thus affecting cell motility. In particular, I would like to see how varying levels of fascin affects different steps of cell migration, especially protrusion and adhesion. The project will also describe measuring the effects of fascin on cellular forces, especially traction force.

The major tools I will use to achieve the work described in this thesis are various forms of quantitative live cell imaging. In his book *Micrographia*, Robert Hooke (who incidentally also coined the word 'cell' to describe biological organisms) writes the following:

> ". . . and by the help of Microscopes, there is nothing so small, as to escape our inquiry; hence there is a new visible World discovered to the understanding. . . . By this the Earth it self, which lyes so neer us, under our feet, shews quite a new thing to us, and in every little particle of its matter, we now behold almost as great a variety of Creatures, as we were able before to reckon up in the whole Universe it self."

-Robert Hooke, Micrographia, 1665 (Hooke, 1665)

The ability to see things with "nothing so small … escap[ing] our inquiry" has been crucial in the progress of cell biology since Hooke's time. Something else that occurred since 1665 is the emergence of technology that has advanced leaps and bounds to allow us to do far more than just behold a "great variety of Creatures"; we now even go as far as to see single molecules within an individual cell belonging to such a Creature. Especially in the early days of microscopy, qualitative analysis of images obtained from microscopes has led to many insightful conclusions. However, there is still much that is missed without the use of quantitative analysis. In recent years, the use of computer algorithms to do such image analysis has allowed for much faster, unbiased calculations, achieving in minutes what would take one or more scientists days, months, or even years.

The Danuser lab has established a name for itself as Laboratory of Computation Cell Biology. The lab brings together cell biologists and computer scientists to innovate new methods in microscopy as well as computer algorithms that are used to analyze the results (Danuser, 2011). Some exciting innovations that come from this lab are quantitative speckle fluorescent microscopy for measuring actin flow and u-track for tracking of subcellular components (Jaqaman et al., 2008; Machacek et al., 2009; Mendoza et al., 2012). As such, the lab has the perfect combination of expertise in cell biological experiments and quantitative analysis that makes it the ideal venue for this Ph.D. thesis work.

Filopodia-independent roles of fascin in promoting cell motility

Introduction

Fascin is an actin binding protein that bundles actin filaments by virtue of its two actin binding domains(Jansen et al., 2011). Numerous studies have linked fascin overexpression to poor patient outcome(Hashimoto et al., 2004; Hashimoto et al., 2006; Pelosi et al., 2003; Yoder et al., 2005) and metastasis(Al-Alwan et al., 2011; Darnel et al., 2009; Xing et al., 2011; Zigeuner et al., 2006) in multiple cancer types. Additionally, fascin has surfaced as a top hit in screens for genes that promote cancer metastasis to the lungs or the brain (Minn et al., 2005; Nguyen et al., 2009). Much of the molecular studies involving fascin has focused fascin's roles in filopodia, following up on the discovery of fascin as a filopodial marker(Otto et al., 1979). Thus, fascin's role in cancer cell biology has implicitly or explicitly been related to the enhanced formation of filopodia, which serve as mechanical and signaling hubs guiding directed migration. For example, HCT116 colorectal carcinoma cells, one of the classic models associated with high fascin expression, displays higher migration efficiency and more filopodia than another colorectal carcinoma cell line, HT29, which is low in fascin expression (Vignjevic et al., 2007) (Suppl. Fig. 1). However, it is not completely clear how much of the motility-enhancing role of fascin is filopodia-dependent and how much is filopodia-independent. Indeed, some more recent studies have begun to link fascin to adhesions and binding partners in other pathways (Breitsprecher et al., 2011; Elkhatib et al., 2014; Kulasingam and Diamandis, 2013). However, how high expression levels of fascin are mechanistically linked to enhanced motility and eventually detrimental patient outcome is unclear. To address this question, we employed quantitative live-cell imaging in various scales to study the role of fascin in promoting cell motility in normal and neoplastic cells.

Results

Fascin promotes collective migration in PtK1 cells

To dissect the roles of fascin in cell migration by high-resolution imaging, we first chose PtK1 cells as our model system. PtK1s are a kidney epithelial cell line of marsupial origin that has served innumerable studies of cytoskeleton organization and function because they are very flat and thus amenable to high-resolution quantitative live cell imaging. In particular, many of the key features of F-actin dynamics, adhesion, and force generation as related to directed migration have been worked out in this system (Gupton and Waterman-Storer, 2006; Hu et al., 2007; Ji et al., 2008; Ponti et al., 2004). Like many epithelial cells they express fascin at low, yet well detectable levels. We established protocols and reagents to further decrease fascin levels by siRNA-based depletion and to increase fascin levels by expression of EGFP-fascin under the control of a CMV-promoter.

We first investigated whether varying fascin levels in PtK1 cells would qualitatively reproduce the differences in collective migration measured in the colorectal HCT116 – HT29 high-low fascin-expressing cell pair (Fig. 3A). Indeed, fascin overexpressing PtK1 cells displayed a wound closure rate 1.5 times faster than control cells (Fig. 3B). The magnitude of this increase was somewhat surprising in view of the fact that PtK1 cells do not readily take up DNA, and therefore the transfection rate for the cells is between 20-30%. PtK1 cells display a wound healing response under the guidance of prominent "leader cells" (Lim et al., 2010), which form persistent leading edge protrusions and a highly-contractile lamella that generate sufficient traction to pull the leader cell body forward along with neighboring 'follower' cells. In our wound healing assay, each 1344 pixel x 1024 pixel movie of the wound has at least two leader

cells, one on each side of the wound. Intriguingly, the proportion of leader cells that are GFP-fascin transfected is significantly higher than the overall transfection rate of PtK1 (Fig. 3C), which corroborates that fascin functions as a migration enhancer.

Immunofluorescence studies of islands of PtK1 cells showed that fascin localizes to the leading edge lamellipodium and to stress fibers in the lamella (Fig. 3D). In addition, the leading edge of cells expressing intermediate levels of GFP and those expressing intermediate levels of GFP-fascin are morphologically indistinguishable as both are free of filopodia (Fig. 3E). Taken together, these results suggest that fascin may have filopodia-unrelated roles in promoting cell motility.

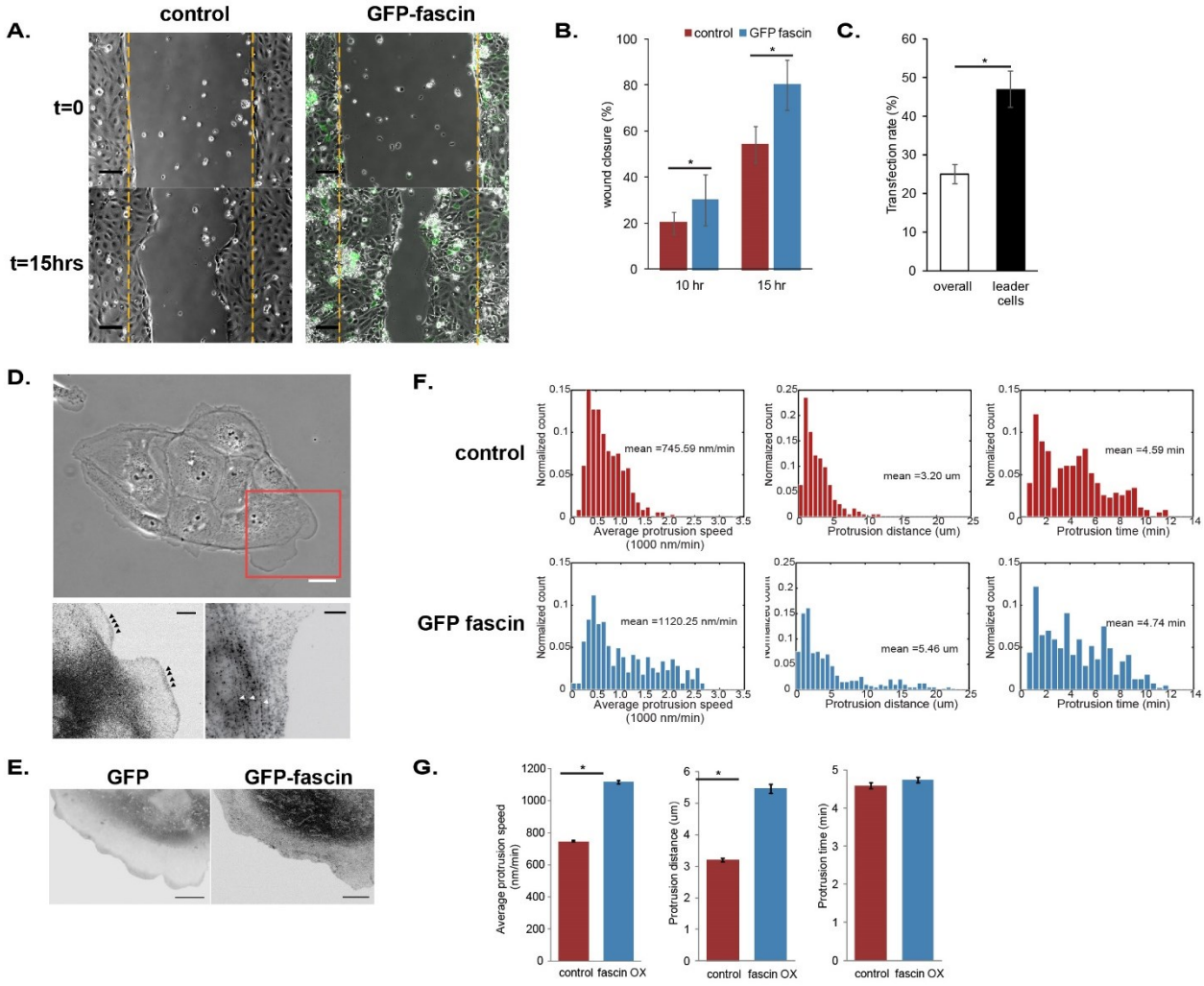

Figure 3. Collective and single-cell motility of PtK1 epithelial cells (A) Representative results of wound healing response in control (left column) and GFP-fascin cells (right column) at 0 and 15 hours. Scale bar: 50 µm. (B) Quantification of percentage wound closure at 10 and 15 hours. Error bars: SEM from 24 positions for each condition (3 independent experiments). * p-value < 0.001. (C) Transfection rate in all cells versus leader cells in wound healing response. Error bar: SEM from same samples as (B). * p-value < 0.001. (D) Top, a representative "island" of PtK1 cells. Red box: representative "leader cell". Bottom, fascin immunofluorescence studies showing localization of fascin to leading edge (left, black arrowheads) and stress fibers (right, white arrowheads). (E) Leading edge morphology of PtK1 cells transfected with GFP (left) or

Figure 3 (continued). GFP-fascin (right). (F) Histograms of average protrusion speed (left column), protrusion distance (middle column), or protrusion time (right column) in control (top row, 6 cells, 1218 time series) and GFP fascin (bottom row, 6 cells, 1299 time series) cells. All conditions were repeated in at least 3 independent experiments. (G) Bar graph of means found in (F). Error bar: SEM with n = number of time series. *p-value < 0.0001.

Fascin increases protrusive activities in single cells without the presence of filopodia

In a wound healing response, where cells at the wound edge are polarized by the asymmetry of cell-cell contacts, the closure rate is directly related to the net protrusion rate at the single cell level (Arthur and Burridge, 2001). To analyze protrusion dynamics at the single cell level, we expressed either GFP alone or GFP-fascin in PtK1 cells and acquired high-resolution time-lapse images at 5 second intervals over a period of 16 minutes (200 frames). During imaging of GFP-fascin cells, only those cells that expressed fascin at intermediate levels with no filopodia were selected. Then, edge detection software was used to track edge movement along the leading edge, and spontaneous protrusion-retraction cycles were analyzed with regard to the protrusion/retraction velocity, protrusion/retraction distance, and time since protrusion/retraction onset (Fig. 3F). Critically, because different sectors of the leading edge move asynchronously, these analyses were performed independently for 500-nm wide edge segments and subsequently processed in statistical distributions.

Histograms of the respective distributions indicate that the mean of the protrusion speeds averaged over one protrusion event was 1.5 times higher for fascin overexpressing cells than for control cells expressing GFP only (Fig. 3G). The mean distance covered by protrusion events was also 70% higher for fascin overexpressing cells. This increase is mainly induced by a skew of the distribution towards a few very long-distance protrusion events, suggesting that higher fascin expression promotes more sustained growth of actin filaments against increasing membrane tension (Ji et al., 2008). Of note, the mean duration of protrusion events was not significantly shifted by fascin overexpression, indicating that the increased protrusion distance is mainly associated with an increased advancement of the cell edge. SiRNA-mediated knock down of fascin expression by ~90% did not result in significantly reduced average protrusion speed or

protrusion distance (Suppl. Fig. 2). This is not unexpected because the control level of fascin expression in an epithelial cell like PtK1 is fairly low.

Complementary work in our lab using the same cell system shows that protrusion cycles are initiated by local formation of a nascent adhesion followed by growth of a non-adherent F-actin network until a force maximum is reached at which the cell edge stalls or retracts until a new nascent adhesion is formed (Ji et al., 2008; Lee et al., submitted). Accordingly, the protrusion distance is governed, in part, by the mechanical stability of the actin network to grow without adhesive anchorage to the substrate.

Fascin expressing cells have decreased overall traction stress and sustain traction stress at the leading edge

Our observation of increased protrusion distance in fascin-overexpressing cells suggested that the mechanical load sustained by the most frontal adhesions may also increase in these cells. To test this, we performed high-resolution traction force microscopy (TFM), which measures the force a cell or a group of cells transmits through adhesions to the substrate (Dembo and Wang, 1999b). The transmitted forces originate in actomyosin contraction in the lamella and in actin polymerization mediated propulsion of the cell edge (Gardel et al., 2008).

To observe differences in traction stress levels at the leading edge, we first compared traction stress at the 1-um leading edge. Results indicate that fascin overexpressing cells exert less stress on its substrate overall (Fig. 4A,B). Next, we analyzed the relation between traction stress levels and the protrusion/retraction state. As for the protrusion cycle analysis we used probing windows of 1 um^2 to sample local stress levels and edge velocities at each time point (Fig. 4C). The windows followed the cell edge over time, allowing us to record time series of stress levels in a

cell-frame of reference (Movie S1). To determine from asynchronously moving windows in one cell and from windows pooled over several cells how stress levels were modulated about a specific protrusive event (such as protrusion onset or retraction onset), we aligned the time series from individual sampling windows at the cell edge relative to the event of interest (W_1 and W_2 in Fig. 4C) and then averaged the aligned time series

Qualitatively, the temporal patterns of traction stresses were similar in control and fascin overexpressing cells (Fig. 4D). In both cases, the traction stress at the leading edge increased at retraction onset and decreased shortly after protrusion onset. An even sharper decrease was observed when the time series was aligned relative to the time point of maximum protrusion velocity. These decreases are related to the fact that after protrusion onset windows that move with the cell edge translocate away from the force-bearing adhesion sites. Quantitatively, there were two significant differences between control and fascin-overexpressing cells. First, in agreement with the overall lower traction stress levels produced by fascin overexpressing cells, the stress levels 1 um beneath the moving cell edge were also systematically lower than in control cells. Incidentally, the confidence interval fascin overexpressing cells was broader, most likely because of the heterogeneity in expression levels between cells. Secondly, fascin overexpressing cells maintained traction stress more stably after protrusion onset than control cells.

To further probe the relationship between protrusive state and traction stress, we studied correlations between cell boundary velocity and traction force boundary. Traction force boundary was found by converting traction stress magnitude into a grayscale heat map and increasing the boundary threshold to find the traction stress outline that minimizes noise. After calculating the protrusion velocities along the traction force boundary as well as the cell

boundary, we aligned both time series with respect to the maximum velocity of the traction force boundary (t=0 in Fig. 4E). In control cells, the cell boundary protrusion velocity reached maximum first, and the maximum of the traction stress boundary velocity followed. However, in fascin-rich cells, such trend was no longer observed (Fig. 4E). This can be interpreted to mean that fascin-rich cells assemble adhesions regardless of protrusion states.

Together, these differences seemed to refute our original hypothesis that fascin promotes longer protrusion cycles by increasing the mechanical stability of lamellipodial network in order to prolong filament growth against the leading edge membrane without requirement for substrate anchoring. On the contrary, our TFM data suggested that fascin-overexpressing cells must continually form nascent adhesion during the protrusion cycle. This would lower the overall traction stress generated in any particular point of the cellular footprint and would reduce the distance over which the growing actin filament network pushed the leading edge forward without mechanical coupling to the substrate.

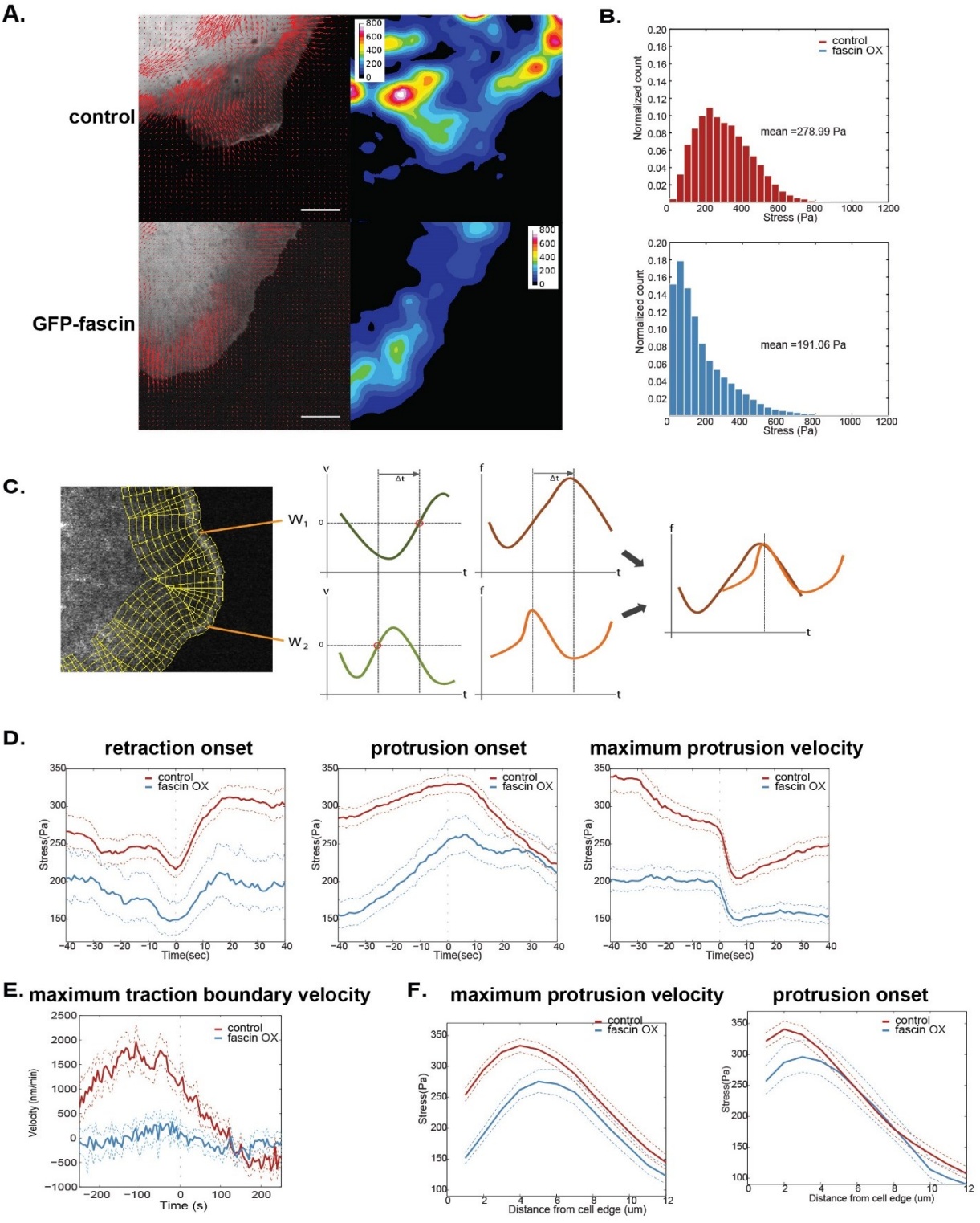

Figure 4. **Effect of fascin on traction stress in PtK1 cells.** (A) Representative traction force field (left, red arrows) and corresponding traction stress heat map (right) for GFP and GFP-fascin

Figure 4 (continued). cell. Force vectors are scaled equally. Scale bar: 10 μm. Heat map unit: Pa. (B) Histograms of overall traction stress in control (5 cells, 468 time series, 3 independent experiments) and GFP-fascin cells (8 cells, 868 time series, 3 independent experiments). Same cells were analyzed for (D) and (F). (C) Alignment of traction stress time series with respect to motion event. For two windows W_1 and W_2, protrusion onset is identified (red circle) and the W_2 velocity time series shifted by Δt to align time with respect to protrusion onset. Then, the force time series for W_2 is shifted using the same Δt. The resulting force time series (far right) are averaged for all windows. (D) Traction stress alignment with respect to retraction onset (left), protrusion onset (middle), and maximum protrusion velocity (right) for control (red) and GFP-fascin (blue) cells. (E) Leading edge protrusion velocity alignment with respect to maximal velocity of traction force boundary for control (red) and GFP-fascin (blue) cells. . For (D), (E), and (F), solid lines indicate population averages, and dotted lines about the population averages indicate 95% confidence intervals computed by bootstrap sampling.

Peak traction stress occurs further away from cell edge in fascin overexpressing cells

The canonical model of adhesion formation and maturation in migrating cells predicts that traction stresses increase with distance from the leading edge as NAs get stabilized and transform into focal adhesion (FAs) (Gardel et al., 2008). The stress maximum is reached in a zone of maximal FA density, concomitantly with a transition from predominantly compressive forces generated by F-actin polymerization in the lamellipodium to pulling forces generated by actomyosin contraction in the lamella. We examined this spatial pattern of traction stresses at protrusion onset and maximum protrusion velocity as reference time points (Fig. 4E) by averaging the temporally aligned stress values in layers of probing windows at a particular distance from the cell edge (Movie S2). At both reference time points control cells and fascin-overexpressing cells displayed the expected stress profile. Importantly, the reduced traction stresses in fascin-overexpressing cells was maintained throughout the profiles.

However, in fascin-overexpressing cells the sites of maximum traction stress are shifted towards the cell center, suggesting that higher fascin levels induce a wider zone of NAs that mechanical support the growth of the lamellipodial network against membrane tension.

Fascin increases nascent adhesion density at the leading edge without affecting dynamics

To test the prediction that fascin overexpression widens the zone of NA formation, we collected total internal reflection fluorescence (TIRF) movies of cells expressing HaloTag-paxillin as a canonical marker of all adhesion structures (Movie S3). Paxillin was expressed in cells that were also expressing GFP only or GFP-fascin (Fig. 5A). For analysis of the movies, we developed a computer algorithm that detected NAs as diffraction-limited spots and more mature adhesion complexes and FAs as paxillin-rich patches. The algorithm also was able to track adhesions over

time and to classify NAs that transitioned in to focal complexes and FAs as “maturing nascent adhesions” as opposed to NAs that turned over without maturation as “failing nascent adhesions.”

This analysis yielded several results: First, the density of nascent adhesion in the 5-um leading edge is significantly greater in fascin-overexpressing cells than in control cells (Fig. 5B). Second, the life times of both failing and maturing nascent adhesions are not significantly different between control and fascin overexpressors. (Fig. 5C,D). Third, the ratio of failing to maturing nascent adhesions are not significantly different between the two groups (Fig. 5E). Fourth, tracking of both fascin and paxillin fluorescence at sites of nascent adhesions starting 100 seconds prior to nascent adhesion detection shows that fascin fluorescence increases at a high rate before paxillin fluorescence does so (Fig 5F). Indeed, this is shown more clearly in the plot of the fluorescence ratio of the two channels (Fig. 5G).

Combined, these observations provide strong evidence that fascin plays a role in templating nascent adhesions and affects early dynamics of adhesions rather than later dynamics such as maturation or disassembly. Of note, fluorescence tracking analysis suggests that fascin is recruited to sites of nascent adhesion formation even before paxillin.

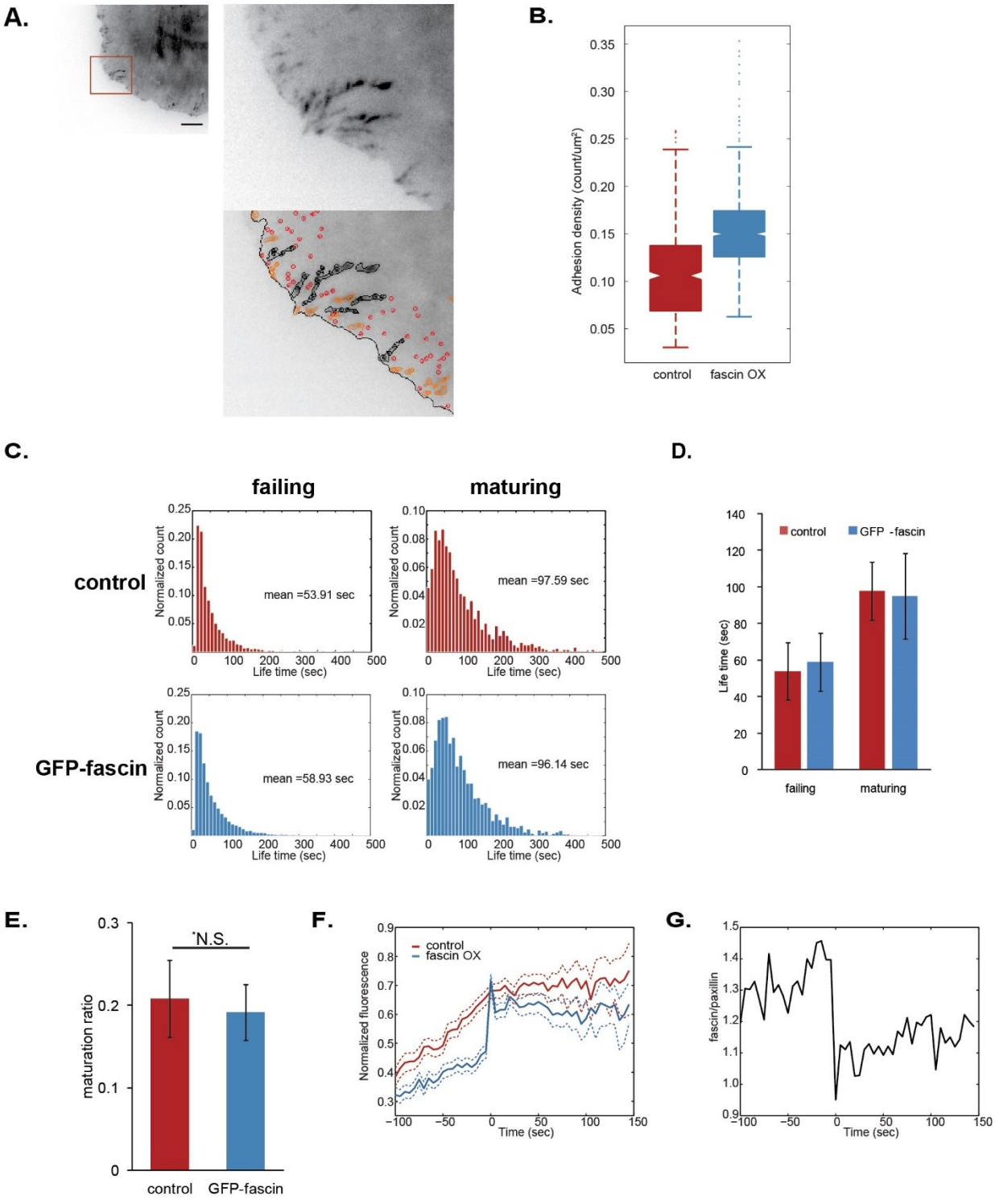

Figure 5. Effect of fascin on cell-substrate adhesions in PtK1 cells. (A) Tracking of cell-substrate adhesions with HaloTag-TMR-labeled paxillin. Left, zoom-out view of lamellipodia of a cell expressing HaloTag-paxillin labeled with TMR-ligand and imaged in with total internal

Figure 5 (continued). reflection fluorescence microscopy. Right, zoom-in view of a portion of the lamellipodia without (top) and with (bottom) results of adhesion tracking algorithm overlaid. Red: diffraction-limited spots that are nascent adhesions, orange: focal complexes, black: focal adhesions. Scale bar: 10 μm. (B) Quantification from computer algorithm in (A). Box plot of adhesion densities in control (5944 adhesion tracks in 3 cells) and GFP-fascin cells (11240 adhesion tracks in 4 cells). *p-value < 0.0001. The same cells were analyzed for parts (C), (D), and (E). (C) Histograms of life times of failing and maturing nascent adhesions. (D) Bar graph of mean life times. Error bars: SEM with n = number of adhesion tracks. (E) Bar graph of "maturation ratio," defined as ratio of adhesion tracks that mature into focal complexes or focal adhesions out of all adhesion tracks. Error bars: SEM with n = number of cells. *N.S. not significant. (F) Fluorescence alignment in fascin and paxillin channels with t = 0 defined as nascent adhesion detection and subsequent fluorescence tracking in both channels at individual nascent adhesions. Mean of 400 nascent adhesions. Solid lines indicate population averages, and dotted lines about the population averages indicate 95% confidence intervals computed by bootstrap sampling. (G) Ratio of fascin fluorescence to paxillin fluorescence from analysis in part (F).

Fascin decreases lamellipodial actin flow

The rate of cell edge protrusion is the result of the rate of actin filament assembly minus the rate of retrograde flow of actin filaments at the leading edge (Lim et al., 2010). Thus, the increased protrusion rates we observed in fascin-overexpressing cells could be explained either by an increase in polymerization rate or a decrease in retrograde flow, or a combination of both. To assess which of these mechanisms is at play with increased fascin levels, we measured actin retrograde flow by quantitative fluorescent speckle microscopy (Fig. 6A, Movie S4). To generate speckle contrast, a low fraction of actin subunits were fluorescently labeled by expression of SNAP-tag actin and incubation of cells with low concentrations of SNAP-Cell TMR-Star then washed with phosphate buffered saline.

For control cells expressing GFP in addition to SNAP-tag actin we measured average flow rates of 943 nm/min in the first 5 um from the cell edge (Fig. 6B). In comparison, GFP-fascin expressing cells displayed significantly lower average flow rates of 526 nm/min, indicating that the higher density of NAs in these cells reduces the flow. Moreover, the approximate proportionality of actin flow and traction stresses is consistent with a slip friction clutch model in which the kinetics of the coupling between actin filaments and substrate is dominated by the affinity of molecular interactions within the adhesion and nearly independent of the (probably weak) load on an individual bond (Howard, 2001). Quite interestingly, control cells exhibited larger spatiotemporal variations in retrograde flow, suggesting that the higher density of NAs in fascin-overexpressing cells promotes redundancy among adhesions that results in a sustained slower flow regime.

To determine whether the reduced flow in fascin-overexpressing cells can explain the increased protrusion and migration rates in these cells we subtracted average protrusion speed of control

cells from that of GFP-fascin cells to calculate the increase in average protrusion speed in GFP-fascin cells (Fig. 3F, 1120 nm/min – 745 nm = 375 nm). Then, we subtracted the actin flow rate of GFP-fascin cells from that of control cells to calculate the decrease in actin flow in GFP-fascin cells (Fig. 6B, 943 nm/min – 526 nm/min = 417 nm/min). The two numbers closely match, suggesting that the increase in protrusion seen in fascin overexpressing cells is driven by the slower actin retrograde flow rather than faster actin polymerization.

In light of the data presented so far, we propose a model in which fascin plays multi-faceted roles to increase cell motility (Fig. 6C). In particular, fascin templates nascent adhesions such that with more fascin, more nascent adhesions are formed. Due to the presence of a higher density of adhesions actin retrograde flow is decreased. Under the assumption that individual molecular bonds in adhesions are relatively weak and thus NAs operate in a slip friction regime, the reduction of flow is translated into overall lower traction and faster protrusion.

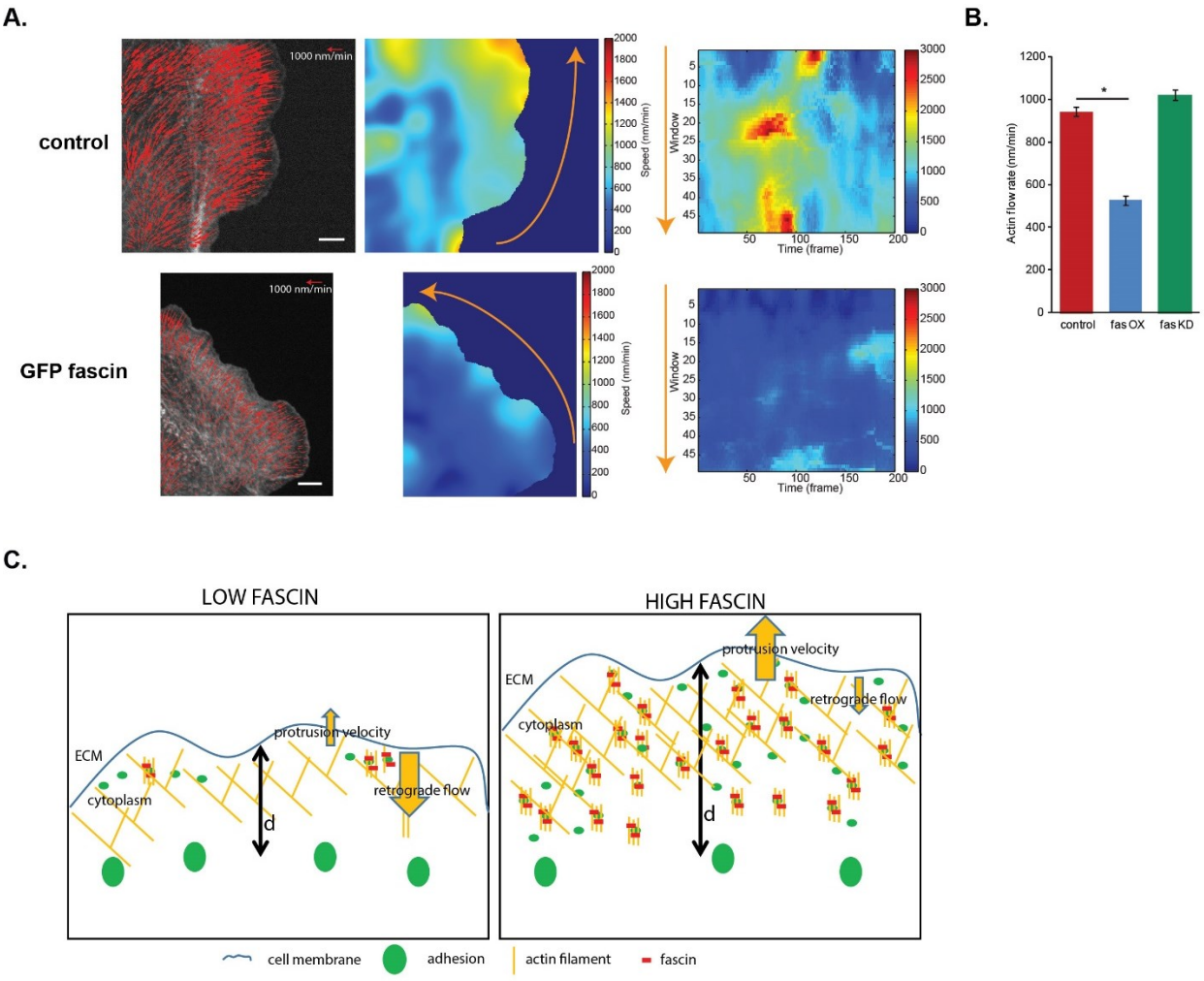

Figure 6. Effect of fascin on actin flow in PtK1 cells. (A) Representative actin flow representations for control and GFP-fascin cell. Left column, actin flow in one frame, represented as vectors. Middle column, actin flow in one frame, represented as heat map. Right column, actin flow activity map showing flow in all frames and all windows along the 5 µm-wide leading edge. Orange arrows indicate direction of window numbering. Scale bar: 5 µm. (B) Mean actin flow in the 0-5 µm from the leading edge for control (5 cells 355 time series), GFP-fascin (6 cells 331 times series), and fascin si cells (5 cells 341 time series). Error bars: SEM with n = number of time series. *p-value << 0.0001 (C) Model of nascent adhesion templating by fascin during cell protrusion.

Fascin promotes invasion in three dimensions in cancer cells

Since wound healing is a largely two-dimensional process also in physiological settings, it is plausible that the conclusions we draw from high-resolution imaging of epithelial cells on 2D substrates are indeed applicable to physiological and pathophysiological processes. In particular, intravital imaging data suggest that in many cases cancer metastasis is a collective migration phenomenon akin a wound healing response (Friedl and Gilmour, 2009). Thus, the proposed model of fascin's role as a promoter of nascent adhesion formation and its consequences for enhanced protrusion and migration offers a mechanism for the more aggressive invasion and spreading of epithelial carcinoma with high fascin expression levels. We were curious whether the same conclusion could be drawn for a cancer model that tends to spread by migration of individual cells and is also associated with high fascin expression. One such model is the MDA-MB 231 cell line, which has been derived from a breast cancer and which express high levels of fascin (Xing et al., 2011). Curiously, despite the high levels of fascin, these cells display a very moderate occurrence of filopodia, and knock-down of fascin by siRNA has no visible effect on filopodia density. On the other hand, knock-down of fascin resulted in sparser NAs as compared to cells treated with control siRNA (Fig. 7A), complementing our observations of denser NAs in fascin-overexpressing cells Together, this suggested that differences in invasion and motility of MDA-MB 231 control and fascin-depleted cells would be related to a largely filopodia-independent, adhesion-mediated function of fascin.

To test whether with the MDA-MB 231 model we could generalize our findings also to migration in 3D, we subjected control and fascin knock-down cells to a collagen invasion assay (Smith et al., 2008). In this assay cells were plated cells on glass and then covered with a collagen plug. Cells were stimulated by chemoattractant (FBS) added to medium on top of the

plug and then allowed to travel for 24 hours. After formaldehyde fixation and Hoechst staining, the 3D collagen volume was imaged at every z-distance of 1 um (Fig. 7A). Using a custom-designed computer program we detected and quantified the number of cells at each z-plane to calculate invasion rate. Results indicate that invasion is indeed greater for cells transfected with control siRNA than for cells transfected with fascin siRNA (Fig. 7B).

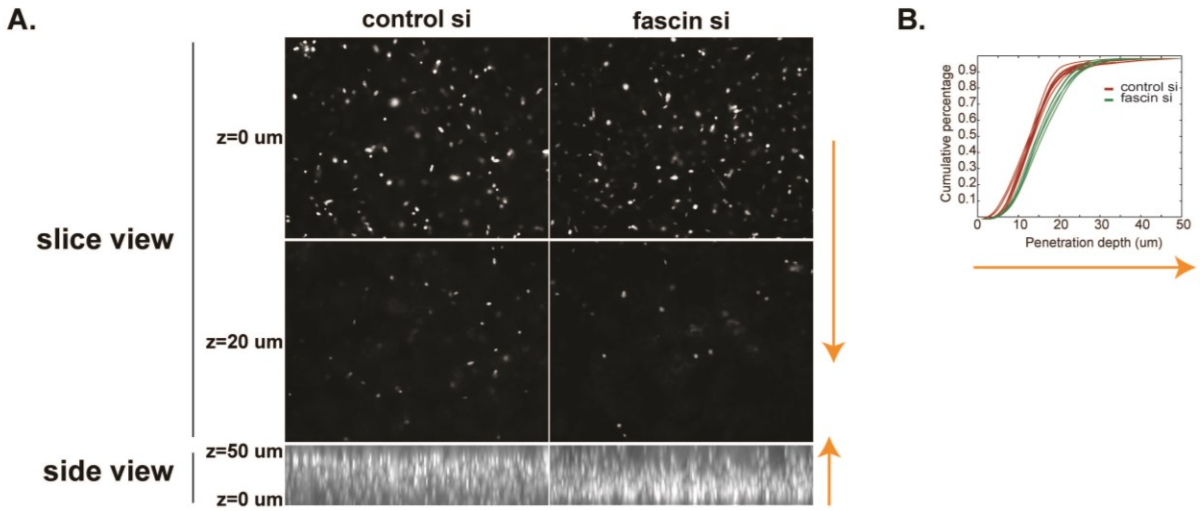

Figure 7. Effect of fascin in three-dimensional invasion in MDA-MB-231 breast carcinoma cells. (A) Top, representative z-slices at 0 and 20 μm from the well bottom for control and fascin knockdown MDA-MB-231 cells. Bottom, side projection of a representative z-stack, from 0 to 50 μm from the well bottom. (C) Cumulative distribution of penetration depth for control and fascin knockdown MDA-MB-231 cells. Each line represents average of z-stacks from one independent experiment. Orange arrows indicate direction in each view, with arrowhead pointing in the direction of invasion.

Discussion

Cancer metastasis at its core requires 1) invasion of cells from primary tumor into the circulatory system, 2) extravasation at a distant site, and 3) survival of a new colony through changes in the microenvironment and angiogenesis (Birchmeier et al., 2003; Yamaguchi et al., 2005). In particular, invasion necessarily means that one or a group of cells in the original tumor becomes more motile as it/they move through the surrounding tissue into a blood or lymph vessel by penetrating one or more basement membranes and endothelial walls. Since the actin cytoskeleton is the key driver of such motility (Mitchison and Cramer, 1996; Mogilner and Oster, 1996a; Pollard, 2003; Yamazaki et al., 2005), there is great interest in studying it and its modulators as cancer targets that prevent metastasis (Olson and Sahai, 2009).

One of the actin modulators that has surfaced as a metastasis marker in multiple cancer types both in human patients (Al-Alwan et al., 2011; Darnel et al., 2009; Xing et al., 2011; Zigeuner et al., 2006) and mouse models (Minn et al., 2005; Nguyen et al., 2009) is fascin. High expression levels of fascin have also been linked to poor clinical prognoses (Hashimoto et al., 2004; Hashimoto et al., 2006; Pelosi et al., 2003; Yoder et al., 2005). Thus far, it has been assumed that at the cellular level these cancer-related functions of fascin are due to its roles in forming invadopodia or, more importantly, filopodia (Hashimoto et al., 2011). However, as our PtK1 and MDA-MB-231 experiments show, there are filopodia-independent shifts in migration and invasion in high-fascin expressing cells.

Fascin templates nascent adhesions

Our study reveals that fascin has a role in the formation of nascent adhesions. Traction force measurements showed that fascin-rich cells link to the substrate via a ‘carpet’ of distributed adhesions that are continually deposited during a protrusion cycle (Fig. 4D). Indeed, live-cell

imaging of the adhesion component paxillin confirmed that cells with high levels of fascin make denser nascent adhesions (Fig. 5B). Importantly, the increased adhesion density is not the result of extended lifetime but of a bona fide increase in nascent adhesion formation. Our finding of elevated protrusion rates in these cells is also in agreement with data presented in (Choi et al., 2008c), demonstrating that protrusion rate and the rate of formation of nascent adhesions are directly coupled. Our data provide evidence that fascin has an active role in the formation of nascent adhesions as fascin is recruited to sites of nascent adhesions even before paxillin, an adaptor protein that is recruited in the early stages (Fig. 5F,G). Other actin cross-linking proteins have been associated with adhesion organization. Most prominently, α-actinin has been shown to play a role in adhesion maturation by organizing actin filaments in a manner that adhesions have "tracks" on which to bring additional adhesion constituents to grow and elongate (Choi et al., 2008c). Our data now adds to this a function for an actin crosslinker as a 'templating component' that prepares the formation of new nascent adhesions rather than enabling their maturation into focal adhesions or modulating their disassembly. In view of their structural differences, it is not surprising that fascin and α-actinin have functions at different points in the lifetime of adhesions. Fascin is a selective crosslinker that uniquely makes tight parallel actin bundles whereas α-actinin crosslinks actin at all angles (Courson and Rock, 2010). Recent investigations of the coordination of different actin nucleator components during the protrusion/retraction cycle of the PtK1 cells used also here showed that nascent adhesions start to form prior to protrusion onset in a process that is dependent on mDia1-mediated elongation of straight actin filaments (Lee et al., submitted). Later in the protrusion cycle, actin polymerization is reinforced by autocatalytic growth of a dendritic network, mediated by activation of the WAVE – Arp2/3 pathway (Lee et al., submitted; Mendoza et al., submitted). Thus, fascin's mode of action is associated with an

early phase of linear bundle formation to initiate adhesion formation, whereas a-actinin operates in the later phase as a cross-linker of linear and branched filaments to stabilize adhesions and promote their maturation.

Data from a recent study has shown that fascin localizes specifically to adhesions in human cancer cells and mouse fibroblasts (Elkhatib et al., 2014). The same study also showed that fascin knockdown cells make significantly more and larger focal adhesions than control cells. At first sight, these observations seem not consistent with the model we propose here. However, we propose that in fascin-rich cells, much of the proteins required for adhesion assembly, especially those in the earlier stages of the adhesion life cycle, are largely used up in the lamellipodia. As a result, fascin-rich cells have less focal adhesions in the lamellipodium/lamella junction than cells with low levels of fascin expression (Elkhatib et al., 2014).

We can speculate how having more nascent adhesions and fewer focal adhesions may promote metastasis in neoplastic cells. It has been observed that rapidly-moving cells such as neutrophils and macrophages have smaller, more dynamic adhesions while more contractile cells such as fibroblasts and endothelial cells have larger, more stable adhesions (Lauffenburger and Horwitz, 1996a). The observation of a direct relationship between cell motility and dynamicity of adhesions has been corroborated by studies in other cell lines subjected to different substrate flexibilities or genetic alterations (Ilic et al., 1995b; Pelham and Wang, 1997). This suggests that enhanced motility in the context of fascin-rich neoplastic cells may be due to the formation of more nascent and fewer focal adhesions.

Fascin-rich cells have extended lamellipodial region of low traction stress

Traction force is a composite of forces from actin polymerization at the leading edge and actomyosin contraction in the cell body. Our traction force measurements indicated that fascin-rich cells have significantly lower traction stress compared to control cells (Fig. 4B). Additionally, the traction stress peaked further into the cell in fascin-rich cells (Fig. 4F). Combined with the nascent adhesions data, this means that fascin-rich cells have a larger lamellipodial region that has high nascent adhesion density and low traction stress.

Optimal traction stress that allows for maximal migration speeds is cell-type dependent (Evans et al., 1993; Harris et al., 1980; Lee et al., 1994). Further experimentation has determined that this optimal stress level also depends on the mechanical properties of the ECM as cell-substrate adhesions are mechanosensitive structures that enable a cell to adapt to the stiffness of the ECM (Katsumi et al., 2004). Of note, there is an inverse relationship between traction stress and migration (Doyle and Lee, 2005; Munevar et al., 2001), which agrees with fascin-rich cells having higher motility and lower traction stress. Therefore, a plausible role of fascin in migration is to enable a cell to better adapt to the ECM by modulating traction stress levels through the formation of nascent adhesions, thereby resulting in faster migration. To definitively show this, more traction force experiments will need to be done in ECM of different rigidities and with multiple cell types.

Reduction in actin retrograde flow in fascin-rich cells account for most of the increase in protrusion velocity

Previous studies have shown actin flow to be slower in adhesion-rich regions, which can be attributed to the fact that there is more mechanical resistance in those regions (Alexandrova et al., 2008; Hu et al., 2007; Ponti et al., 2004). Consistent with this, an inverse relationship between cell advancement and rate of actin flow has been observed (Jurado et al., 2005;

Smilenov, 1999), although conflicting data do exist. Thus, an implication of denser nascent adhesions in fascin-rich cells is that the actin flow in the lamellipodium will be affected. Indeed, our data are in support of the inverse relationship and show that in cells with high levels of fascin, actin retrograde flow is significantly decreased.

Actin polymerization at the leading edge generates a pushing force on the plasma membrane, most likely by the Browninan ratchet mechanism (Theriot, 2000). This pushing force drives membrane protrusions that ultimately results in cell translocation and also drives the whole actin network backward in retrograde actin flow. In our case, cells expressing high levels of fascin were found to have more protrusive activities (Fig. 3). This could mean that actin polymerization occurs at a higher rate or that retrograde actin flow is slower, since reduced actin flow translates into the cell utilizing more of the actin polymerization to drive protrusions. The two scenarios are not mutually exclusive, so the answer likely lies somewhere between the two extremes. Our measure of actin flow does indeed suggest that most of the additional protrusive activities in fascin-rich cells are due to slower retrograde actin flow (Fig. 6B).

In conclusion, the combination of increased nascent adhesion formation, which leads to slower actin retrograde flow, and decreased traction stress, allows for more protrusive activities at the single cell level in fascin-rich cells. In turn, this translates to higher migration rates in two- and three-dimensions. Our results give a cell biological explanation for how fascin increases cell motility, which may lead to high metastasis rates and poor outcomes in patients of numerous cancers with high fascin expression.

Materials and Methods

PtK1 cell culture and imaging conditions. PtK1 cells were cultured in Ham's F12 media (Invitrogen), supplemented with 10% FBS, 0.1 mg/ml streptomycin, 100 U/ml penicillin. They were routinely tested for mycoplasma contamination. Cells were transfected by electroporation using the Neon transfection system (Invitrogen) according to manufacturer's instructions (1 pulse, 1400V, 20ms), and grown on acid-washed glass coverslips from Corning (#1.5 coverslips) for 2 days before imaging. Prior to imaging, expressed HaloTag fusion proteins were labeled by HaloTag-TMR ligand (Promega) according to manufacturer's instructions. For plasma membrane staining, cells were incubated with 1 g/ml CellMask Orange (Invitrogen) for 5 min, and images were acquired within 2 hours. Imaging was performed in imaging medium (Leibovitz's L-15 without phenol red, Invitrogen) supplemented with 10% FBS, 0.1 mg/ml streptomycin, 100 U/ml penicillin, 0.45% glucose, and Oxyrase (1.0 U per ml , Oxyrase Inc.).

Wound healing assay. Migration was tested in wound healing assays using Culture Inserts (ibidi). After cells were grown to confluence, Culture Inserts were removed and imaged every 5 minutes for 18 hours with an inverted Nikon Ti-E microscope with integrated Perfect Focus System with a 20X, objective lens and custom built 37°C microscope incubator enclosure. Percent wound closure was calculated using ImageJ. Leader cells were visually identified for each image sequence.

siRNA knockdown of fascin in PtK1. Tasmanian devil (Sarcophilus harrisii) fascin sequence was used to design siRNA sequences. Two Alexa488-fascin siRNA were custom ordered

(Qiagen). Of those, siRNA sequence GGUGGGCAAGGACGAGCUCTT was confirmed to knockdown fascin with 90% efficiency.

Immunostaining. PtK1 cells grown on acid-washed coverslips for two days were pre-extracted in CB buffer (10mM MES, pH 6.1, 138mM KCl, 3mM $MgCl_2$, 2mM EGTA) with 0.1% Triton-X-100 and 1J.g/ml phalloidin for 1 min. Then, the cells were fixed using 1 % glutaraldehyde in CB for 20 min, followed by two washes with 0.4% NaBH4 in PBS for 15 min each. 3 % BSA in PBS was used for blocking. The fixed cells were incubated with primary antibody (1:100 dilution), followed by incubation with fluorescently conjugated secondary antibody (1:200 dilution) (Invitrogen). After extensive washing, actin was stained with Alexa568 or Alexa647-labeled phalloidin (Invitrogen). Fascin antibody was purchased from Dako (M3567).

Light microscopy. All microscopy except paxillin imaging was performed using an inverted Nikon Ti-E microscope (including motorized focus, objective nosepiece, fluorescence filter turret, and condenser turret) with integrated Perfect Focus System with a 60x, 1.4 NA Plan Apochromat objective lens with 1.5x optovar (for traction force microscopy and dual-color imaging, no optovar was used), motorized stage and focus motor from Prior, and custom built 37°C microscope incubator enclosure mounted on a TMC vibration-isolation table. Confocal images were obtained using a Yokogawa CSU-X1 spinning disk confocal head equipped with an internal motorized high speed emission filter wheel and the Borealis modification (Spectral Applied Research) for increased light throughput and illumination homogeneity. Fluorophores were excited by Spectral Applied Research custom laser merge module (LMM-7) equipped with solid state 561 nm (200 mW) and 642 nm (100 mW) lasers. Excitation and emission

wavelengths were selected and attenuated with an AOTF and a quad Semrock 405/488/561/647 dichroic mirror, respectively. Alexa-568 was visualized using the 561 laser line and 620/60 emission filter; HaloTag-TMR was visualized using the 561 laser line and 605/70 emission filter (Chroma); for traction force microscopy, far-red fluorescent beads were visualized by the 647 laser line and 700/75 emission filter (Chroma). Images were collected with an ORCA-AG cooled CCD camera from Hamamatsu and Metamorph software v7.7 (Molecular Devices) without binning. Exposure times were typically 500 ms using 15~30% laser power.

Paxillin recruitment was imaged by total internal reflection fluorescence microscopy using a Nikon Ti-E inverted motorized microscope with integrated Perfect Focus System, Nikon 100x 1.49 NA TIRF DIC objective lens, and Nikon dual-port TIRF/Epi illuminator with motorized laser incident angle adjustment. For lasers, a Spectral Applied Research laser launch was used with 100mW 401nm, 40mW 442nm, 50mW 491nm, 50mW 515nm, 50mW 561nm and 100mW 640nm solid state lasers with a fiber-optic delivery system and AOTF. A Prior Proscan III controller was used for fast excitation and emission filter wheels, fast transmitted and epi- fluorescence light path shutters, and a linear-encoded motorized stage. A Chroma 405/491/561/638 dichroic mirror was used with a 561 laser line and 600/50 emission filter for HaloTag-TMR. In addition to emission filters, a custom Chroma laser notch filter was used in the emission path to further block the illumination light from reaching the camera and to minimize interference patterns. Images were collected with a Hamamatsu ORCA R2 CCD camera and MetaMorph v7.7 (Molecular Devices). Exposure times were typically 500 ms using 30~50% laser power.

Western blotting. PtK1 cells were grown to 80% confluency and washed twice with ice-cold PBS. Cells were lysed in RIPA buffer (150 mM NaCl, 1.0% Triton X-100, 0.5% sodium deoxycholate, 0.1% SDS, 50 mM Tris, pH 8.0) containing a protease inhibitor cocktail tablet (Roche), and the adherent cells were scraped off the dish using a cold plastic cell scraper. The cell suspension was transferred to a pre-cooled microcentrifuge tube and incubated at 4°C for 30 min with agitation and spun at 13,000 rpm for 20 min at 4°C to isolate the supernatant. Samples were made by adding 1vol of Laemmli Sample Buffer (Bio-Rad) and were run on SDS-PAGE and then transferred to a PVDF membrane by applying 40 volts for 1 h at 4°C. The membrane was briefly washed in TBS-T (50 mM Tris, 150 mM NaCl, 0.05% Tween-20, pH 7.6) and blocked for 1h at room temperature with 5% milk in TBS-T. It was probed with a 1:1000 dilution of primary antibody (anti-mDia1 from Axxora, anti-mDia2 from Art Alberts) for 1 h, washed, probed with a 1:1000 dilution of the anti-rabbit IgG HRP antibody (Abcam) for 1h, and washed again. The membrane was incubated with SuperSignal West Pico chemiluminescent substrate (Thermo Scientific), and the blot was exposed to film for 10 seconds.

Traction force microscopy (TFM). Preparation of soft substrates with far-red fluorescent beads for traction force microscopy is described elsewhere. Briefly, a ~30 μm layer of silicone gel with a refractive index of ~1.49 and Young's modulus of 8 kPa (1:1.4 mixture of parts A and B of QGel 920 by Quantum Silicones; the Young's modulus measured as described elsewhere) was created on a #1.5 cover glass at the bottom of a 35-mm culture dish (WillCo-dish®) by spin-coating and curing at 100 ºC for 2 hrs. The surface of the gel was coated with fibronectin and fluorescent tracer particles (40 nm carboxylated far-red fluorescent beads; excitation/emission 690/720 nm, by Invitrogen, Carlsbad, CA) by 15 min room temperature incubation under a

solution of 50 μg/ml of fibronectin and 100 μg/ml EDC in PBS, pH 7.4, with the particles added to the solution. The culture dishes were washed 3 times with PBS, and PtK1 cells were seeded at a concentration of $0.3x10^6$ per dish. Prior to imaging, cells were stained with CellMask Orange (Invitrogen) as described above. In order to prevent oxygen exchange to minimize photodamage, the imaging chamber was completely sealed. At the end of a TFM experiment, cells must be lifted off the substrates in order to measure the position of the tracer beads when the substrate is not deformed by cellular forces. To accomplish this in a closed chamber, the dish covers were outfitted with inlet and outlet tubing and sealed against the dishes with VALAP, making it possible to inject trypsin into the dish. Images of cells and tracer particles were taken (in two different fluorescence wavebands) every 5 seconds for ~1000 seconds on the Nikon Ti spinning disk confocal microscope with a 60x/1.4 objective. Cells were then removed from the substrate by 1 hr incubation in Trypsin/EDTA (10x, 0.5%, Invitrogen), and images of tracer particles on the deformation-free gel substrate were acquired in the areas where cells and particles were imaged beforehand. Cell traction forces were calculated by comparing images of tracer particles with and without cells on the substrate using the Fourier transform traction cytometry method.

Cell edge tracking and windowing. Rates of protrusion and retraction were obtained from fluorescence images by computational edge tracking using a custom-built software package written in Matlab (Mathworks). Cell edges were segmented by intensity thresholding and cell edge displacements were tracked by applying the mechanical model described elsewhere for morphing the edge between consecutive time points. Probing windows were generated with a window size of 500 nm by 500 nm for protrusion analysis and 1 μm by 1 μm for traction force analysis, respectively. The number of windows along the open cell boundary were held constant.

Therefore, as the length of the boundary changed, the window size changed as well. The corners of the windows followed the cell edge displacement vectors. The basic concepts of sampling image signals in motile cells have been introduced elsewhere. The specifics and validation of a new version of window-based sampling applied for the present study are detailed elsewhere.

Identification of protrusion/retraction segments. This analysis was done as described in Lee et al. Protrusion and retraction segments were identified on a per-window basis. First, the instantaneous edge velocity measured for a particular window was integrated over time, resulting in an edge displacement time series. For further processing, the displacement time series was represented by a smoothing spline filter using the Matlab function csaps() and a smoothing parameter: 0.01. Next, we identified local maxima in the edge displacement curve using the Matlab function findpeaks(). We eliminated minor switches between protrusion and retraction phases by retaining only the highest of the local maxima in a rolling window of 50 seconds. Between every pair of consecutive local maxima we then identified the lowest local minimum, bisecting the interval between the two maxima into a retraction segment lasting from the first local maximum to the local minimum and a protrusion segment lasting from the local minimum to the second local maximum. Protrusion and retraction segments with a distance between endpoints of less than 10 pixels (equals to 720 nm) were discarded. This distance corresponds to ~1.5 the depth of the probing windows, i.e. only protrusion segments that yielded a significant translocation of the region of interest used for fluorescence intensity sampling were considered. For valid protrusion/retraction segments, we then computed the segmental distance, the segmental duration, and the average segmental protrusion/retraction velocity. Distributions

of segmental parameters between different experimental conditions were statistically compared using the two-sample KS (Kolmogorov- Smirnov) test (Matlab function kstest2()).

Nascent adhesion (NA) detection, focal adhesion (FA) segmentation, and adhesion tracking. NAs in paxillin images were detected using an existing algorithm from single particle tracking. Briefly, TMR-paxillin images were filtered using the Laplacian of Gaussian filter followed by local maximum detection. Each local maximum was then fitted with an isotropic Gaussian function (standard deviation: 2.1 pixel) and tested with a goodness of fit test (p=0.05) for outlier removal. FA segmentation was performed based on a combination of Otsu and Rosin thresholding after image preprocessing with noise removal and background subtraction. Segmented areas were categorized as focal contacts (FCs) or FAs based on the area following the criteria prescribed by Gardel et al. (0.24 μm^2 for FCs, 0.6 μm^2 for FAs). NAs ware tracked by the uTrack software using gap closing option (maximum gap = 5 frames) and a Brownian search band of 2-5 pixels. Each track was examined to see if it overlapped with a FC or FA, and if so, the track was labeled as a maturing adhesion. Otherwise, the track was labeled as a failing adhesion.

MDA-MB-231 cell culture. MDA-MB-231 cells were cultured in DMEM (Corning), supplemented with 10% FBS, 0.1 mg/ml streptomycin, 100 U/ml penicillin. They were routinely tested for mycoplasma contamination. For DNA, cells were transfected by electroporation using the Neon transfection system (Invitrogen) according to manufacturer's instructions (4 pulses, 1400V, 10ms). For siRNA, cells were transfected by Lipofectamine RNAiMax (Invitrogen) according to manufacturer's instructions.

Collagen invasion assay. Cells were suspended in 2.3 mg/ml of serum-free liquid bovine collagen at 10^5 cells/ml. 100 µl aliquots were dispensed into black 96-well ViewPlates (PerkinElmer) coated with bovine serum albumin. Plates were centrifuged at 1000 rpm for 5 minutes and incubated in a 37 °C/10% CO_2 tissue culture incubator. Once collagen had polymerized, media containing fetal bovine serum was added on top of the collagen to a final concentration of 5%. After 36-hour incubation at 37 °C in 10% CO_2, cells were fixed and stained for 2 h in 4% formaldehyde solution (Sigma-Aldrich) containing 5 µ g/ml Hoechst33258 nuclear stain (Invitrogen). Confocal z-stacks were collected at 1-µm interval from each well. Nuclear staining in each slice was quantified automatically with algorithm developed in house to determine the distribution of invaded cells.

Conclusion

The work described here has elucidated some of the molecular/cellular mechanisms by which fascin increases cell motility and invasion. This is possibly one clue as to why high fascin expression in different cancers correlates with poor clinical outcomes for cancer patients. The initial hypothesis underlying this work was that fascin's role as the actin bundler in filopodia could not be the complete explanation for previously described motility increases – especially because the roles of filopodia in migration are still unclear in general, and in particular because cell lines with elevated fascin expression yet few filopdia still display increased motility. My results indicate that fascin has the unexpected role of promoting nascent adhesions in the lamellipodia and that fascin-rich cells have reduced traction stress and actin flow. These filopodia-independent cellular changes can explain why fascin-rich cells are able to migrate faster, both collectively and at the single cell level.

Fascin templates nascent adhesions

Our study reveals that fascin has a role in the formation of nascent adhesions. Indeed, traction force measurements suggested that fascin-rich cells may make adhesions continually during a protrusion cycle (Fig. 4D) and live-cell images confirmed that cells with high levels of fascin make denser nascent adhesions without affecting lifetimes (Fig. 5C,E,F). The rate of formation of nascent adhesions is thought to be directly related to protrusion rate (Choi et al., 2008c). Since cells expressing high levels of fascin do indeed protrude more, these cells are expected to form more nascent adhesions. However, our data provide evidence that fascin goes one step further and has an active role in the formation of nascent adhesions. Fluorescence tracking of fascin and paxillin at sites of adhesions suggests fascin is recruited to nascent adhesions before detectable levels of paxillin is recruited. Alpha-actinin, another actin crosslinker, has been previously

shown to play a role in adhesion maturation by organizing actin filaments in a manner in which adhesions have "tracks" on which to bring additional adhesion constituents to grow and elongate (Choi et al., 2008c). Our model adds to this with a model in which an actin crosslinker has a role in the early dynamics of adhesions rather than later stages such as maturation into focal adhesions or disassembly of adhesions.

Data from a recent study has shown that fascin localizes specifically to adhesions in human cancer cells and mouse fibroblasts (Elkhatib et al., 2014). The same study also showed that fascin knockdown cells make significantly more and larger focal adhesions than control cells. We believe this to be a repercussion of the fact that high levels of fascin lead to denser nascent adhesions. In fascin-rich cells, much of the proteins associated with the adhesome, especially those required in the earlier stages of the adhesion life cycle, will be depleted in the lamellipodia. Thus, due to this depletion effect, fascin-rich cells have less focal adhesions in the lamellipodium/lamella junction, which we observed. Conversely, fascin-poor cells are expected to have more and larger focal adhesions.

We can speculate how having more nascent adhesions and fewer focal adhesions may promote metastasis in neoplastic cells. It has been observed that rapidly-moving cells such as neutrophils and macrophages have smaller, more dynamic adhesions while more contractile cells such as fibroblasts and endothelial cells have larger, more stable adhesions (Lauffenburger and Horwitz, 1996a). This observation of direct relationship between cell motility and dynamicity of adhesions has been made in other cell lines subjected to different substrate flexibilities or genetic alterations (Ilic et al., 1995b; Pelham and Wang, 1997). This suggests that enhanced motility in the context of fascin-rich neoplastic cells may be due to having more nascent adhesions and fewer focal adhesions.

Moreover, different cell types have different optimal traction stress that allows for maximal migration speeds (Evans et al., 1993; Harris et al., 1980; Lee et al., 1994). Further experimentation has determined that this stress level depends largely on cell type and mechanical properties of the ECM as cell-substrate adhesions are mechanosensitive structures that enable a cell to adapt to the stiffness of the ECM. Of note, there seems to be an inverse relationship between traction stress and migration (Doyle and Lee, 2005; Munevar et al., 2001), which agrees with fascin-rich cells having higher motility and lower traction stress. Combining past observations with regard to adhesions and traction stress, we can speculate that perhaps one role of fascin in migration is to enable a cell to better adapt to the ECM by modulating traction stress levels through the formation of nascent adhesions, thereby resulting in faster migration. To definitively show this, more traction force experiments will need to be done in ECM of different rigidities and with multiple cell types.

Reduction in actin retrograde flow in fascin-rich cells account for most of the increase in protrusion velocity

Previous studies have shown actin flow to be slower in adhesion-rich regions, which can be attributed to the fact that there is more mechanical resistance in those regions (Alexandrova et al., 2008; Hu et al., 2007; Ponti et al., 2004). Consistent with this, an inverse relationship between advancement of cell and rate of actin flow has been observed (Jurado et al., 2005; Smilenov, 1999), although conflicting data do exist. Thus, an implication of denser nascent adhesions in fascin-rich cells is that the actin flow in the lamellipodium will be affected. Indeed, our data are in support of the inverse relationship and show that in cells with high levels of fascin, actin retrograde flow is significantly decreased.

Actin polymerization at the leading edge generates a pushing force on the plasma membrane, most likely by the Brownian ratchet mechanism (Alberts and Odell, 2004; Mogilner and Oster, 1996b). This pushing force drives membrane protrusions that ultimately result in cell translocation and also drives the whole actin network backward in retrograde actin flow. In our case, cells expressing high levels of fascin were found to have more protrusive activities (Fig. 3). This could mean that actin polymerization occurs at a higher rate or that retrograde actin flow is slower, since reduced actin flow translates into the cell utilizing more of the actin polymerization to drive protrusions. The two scenarios are not mutually exclusive, so the answer likely lies somewhere between the two extremes. Our measure of actin flow does indeed suggest that most of the additional protrusive activities in fascin-rich cells are due to slower retrograde actin flow (Fig. 6B). However, not all of the differences in protrusion velocities are accounted for by actin retrograde flow, so increased actin polymerization is like to also plays a role. Thus, our study provides evidence that at least part of the mechanism by which fascin promotes cell motility is by decreasing actin retrograde flow as a consequence of increased nascent adhesion density.

Fascin may have different roles in different stages of metastasis

It is worth revisiting the steps of metastasis at this point: First, tumor cells locally invade into the adjacent tissue. Then, some of these cells intravasate into vessels via transendothelial migration. Next, cancer cells must be able to survive in circulation and eventually extravasate. Finally, successful colonization requires that the cells be able to proliferate at the new site (Mehlen and Puisieux, 2006). The initial steps that involve increased cell motility is an area of intense research, but no one has yet systematically shown that migration is the rate limiting step in metastasis. It could very well be that the rate limiting step is survival. Even if this is true, it does not preclude fascin from playing a critical role in promoting metastasis, especially given recent

work from Robert Weinberg's laboratory (Shibue et al., 2012). Shibue and colleagues showed in three-dimensional cultures of mouse mammary carcinoma cells that one mechanism by which cancer cells increase survival and proliferation within the post-extravasation tissue is through the formation of filopodia-like structures that have integrins along the shaft, allowing for the assembly of mature adhesion plaques that activate pro-survival, pro-proliferation signals. Given that fascin is a filopodia marker and that high levels of fascin promotes the formation of filopodia, it is not unreasonable to speculate that fascin could also increase survival and proliferation through similar mechanisms.

In the present work, we have shown filopodia-independent roles of fascin in promoting cell motility that complement the filopodia-centric models. This ascribes a dual role to fascin in several cell structures and functions that are all supporting metastasis. On the one hand, filopodia-independent functions of fascin such as nascent adhesion formation allow a cell to migrate faster and more. On the other hand, filopodia-related functions of fascin enhance survival of new colonies and also likely have roles in increasing migration. Combining the two, fascin-overexpressing cells could have both high extravasation rate and increased survival and proliferation in a new microenvironment, tissue, or organ.

Future work

The present work leaves many questions to be answered and technical hurdles to be overcome. To further elucidate fascin's effect on cell motility, more work needs to be done to biochemically characterize its effect on adhesions, establish relevance in multiple human cancers, and achieve high resolution imaging in three-dimensions.

Biochemical characterization of fascin's effect on nascent adhesions

My work has indicated that one of the mechanisms by which fascin might have the pathophysiological effect of promoting cell motility is through cellular adhesions to the extracellular matrix. But how exactly is an actin bundling protein having such an effect?

To that end, biochemical experiments and screens are necessary to definitively establish the proteins involved in this phenomenon. Although not within the scope of this thesis work, it would be interesting to see whether or not there are any direct molecular interactions between fascin or fascin-bundled actin and any cell adhesion molecules. Such work is needed to advance the field, as it is likely that not all binding partners to fascin are known. Both published and unpublished recent work on fascin from multiple labs suggest that fascin has many more binding partners than is suggested by the current literature and that it has a role in adhesions, in focal adhesions as well as intercellular adhesions.

One hypothesis that could explain fascin's effect of promoting nascent adhesions is that it directly interacts with proteins such as paxillin that are recruited to the cell-substrate adhesion in the early stages(Laukaitis et al., 2001). Paxillin is a scaffolding protein and contains a number of phosphorylation sites for kinases (including protein kinase C) and is phosphorylated in response to various stimuli (Deakin and Turner, 2008). It is known that such phosphorylation events

influence paxillin localization to adhesions. A direct interaction with fascin or fascin-bundled actin could inhibit some of the phosphorylation events, thereby changing paxillin localization and/or activity.

Another hypothesis is that the effect of fascin promotes nascent adhesions not through direct molecular interactions with proteins of the adhesome but through a templating effect via actin bundles. This would parallel the past finding that alpha-actinin, another actin bundler, promotes adhesion maturation by making actin tracks onto which other proteins are recruited (Choi et al., 2008a).

Establishment of universality in other cell lines

The model systems used in the present studies are kidney epithelial cells from a marsupial organism and human breast cancer cells. Epithelial cells are especially relevant because most cancers are cancers of the epithelial cells, making up between 80-90 of every 100 cancers (Cancer Research UK). There was good agreement in results between the two cell lines used, especially with regard to fascin's effect on adhesions in largely filopodia-free cells. Given that marsupials and primates are evolutionarily distinct groups of mammals, it is likely that the findings apply to other cells.

However, in order to establish universality of the results described here, more experiments will need to be done in other cells, especially various forms of human carcinoma. To that end, a screen with established cell lines and/or primary cells representing different carcinomas will be useful. It may be difficult to do high resolution imaging studies with cancer cells, depending on their morphology. However, the three-dimensional collagen assay described here will be

amenable to most cell lines in measuring migration such that migration rate can be related to fascin expression levels.

High-resolution, three-dimensional imaging studies

Much of the high-resolution imaging studies in this work has been two-dimensional studies of cells plated on a glass cover slip. However, life is three-dimensional. As such, there has been increasing interest recently in developing the tools necessary for high-resolution three-dimensional imaging studies.

There are several difficulties associated with executing high resolution quantitative live cell imaging studies in three dimensions. The first hurdle is the cell culture itself. Numerous options exist currently for culturing cells in three-dimensions, including natural polymers such as collagen, gelatin, hyaluronate, and Matrigel and synthetic polymers such as polyglycolic acid, polylactic acid, and polyethylene glycol (Lee et al., 2008). Each cell type is found in a microenvironment with different mechanical properties and has a unique set of interactions with it, so careful considerations of such factors must be made before deciding on the culture medium. The next obstacle is the microscope. Here again, there have been some recent developments with the advent of technology such as light sheet microscopy (Planchon et al., 2011; Vettenburg et al., 2014) that allows for deep penetration of the sample volume at isotropic resolution and minimizes photobleaching without large sacrifices in temporal resolution. The final hurdle is a computer algorithm that can quantify a number of desired parameters such as cell shape and fluorescence/migration activities, as can be done in two-dimensions. Notwithstanding these difficulties, there is immense interest among cell biologists in being able to observe some of the well-accepted two-dimensional phenomena in three-dimensions.

For the purposes of studying fascin, it will be interesting to see how adhesion morphology compares between two- and three-dimensional states. Rapidly-moving cells have been observed not to form any adhesions in three-dimensions (Friedl et al., 1998). Will the more rapidly-moving fascin-rich cells lack adhesions that the control counterparts have? To answer such questions, the employment of latest microscopy technology such as light sheet microscopy may be necessary. In addition, it will most likely be necessary to optimize ECM parameters and find a material that is optimized for showing adhesions, since properties of the ECM will affect how cells and substrates interact with each other. If it is determined that three-dimensional quantitation of phenotype is necessary, tailored algorithms must be developed.

And beyond…

Outlining the molecular mechanisms of fascin is a useful goal. However, the eventual end goal of most biomedical studies is not only to explain what a particular protein is doing in a cell but how we might inhibit its pathological activities to help patients and improve patient outcomes. If it is indeed determined that fascin plays a critical role in one or more of the steps to metastasis, the next natural step is the search for a drug that targets fascin and has the effect of preventing or decreasing the rate of metastasis. For this to be achieved, there will need to be collaborative efforts between biologists and chemists of many different fields.

First and foremost, we do not yet have a molecular structure of fascin bound to actin, and it is only postulated that there are two or more actin binding sites on the protein (Jansen et al., 2011). A structure of fascin actually bound to actin will be instrumental in identifying possible sites of drug target. Furthermore, screens will need to be set up that are specific to identifying “hits” for inhibitors of fascin. The difficulty in setting up such screens, of course, will be the determination of the right model system and the end point. Using tailored automation, an assay such as the

collagen invasion assay in MDA-MB-231 may be a good start. With the structure and the results of the screen at hand, medicinal chemists may then be able to optimize the initial hits in regards to parameters such as bioavailability, stability, pharmacokinetics, and pharmacodynamics. Because high fascin expression level has been correlated with increased metastasis and poor patient outcomes in so many different cancers, collaborations between industry and academia will benefit both and greatly accelerate the arduous process.

References

Al-Alwan, M., Olabi, S., Ghebeh, H., Barhoush, E., Tulbah, A., Al-Tweigeri, T., Ajarim, D., and Adra, C. (2011). Fascin is a key regulator of breast cancer invasion that acts via the modification of metastasis-associated molecules. PLoS One *6*, e27339.

Alberts, J.B., and Odell, G.M. (2004). In silico reconstitution of Listeria propulsion exhibits nano-saltation. PLoS biology *2*, e412.

Alexandrova, A.Y., Arnold, K., Schaub, S., Vasiliev, J.M., Meister, J.J., Bershadsky, A.D., and Verkhovsky, A.B. (2008). Comparative dynamics of retrograde actin flow and focal adhesions: formation of nascent adhesions triggers transition from fast to slow flow. PloS one *3*, e3234.

Anilkumar, N., Parsons, M., Monk, R., Ng, T., and Adams, J.C. (2003). Interaction of fascin and protein kinase Calpha: a novel intersection in cell adhesion and motility. EMBO J *22*, 5390-5402.

Aratyn, Y.S., Schaus, T.E., Taylor, E.W., and Borisy, G.G. (2007). Intrinsic dynamic behavior of fascin in filopodia. Mol Biol Cell *18*, 3928-3940.

Arthur, W.T., and Burridge, K. (2001). RhoA Inactivation by p190RhoGAP Regulates Cell Spreading and Migration by Promoting Membrane Protrusion and Polarity. Molecular Biology of the Cell *12*, 2711-2720.

Bear, J.E., Svitkina, T.M., Krause, M., Schafer, D.A., Loureiro, J.J., Strasser, G.A., Maly, I.V., Chaga, O.Y., Cooper, J.A., Borisy, G.G*., et al.* (2002). Antagonism between Ena/VASP proteins and actin filament capping regulates fibroblast motility. Cell *109*, 509-521.

Birchmeier, C., Birchmeier, W., Gherardi, E., and Vande Woude, G.F. (2003). Met, metastasis, motility and more. Nature reviews Molecular cell biology *4*, 915-925.

Bisi, S., Disanza, A., Malinverno, C., Frittoli, E., Palamidessi, A., and Scita, G. (2013). Membrane and actin dynamics interplay at lamellipodia leading edge. Curr Opin Cell Biol *25*, 565-573.

Block, J., Breitsprecher, D., Kuhn, S., Winterhoff, M., Kage, F., Geffers, R., Duwe, P., Rohn, J.L., Baum, B., Brakebusch, C*., et al.* (2012). FMNL2 drives actin-based protrusion and migration downstream of Cdc42. Curr Biol *22*, 1005-1012.

Bray, D. (1970). The surface movement during growth of single explanted neurons. PNAS *65*, 905-910.

Breitsprecher, D., Koestler, S.A., Chizhov, I., Nemethova, M., Mueller, J., Goode, B.L., Small, J.V., Rottner, K., and Faix, J. (2011). Cofilin cooperates with fascin to disassemble filopodial actin filaments. J Cell Sci *124*, 3305-3318.

Bryan, J. (1978). Separation and interaction of the major components of sea urchin actin gel. J Mol Biol *125*, 207-224.

Buccione, R., Orth, J.D., and McNiven, M.A. (2004). Foot and mouth: podosomes, invadopodia and circular dorsal ruffles. Nature reviews Molecular cell biology *5*, 647-657.

Butler, J.P., Tolic-Norrelykke, I.M., Fabry, B., and Fredberg, J.J. (2002). Traction fields, moments, and strain energy that cells exert on their surroundings. American journal of physiology Cell physiology *282*, C595-605.

Campellone, K.G., and Welch, M.D. (2010). A nucleator arms race: cellular control of actin assembly. Nature reviews Molecular cell biology *11*, 237-251.

Cancer Research UK (http://www.cancerresearchuk.org/cancer-help/about-cancer/what-is-cancer/cells/types-of-cells-and-cancer).

Cater, S.B., and Rehder, V. (1995). The sensory-motor role of growth cone filopodia. Curr Opin Neurobiol *5*, 68-74.

Chaudhuri, O., Parekh, S.H., and Fletcher, D.A. (2007). Reversible stress softening of actin networks. Nature *445*, 295-298.

Choi, C.K., A, and A (2008a). Actin and α-actinin orchestrate the assembly and maturation of nascent adhesions in a myosin II motor-independent manner. Nature cell biology *10*, 1039–1050.
Choi, C.K., Vicente-Manzanares, M., Zareno, J., Whitmore, L.A., Mogilner, A., and Horwitz, A.R. (2008b). Actin and alpha-actinin orchestrate the assembly and maturation of nascent adhesions in a myosin II motor-independent manner. Nature cell biology *10*, 1039-1050.
Choi, C.K., Vicente-Manzanares, M., Zareno, J., Whitmore, L.A., Mogilner, A., and Horwitz, A.R. (2008c). Actin and α-actinin orchestrate the assembly and maturation of nascent adhesions in a myosin II motor-independent manner. Nat Cell Biol *10*, 1039-1050.
Condeelis, J. (1993). Life at the Leading Edge: The Formation of Cell Protrusions. Annu Rev Cell Biol *9*, 411-444.
Courson, D.S., and Rock, R.S. (2010). Actin cross-link assembly and disassembly mechanics for alpha-Actinin and fascin. The Journal of biological chemistry *285*, 26350-26357.
Cramer, L.P., Mitchison, T.J., and Theriot, J.A. (1994). Actin-dependent motile forces and cell motility. Curr Opin Cell Biol *6*, 82-86.
Cramer, L.P., Siebert, M., and Mitchison, T.J. (1997). Identifi cation of novel graded polarity actin filament bundles in locomoting heart fibroblasts. J Cell Biol *136*, 1287-1305.
Danuser, G. (2011). Computer vision in cell biology. Cell *147*, 973-978.
Darnel, A.D., Behmoaram, E., Vollmer, R.T., Corcos, J., Bijian, K., Sircar, K., Su, J., Jiao, J., Alaoui-Jamali, M.A., and Bismar, T.A. (2009). Fascin regulates prostate cancer cell invasion and is associated with metastasis and biochemical failure in prostate cancer. Clin Cancer Res *15*, 1376-1383.
Deakin, N.O., and Turner, C.E. (2008). Paxillin comes of age. J Cell Sci *121*, 2435-2444.
Dembo, M., and Wang, Y. (1999a). Stresses at the Cell-to-Substrate Interface during Locomotion of Fibroblast. BIOPHYSICAL JOURNAL *76*, 2307–2316.
Dembo, M., and Wang, Y. (1999b). Stresses at the Cell-to-Substrate Interface during Locomotion of Fibroblasts. Biophysical journal *76*, 2307–2316.
Dent, E.W., Gupton, S.L., and Gertler, F.B. (2011). The growth cone cytoskeleton in axon outgrowth and guidance. Cold Spring Harb Perspect Biol *3*.
DeRosier, D., Mandelkow, E., and Silliman, A. (1977). Structure of actin-containing filaments from two types of non-muscle cells. J Mol Biol *113*, 679-695.
Dominguez, R., and Holmes, K.C. (2011). Actin structure and function. Annu Rev Biophys *40*, 169-186.
Dos Remedios, C.G., Chhabra, D., Kekic, M., and Dedova, I.V. (2003). Actin Binding Proteins-Regulation of Cytoskeletal Microfilaments. Physiol Rev *83*, 433–473.
Doyle, A.D., and Lee, J. (2005). Cyclic changes in keratocyte speed and traction stress arise from Ca2+-dependent regulation of cell adhesiveness. J Cell Sci *118*, 369-379.
Duh, F.M., Latif, F., Weng, Y., Geil, L., Modi, W., Stackhouse, T., Matsumura, F., Duan, D.R., Linehan, W.M., Lerman, M.I.*, et al.* (1994). cDNA cloning and expression of the human homolog of the sea urchin fascin and Drosophila singed genes which encodes an actin-bundling protein. DNA Cell Biol *13*, 821-827.
Elkhatib, N., Neu, M.B., Zensen, C., Schmoller, K.M., Louvard, D., Bausch, A.R., Betz, T., and Vignjevic, D.M. (2014). Fascin plays a role in stress fiber organization and focal adhesion disassembly. Curr Biol *24*, 1492-1499.
Elliott, H.L., S. Chen, K. Lee, M. Mendoza, S. Besson, G. Danuser (2012). Quantification of image patterns in dynamic and variable cell shapes. Submitted.
Enterline, H.T., and Coman, D.R. (1950). The ameboid motility of human and animal neoplastic cells. Cancer *3*, 1033-1038.
Evans, A., a, and a (1993). Synchrony of cell spreading and contraction force as phagocytes engulf large pathogens. J Cell Biol *122*, 1295-1300.
Farina, K.L., Wyckoff, J.B., and Rivera, J. (1998). Cell motility of tumor cells visualized in living intact primary tumors using green fluorescent protein. Cancer Res *58*, 2528-2532.

Fletcher, D.A., and Mullins, R.D. (2010). Cell mechanics and the cytoskeleton. Nature *463*, 485-492.
Forscher, P., Lin, C.H., and Thompson, C. (1992). Novel form of growth cone motility involving site-directed actin filament assembly. Nature *357*, 515-518.
Friedl, P., a, and a (1998). Cell migration strategies in 3-D extracellular matrix: Differences in morphology, cell matrix interactions, and integrin function. Microscopy Res and Tech *43*, 369–378.
Friedl, P., a, and a (2001). Amoeboid leukocyte crawling through extracellular matrix: lessons from the Dictyostelium paradigm of cell movement. J Leukocyte Biol *70*, 491-509.
Friedl, P., and Gilmour, D. (2009). Collective cell migration in morphogenesis, regeneration and cancer. Nature reviews Molecular cell biology *10*, 445-457.
Friedl, P., and Wolf, K. (2003). Tumour-cell invasion and migration: diversity and escape mechanisms. Nature reviews Cancer *3*, 362-374.
Gao, W., Zhang, C., Feng, Y., Chen, G., Wen, S., Huangfu, H., and Wang, B. (2012). Fascin-1, ezrin, and paxilin contribute to the malignant progress and are predictors of clinical prognosis in laryngeal squamous cell carcinoma. PLoS One *7*.
Gardel, M.L., Sabass, B., Ji, L., Danuser, G., Schwarz, U.S., and Waterman, C.M. (2008). Traction stress in focal adhesions correlates biphasically with actin retrograde flow speed. The Journal of cell biology *183*, 999-1005.
Gauthier, N.C., Fardin, M.A., Roca-Cusachs, P., and Sheetz, M.P. (2011). Temporary increase in plasma membrane tension coordinates the activation of exocytosis and contraction during cell spreading. Proc Natl Acad Sci U S A *108*, 14467-14472.
Ghosh, M., Song, X., Mouneimne, G., Sidani, M., Lawrence, D.S., and Condeelis, J.S. (2004). Cofilin promotes actin polymerization and defines the direction of cell motility. Science *304*, 743-746.
Gimona, M., Buccione, R., Courtneidge, S.A., and Linder, S. (2008). Assembly and biological role of podosomes and invadopodia. Curr Opin Cell Biol *20*, 235-241.
Greenburg, G., and Hay, E.D. (1982). Epithelia suspended in collagen gels can lose polarity and express characteristics of migrating mesenchymal cells. J Cell Biol *95*, 333-339.
Gupton, S.L., Eisenmann, K., Alberts, A.S., and Waterman-Storer, C.M. (2007). mDia2 regulates actin and focal adhesion dynamics and organization in the lamella for efficient epithelial cell migration. J Cell Sci *120*, 3475-3487.
Gupton, S.L., and Waterman-Storer, C.M. (2006). Spatiotemporal feedback between actomyosin and focal-adhesion systems optimizes rapid cell migration. Cell *125*, 1361-1374.
Gutierrez, E., Tkachenko, E., Besser, A., Sundd, P., Ley, K., Danuser, G., Ginsberg, M.H., and Groisman, A. (2011). High refractive index silicone gels for simultaneous total internal reflection fluorescence and traction force microscopy of adherent cells. PLoS One *6*, e23807.
Hanker, L., Karn, T., Holtrich, U., Graeser, M., Becker, S., Reinhard, J., Ruckhaberle, E., Gevensleben, H., and Rody, A. (2013). Prognostic impact of fascin-1 (FSCN1) in epithelial ovarian cancer. Anticancer Research *33*, 371-378.
Harris, A.K., a, a, and a (1980). Silicone rubber substrata:a new wrinkle in the study of cell locomotion. Science *208*, 177-179.
Hashimoto, Y., Kim, D.J., and Adams, J.C. (2011). The roles of fascins in health and disease. J Pathol *224*, 289-300.
Hashimoto, Y., Shimada, Y., Kawamura, J., Yamasaki, S., and Imamura, M. (2004). The prognostic relevance of fascin expression in human gastric carcinoma. Oncology *67*, 262-270.
Hashimoto, Y., Skacel, M., Lavery, I.C., Mukherjee, A.L., Casey, G., and Adams, J.C. (2006). Prognostic significance of fascin expression in advanced colorectal cancer: an immunohistochemical study of colorectal adenomas and adenocarcinomas. BMC Cancer *6*, 241.
Heneen, W.K. (1970). In situ Analysis of Normal and Abnormal Patterns of the mitotic apparatus in cultured rat kangaroo cells. Chromosoma *29*, 88-117.

Hooke, R. (1665). Micrographia.
Hotulainen, P., and Lappalainen, P. (2006). Stress fibers are generated by two distinct actin assembly mechanisms in motile cells. J Cell Biol *173*, 383-394.
Houk, A.R., Jilkine, A., Mejean, C.O., Boltyanskiy, R., Dufresne, E.R., Angenent, S.B., Altschuler, S.J., Wu, L.F., and Weiner, O.D. (2012). Membrane tension maintains cell polarity by confining signals to the leading edge during neutrophil migration. Cell *148*, 175-188.
Howard, J. (2001). Mechanics of Motor Proteins and the Cytoskeleton (Sunderland, MA, USA: Sinauer Associates).
Hu, K., Ji, L., Applegate, K.T., Danuser, G., and Waterman-Storer, C.M. (2007). Differential transmission of actin motion within focal adhesions. Science *315*, 111-115.
Ilic, D., A., A., and A. (1995a). Reduced cell motility and enhanced focal adhesion contact formation in cells from FAK-deficient mice. Nature *377*, 539-544.
Ilic, D., Furuta, Y., Kanazawa, S., Takeda, N., Sobue, K., Nakatsuji, N., Nomura, S., Fujimoto, J., Okada, M., Yamamoto, T.*, et al.* (1995b). Reduced cell motility and enhanced focal adhesion contact formation in cells from FAK-deficient mice. Nature *377*, 539-544.
Ingram, V.M. (1969). A Side View of Moving Fibroblasts. Nature *222*, 641-644.
Iskratsch, T., Yu, C.H., Mathur, A., Liu, S., Stevenin, V., Dwyer, J., Hone, J., Ehler, E., and Sheetz, M. (2013). FHOD1 is needed for directed forces and adhesion maturation during cell spreading and migration. Dev Cell *27*, 545-559.
Iwaya, K., Norio, K., and Mukai, K. (2007a). Coexpression of Arp2 and WAVE2 predicts poor outcome in invasive breast carcinoma. Mod Pathol *20*, 339-343.
Iwaya, K., Oikawa, K., Semba, S., Tsuchiya, B., Mukai, Y., Otsubo, T., Nagao, T., Izumi, M., Kuroda, M., Domoto, H.*, et al.* (2007b). Correlation between liver metastasis of the colocalization of actin-related protein 2 and 3 complex and WAVE2 in colorectal carcinoma. Cancer Sci *98*, 992-999.
Jaiswal, R., Breitsprecher, D., Collins, A., Correa, I.R., Jr., Xu, M.Q., and Goode, B.L. (2013). The formin Daam1 and fascin directly collaborate to promote filopodia formation. Curr Biol *23*, 1373-1379.
Jansen, S., Collins, A., Yang, C., Rebowski, G., Svitkina, T., and Dominguez, R. (2011). Mechanism of actin filament bundling by fascin. The Journal of biological chemistry *286*, 30087-30096.
Jaqaman, K., Loerke, D., Mettlen, M., Kuwata, H., Grinstein, S., Schmid, S.L., and Danuser, G. (2008). Robust single-particle tracking in live-cell time-lapse sequences. Nature methods *5*, 695-702.
Jayo, A., Parsons, M., and Adams, J.C. (2012). A novel Rho-dependent pathway that drives interaction of fascin-1 with p-Lin-11/Isl-1/Mec-3 kinase (LIMK) 1/2 to promote fascin-1/actin binding and filopodia stability. BMC Biol *10*, 72.
Ji, L., Lim, J., and Danuser, G. (2008). Fluctuations of intracellular forces during cell protrusion. Nat Cell Biol *10*, 1393-1400.
Jurado, C., Haserick, J.R., and Lee, J. (2005). Slipping or Gripping-Fluorescent Speckle Microscopy in Fish Keratocytes Reveals Two Different Mechanisms for Generating a Retrograde Flow of Actin. Molecular Biology of the Cell *16*, 507-518.
Kafri, R., Springer, M., and Pilpel, Y. (2009). Genetic redundancy: new tricks for old genes. Cell *136*, 389-392.
Kanda, M., Matthaei, H., Wu, J., Hong, S.M., Yu, J., Borges, M., Hruban, R.H., Maitra, A., Kinzler, K., Vogelstein, B.*, et al.* (2012). Presence of somatic mutations in most early-stage pancreatic intraepithelial neoplasia. Gastroenterology *142*, 730-733 e739.
Kaneda, A., Kaminishi, M., Sugimura, T., and Ushijima, T. (2004). Decreased expression of the seven ARP2/3 complex genes in human gastric cancers. Cancer Lett *212*, 203-210.
Katsumi, A., Orr, A.W., Tzima, E., and Schwartz, M.A. (2004). Integrins in mechanotransduction. The Journal of biological chemistry *279*, 12001-12004.

Kim, D.H., Bae, J., Lee, J.W., Kim, S.Y., Kim, Y.H., Bae, J.Y., Yi, J.K., Yu, M.H., Noh, D.Y., and Lee, C. (2009). Proteomic analysis of breast cancer tissue reveals upregulation of actin-remodeling proteins and its relevance to cancer invasiveness. Proteomics Clin Appl *3*, 30-40.
Kim, S.J., Kim, D.C., Kim, M.C., Jung, G.J., Kim, K.H., Jang, J.S., Kwon, H.C., Kim, Y.M., and Jeong, J.S. (2012). Fascin expression is related to poor survival in gastric cancer. Pathol Int *62*, 777-784.
Kong, D., Li, Y., Wang, Z., and Sarkar, F.H. (2011). Cancer Stem Cells and Epithelial-to-Mesenchymal Transition (EMT)-Phenotypic Cells: Are They Cousins or Twins? Cancers (Basel) *3*, 716-729.
Kulasingam, V., and Diamandis, E.P. (2013). Fascin-1 is a novel biomarker of aggressiveness in some carcinomas. BMC Med *11*, 53.
Lacayo, C.I., Pincus, Z., VanDuijn, M.M., Wilson, C.A., Fletcher, D.A., Gertler, F.B., Mogilner, A., and Theriot, J.A. (2007). Emergence of large-scale cell morphology and movement from local actin filament growth dynamics. PLoS Biol *5*, e233.
Ladoux, B., and Nicolas, A. (2012). Physically based principles of cell adhesion mechanosensitivity in tissues. Rep Prog Phys *75*, 116601.
Lauffenburger, D.A., and Horwitz, A.F. (1996a). Cell migration: a physically integrated molecular process. Cell *84*, 359–369.
Lauffenburger, D.A., and Horwitz, A.F. (1996b). Cell migration: a physically integrated molecular process. Cell *84*, 359-369.
Laukaitis, C.M., A, and a (2001). Differential dynamics of alpha 5 integrin, paxillin, and alpha-actinin during formation and disassembly of adhesions in migrating cells. J Cell Biol *153*, 1427–1440.
Lee, J., a, a, and a (1994). Traction forces generated by locomoting keratocytes. J Cell Biol *127*, 1957-1964.
Lee, J., Cuddihy, M.J., and Kotov, N.A. (2008). Three-dimensional cell culture matrices: state of the art. Tissue engineering Part B, Reviews *14*, 61-86.
Lee, K., Gallop, J.L., Rambani, K., and Kirschner, M.W. (2010). Self-assembly of filopodia-like structures on supported lipid bilayers. Science *329*, 1341-1345.
Lee, K., Hunter, E., and Oak, Y. (submitted).
Levan, A., Nichols, W.W., Peluse, M., and Coriell, L.L. (1966). The stemline chromosomes of three cell lines representing different vertebrate classes. Chromosoma *18*, 343-358.
Levan, G. (1970). Contributions to the chromosomal characterization of the PTK 1 rat-kangaroo cell line.
Li, B., Xie, L., Starr, Z.C., Yang, Z., Lin, J.S., and Wang, J.H. (2007). Development of micropost force sensor array with culture experiments for determination of cell traction forces. Cell Motil Cytoskeleton *64*, 509-518.
Lim, J.I., Sabouri-Ghomi, M., Machacek, M., Waterman, C.M., and Danuser, G. (2010). Protrusion and actin assembly are coupled to the organization of lamellar contractile structures. Experimental cell research *316*, 2027-2041.
Lin, C., and Forscher, P. (1995). Growth cone advance is inversely proportional to retrograde f-actin flow. Neuron *14*, 763-771.
Ma, Y., Li, A., Faller, W.J., Libertini, S., Fiorito, F., Gillespie, D.A., Sansom, O.J., Yamashiro, S., and Machesky, L.M. (2013). Fascin 1 is transiently expressed in mouse melanoblasts during development and promotes migration and proliferation. Development *140*, 2203-2211.
Machacek, M., Hodgson, L., Welch, C., Elliott, H., Pertz, O., Nalbant, P., Abell, A., Johnson, G.L., Hahn, K.M., and Danuser, G. (2009). Coordination of Rho GTPase activities during cell protrusion. Nature *461*, 99-103.
Machesky, L.M., and Insall, R.H. (1998). Scar1 and the related Wiskott-Aldrich syndrome protein, WASP, regulate the actin cytoskeleton through the Arp2/3 complex. Curr Biol *8*, 1347-1356.

Mao, X., Chen, D., Wu, J., Li, J., Zhou, H., Wu, Y., and Duan, X. (2013). Differential expression of fascin, E-cadherin and vimentin, Proteins associated with survival of cholangiocarcinoma patients. Clinical Investigation *346*.
Marcy, Y., Prost, J., Carlier, M.F., and Sykes, C. (2004). Forces generated during actin-based propulsion: a direct measurement by micromanipulation. Proc Natl Acad Sci U S A *101*, 5992-5997.
Mattila, P.K., and Lappalainen, P. (2008). Filopodia: molecular architecture and cellular functions. Nature reviews Molecular cell biology *9*, 446-454.
Mehlen, P., and Puisieux, A. (2006). Metastasis: a question of life or death. Nature reviews Cancer *6*, 449-458.
Mendoza, M.C., Besson, S., and Danuser, G. (2012). Quantitative fluorescent speckle microscopy (QFSM) to measure actin dynamics. Current protocols in cytometry / editorial board, J Paul Robinson, managing editor [et al] *Chapter 2*, Unit2 18.
Mendoza, M.C., Vilela, M., Blenis, J., and Danuser, G. (submitted). ERK reinforces actin polymerization to power persistent edge protrusion during motility.
Minn, A.J., Gupta, G.P., Siegel, P.M., Bos, P.D., Shu, W., Giri, D.D., Viale, A., Olshen, A.B., Gerald, W.L., and Massague, J. (2005). Genes that mediate breast cancer metastasis to lung. Nature *436*, 518-524.
Mitchison, T.J., and Cramer, L.P. (1996). Actin-based cell motility and cell locomotion. Cell *84*, 371-379.
Mitchison, T.J., and Kirschner, M.W. (1984). Dynamic instability of microtubule growth. Nature *312*, 237-242.
Mogilner, A., and Oster, G. (1996a). Cell motility driven by actin polymerization. BIOPHYSICAL JOURNAL *71*, 3030-3045.
Mogilner, A., and Oster, G. (1996b). Cell Motility Driven by Actin Polymerization. Biophysical journal *71*, 3030-3045.
Mogilner, A., and Oster, G. (1996c). Cell motility driven by actin polymerization. Biophys J *71*, 3030-3045.
Moll, R., A, A, and A (1993). Differential loss of E-cadherin expression in infiltrating ductal and lobular breast carcinomas.
Morris, J.P.t., Wang, S.C., and Hebrok, M. (2010). KRAS, Hedgehog, Wnt and the twisted developmental biology of pancreatic ductal adenocarcinoma. Nature reviews Cancer *10*, 683-695.
Munevar, S., Wang, Y., and Dembo, M. (2001). Traction Force Microscopy of Migrating Normal and H-ras Transformed 3t3 fibroblasts. BIOPHYSICAL JOURNAL *80*, 1744–1757.
Nayal, A., Webb, D.J., Brown, C.M., Schaefer, E.M., Vicente-Manzanares, M., and Horwitz, A.R. (2006). Paxillin phosphorylation at Ser273 localizes a GIT1-PIX-PAK complex and regulates adhesion and protrusion dynamics. J Cell Biol *173*, 587-589.
Nguyen, D.X., Bos, P.D., and Massague, J. (2009). Metastasis: from dissemination to organ-specific colonization. Nature reviews Cancer *9*, 274-284.
Nobes, C.D., and Hall, A. (1995). Rho, Rac, and Cdc42 GTPases regulate the assembly of multimolecular focal complexes associated with actin stress fibers, lamellipodia, and filopodia. Cell *81*, 53-62.
Olson, M.F., and Sahai, E. (2009). The actin cytoskeleton in cancer cell motility. Clin Exp Metastasis *26*, 273-287.
Otsubo, T., Iwaya, K., Mukai, Y., Mizokami, Y., Serizawa, H., Matsuoka, T., and Mukai, K. (2004). Involvement of Arp2/3 complex in the process of colorectal carcinogenesis. Mod Pathol *17*, 461-467.
Otto, J.J., Kane, R.E., and Bryan, J. (1979). Formation of filopodia in coelomocytes: localization of fascin, a 58,000 dalton actin cross-linking protein. Cell *17*, 285-293.
Pak, C.W., Flynn, K.C., and Bamburg, J.R. (2008). Actin-binding proteins take the reins in growth cones. Nat Rev Neurosci *9*, 136-147.
Pankova, K., Rosel, D., Novotny, M., and Brabek, J. (2010). The molecular mechanisms of transition between mesenchymal and amoeboid invasiveness in tumor cells. Cellular and molecular life sciences : CMLS *67*, 63-71.

Pelham, R.J., and Wang, Y. (1997). Cell locomotion and focal adhesions are regulated by substrate flexibility. PNAS *94*, 13661-13665.
Pelosi, G., Pastorino, U., Pasini, F., Maissoneuve, P., Fraggetta, F., Iannucci, A., Sonzogni, A., De Manzoni, G., Terzi, A., Durante, E.*, et al.* (2003). Independent prognostic value of fascin immunoreactivity in stage I nonsmall cell lung cancer. Br J Cancer *88*, 537-547.
Pfaff, M., A., and A. (1999). Calpain cleavage of integrin β cytoplasmic domains1. FEBS *460*, 17-22.
Planchon, T.A., Gao, L., Milkie, D.E., Davidson, M.W., Galbraith, J.A., Galbraith, C.G., and Betzig, E. (2011). Rapid three-dimensional isotropic imaging of living cells using Bessel beam plane illumination. Nature methods *8*, 417-423.
Pollard, T., Blanchoin, L., and Mullins, R. (2000). Molecular mechanisms controlling actin filament dynamics in nonmuscle cells. Annu Rev Biophys Biomol Struct *29*, 545-576.
Pollard, T., Earnshaw, WC, Lippincott-Schwartz, J (2007). Cell Biology.
Pollard, T.B., GG (2003). Cellular motility driven by assembly and disassembly of actin filaments. Cell *112*, 453-465.
Pollard, T.D., and Borisy, G.G. (2003). Cellular motility driven by assembly and disassembly of actin filaments. Cell *112*, 453-465.
Pollard, T.D., and Weihing, R.R. (1974). Actin and myosin and cell movement. Crit Rev Biochem Mol Biol *2*, 1-65.
Ponti, A., Machacek, M., Gupton, S.L., Waterman-Storer, C.M., and Danuser, G. (2004). Two distinct actin networks drive the protrusion of migrating cells. Science *305*, 1782-1786.
Potter, D.A., A, A, and A (1998). Calpain Regulates Actin Remodeling during Cell Spreading. J Cell Biol *141*, 647–662.
Pujol, T., du Roure, O., Fermigier, M., and Heuvingh, J. (2012). Impact of branching on the elasticity of actin networks. Proc Natl Acad Sci U S A *109*, 10364-10369.
Raucher, D., and Sheetz, M.P. (2000). Cell spreading and lamellipodial extension rate is regulated by membrane tension. J Cell Biol *148*, 127-136.
Rizvi, S.A., Neidt, E.M., Cui, J., Feiger, Z., Skau, C.T., Gardel, M.L., Kozmin, S.A., and Kovar, D.R. (2009). Identification and characterization of a small molecule inhibitor of formin-mediated actin assembly. Chem Biol *16*, 1158-1168.
Rodriguez-Viciana, P., Tetsu, O., Oda, K., Okada, J., Rauen, K., and McCormick, F. (2005). Cancer targets in the Ras pathway. Cold Spring Harb Symp Quant Biol *70*, 461-467.
Rorth, P. (2003). Communication By Touch: Role of Cellular Extensions. Cell *112*, 595–598.
Rottner, K., Behrendt, B., Small, J.V., and Wehland, J. (1999). VASP dynamics during lamellipodia protrusion. Nat Cell Biol *1*, 321-322.
Saez, A., Buguin, A., Silberzan, P., and Ladoux, B. (2005). Is the mechanical activity of epithelial cells controlled by deformations or forces? Biophys J *89*, L52-54.
Samimi, H., Zaki Dizaji, M., Ghadami, M., Shahzadeh Fazeli, A., Khashayar, P., Soleimani, M., Larijani, B., and Haghpanah, V. (2013). Essential genes in thyroid cancers: focus on fascin. J Diabetes Metab Disord *12*, 32.
Sanchez-Madrid, F., and Angel del Pozo, M. (1999). Leukocyte polarization in cell migration and immune interaction. EMBO J *18*, 501-511.
Schafer, C., Faust, U., Kirchgessner, N., Merkel, R., and Hoffmann, B. (2011). The filopodium: a stable structure with highly regulated repetitive cycles of elongation and persistence depending on the actin cross-linker fascin. Cell Adh Migr *5*, 431-438.
Schoen, I., Hu, W., Klotzsch, E., and Vogel, V. (2010). Probing cellular traction forces by micropillar arrays: contribution of substrate warping to pillar deflection. Nano Lett *10*, 1823-1830.
Sedzinski, J., Biro, M., Oswald, A., Tinevez, J.Y., Salbreux, G., and Paluch, E. (2011). Polar actomyosin contractility destabilizes the position of the cytokinetic furrow. Nature *476*, 462-466.

Shah, R.B., Mehra, R., Chinnaiyan, A.M., Shen, R., Ghosh, D., and Zhou, M. (2004). Androgen-independent prostate cancer is a heterogeneous group of diseases-lessons from a rapid autopsy program. Cancer Research *64*, 9209-9216.
Shibue, T., Brooks, M.W., Inan, M.F., Reinhardt, F., and Weinberg, R.A. (2012). The outgrowth of micrometastases is enabled by the formation of filopodium-like protrusions. Cancer discovery *2*, 706-721.
Small, J.V., Monika, H., and Kurt, A. (1995). Actin Filament Organization in the Fish Keratocyte Lamellipodium.
Smilenov, L.B. (1999). Focal Adhesion Motility Revealed in Stationary Fibroblasts. Science *286*, 1172-1174.
Smith, H.W., Marra, P., and Marshall, C.J. (2008). uPAR promotes formation of the p130Cas-Crk complex to activate Rac through DOCK180. The Journal of cell biology *182*, 777-790.
Stark, G.R., Kerr, I.M., Williams, B.R., Silverman, R.H., and Schreiber, R.D. (1998). How cells respond to interferons.
Suraneni, P., Rubinstein, B., Unruh, J.R., Durnin, M., Hanein, D., and Li, R. (2012a). The Arp2/3 complex is required for lamellipodia extension and directional fibroblast cell migration. J Cell Biol *197*, 239-251.
Suraneni, P., Rubinstein, B., Unruh, J.R., Durnin, M., Hanein, D., and Li, R. (2012b). The Arp2/3 complex is required for lamellipodia extension and directional fibroblast cell migration. J Cell Biol *197*, 239-251.
Svitkina, T.M., a, a, and a (1997). Analysis of the Actin–Myosin II System in Fish Epidermal Keratocytes: Mechanism of Cell Body Translocation. J Cell Biol *139*, 397–415.
Svitkina, T.M., and Borisy, G.G. (1999). Arp23 Complex and ADFcofilin in dendritic org and treadmilling of actin filament array in lamellipodia. J Cell Biol *145*, 1009–1026.
Takenawa, T., and Suetsugu, S. (2007). The WASP-WAVE protein network: connecting the membrane to the cytoskeleton. Nature reviews Molecular cell biology *8*, 37-48.
Tan, V.Y., Lewis, S.J., Adams, J.C., and Martin, R.M. (2013). Association of fascin-1 with mortality, disease progression and metastasis in carcinomas: a systematic review and meta-analysis. BMC Med *11*, 52.
Teng, Y., Xu, S., Yue, W., Ma, L., Zhang, L., Zhao, X., Guo, Y., Zhang, C., Gu, M., and Wang, Y. (2013). Serological investigation of the clinical significance of fascin in non-small-cell lung cancer. Lung Cancer *82*, 346-352.
Theriot, J. (2000). The Polymerization Motor. Traffic *1*, 19-28.
Thiery, J.P. (2002). Epithelial-mesenchymal transitions in tumour progression. Nature reviews Cancer *2*, 442-454.
Tkachenko, E., Sabouri-Ghomi, M., Pertz, O., Kim, C., Gutierrez, E., Machacek, M., Groisman, A., Danuser, G., and Ginsberg, M.H. (2011). Protein kinase A governs a RhoA-RhoGDI protrusion-retraction pacemaker in migrating cells. Nature cell biology *13*, 660-667.
Tymchenko, N., Wallentin, J., Petronis, S., Bjursten, L.M., Kasemo, B., and Gold, J. (2007). A novel cell force sensor for quantification of traction during cell spreading and contact guidance. Biophys J *93*, 335-345.
Vettenburg, T., Dalgarno, H.I., Nylk, J., Coll-Llado, C., Ferrier, D.E., Cizmar, T., Gunn-Moore, F.J., and Dholakia, K. (2014). Light-sheet microscopy using an Airy beam. Nature methods *11*, 541-544.
Vignjevic, D., Schoumacher, M., Gavert, N., Janssen, K.P., Jih, G., Lae, M., Louvard, D., Ben-Ze'ev, A., and Robine, S. (2007). Fascin, a novel target of beta-catenin-TCF signaling, is expressed at the invasive front of human colon cancer. Cancer Res *67*, 6844-6853.
Walen, K.H., and Brown, S.W. (1962). Chromosomes in a marsupial (Potorous tridactylis). Nature *194*.
Wear, M.A., Schafer, D.A., and Cooper, J.A. (2000). Actin dynamics Assembly and disassembly of actin networks. Curr Biol *10*, R891-R895.
Weaver, A.M. (2006). Invadopodia: specialized cell structures for cancer invasion. Clin Exp Metastasis *23*, 97-105.

Wirtz, D. (2009). Particle-tracking microrheology of living cells: principles and applications. Annu Rev Biophys *38*, 301-326.
World Health Organization (2014). Cancer (http://www.who.int/mediacentre/factsheets/fs297/en/).
Wu, C., Asokan, S.B., Berginski, M.E., Haynes, E.M., Sharpless, N.E., Griffith, J.D., Gomez, S.M., and Bear, J.E. (2012). Arp2/3 is critical for lamellipodia and response to extracellular matrix cues but is dispensable for chemotaxis. Cell *148*, 973-987.
Xing, P., Li, J.G., Jin, F., Zhao, T.T., Liu, Q., Dong, H.T., and Wei, X.L. (2011). Fascin, an actin-bundling protein, promotes breast cancer progression in vitro. Cell Biochem Funct *29*, 303-310.
Xu, Y.F., Yu, S.N., Lu, Z.H., Liu, J.P., and Chen, J. (2011). Fascin promotes the motility and invasiveness of pancreatic cancer cells. World J Gastroenterol *17*, 4470-4478.
Yamaguchi, H., Wyckoff, J., and Condeelis, J. (2005). Cell migration in tumors. Curr Opin Cell Biol *17*, 559-564.
Yamashiro-Matsumura, S., and Matsumura, F. (1985). Purification and characterization of an F-actin-bundling 55-kilodalton protein from HeLa cells. The Journal of biological chemistry *260*, 5087-5097.
Yamashiro, S. (2012). Functions of Fascin in Dendritic Cells. Critical Reviews in Immunology *32*, 11-22.
Yamashiro, S., Yamakita, Y., Ono, S., and Matsumura, F. (1998). Fascin, an actin-bundling protein, induces membrane protrusions and increases cell motility of epithelial cells. Mol Biol Cell *9*, 993-1006.
Yamazaki, D., Kurisu, S., and Takenawa, T. (2005). Regulation of cancer cell motility through actin reorganization. Cancer Sci *96*, 379-386.
Yang, C., Czech, L., Gerboth, S., Kojima, S., Scita, G., and Svitkina, T. (2007). Novel roles of formin mDia2 in lamellipodia and filopodia formation in motile cells. PLoS Biol *5*, e317.
Yang, S., Huang, F.K., Huang, J., Chen, S., Jakoncic, J., Leo-Macias, A., Diaz-Avalos, R., Chen, L., Zhang, J.J., and Huang, X.Y. (2013). Molecular mechanism of fascin function in filopodial formation. The Journal of biological chemistry *288*, 274-284.
Yilmaz, M., and Christofori, G. (2010). Mechanisms of motility in metastasizing cells. Molecular cancer research : MCR *8*, 629-642.
Yoder, B.J., Tso, E., Skacel, M., Pettay, J., Tarr, S., Budd, T., Tubbs, R.R., Adams, J.C., and Hicks, D.G. (2005). The expression of fascin, an actin-bundling motility protein, correlates with hormone receptor-negative breast cancer and a more aggressive clinical course. Clin Cancer Res *11*, 186-192.
Yokotsuka, M., Iwaya, K., Saito, T., Pandiella, A., Tsuboi, R., Kohno, N., Matsubara, O., and Mukai, K. (2011). Overexpression of HER2 signaling to WAVE2-Arp2/3 complex activates MMP-independent migration in breast cancer. Breast Cancer Res Treat *126*, 311-318.
Zaoui, K., Honore, S., Isnardon, D., Braguer, D., and Badache, A. (2008). Memo-RhoA-mDia1 signaling controls microtubules, the actin network, and adhesion site formation in migrating cells. J Cell Biol *183*, 401-408.
Zeng, L., Si, X., Yu, W.P., Le, H.T., Ng, K.P., Teng, R.M., Ryan, K., Wang, D.Z., Ponniah, S., and Pallen, C.J. (2003). PTP alpha regulates integrin-stimulated FAK autophosphorylation and cytoskeletal rearrangement in cell spreading and migration. J Cell Biol *160*, 137-146.
Zhang, F.R., Tao, L.H., Shen, Z.Y., Lv, Z., Xu, L.Y., and Li, E.M. (2008). Fascin expression in human embryonic, fetal, and normal adult tissue. J Histochem Cytochem *56*, 193-199.
Zheng, H., Zheng, Y., Li, X., and Takahashi, H. (2008). Arp23 overexpression contributed to pathogenesis, growth and invasion of gastric carcinoma. Anticancer Research *28*, 2225-2232.
Zigeuner, R., Droschl, N., Tauber, V., Rehak, P., and Langner, C. (2006). Biologic significance of fascin expression in clear cell renal cell carcinoma: systematic analysis of primary and metastatic tumor tissues using a tissue microarray technique. Urology *68*, 518-522.

Appendix 1: Supplementary Figures and Figure Legends

Supplementary Figure 1

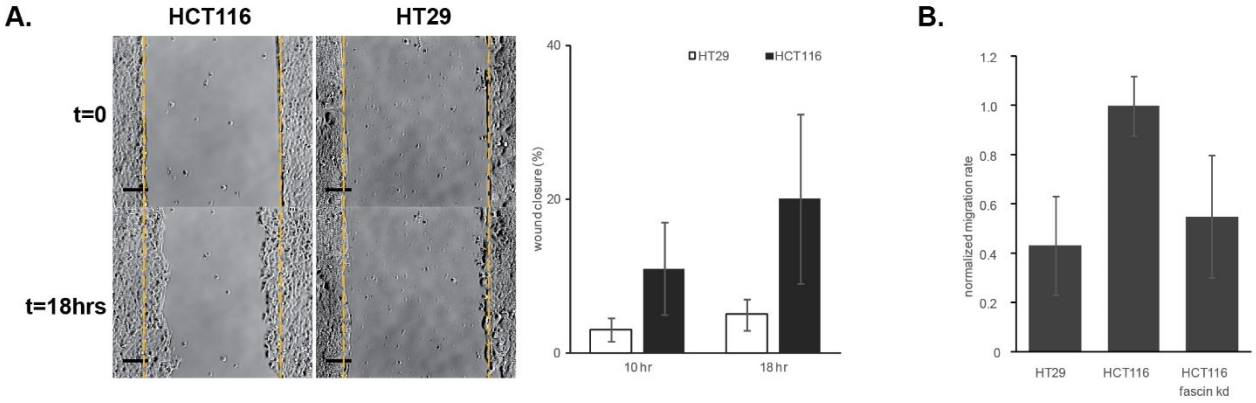

Supplementary Figure 1. Migration in HCT116 and HT29 colon cancer cells (A) Left, representative results of wound healing response in HCT116 (left column) and HT 29 (right column) cells at 0 and 18 hours. Scale bar: 50 μm. Right, quantification of percentage wound closure at 10 and 15 hours. Error bars: SEM from 12 positions for each condition (3 independent experiments). (B) Results of transwell migration assay for HT29, HCT116, and HCT116 fascin KD cells. Error bars: SEM from 6 wells for each condition (3 independent experiments).

Supplementary Figure 2

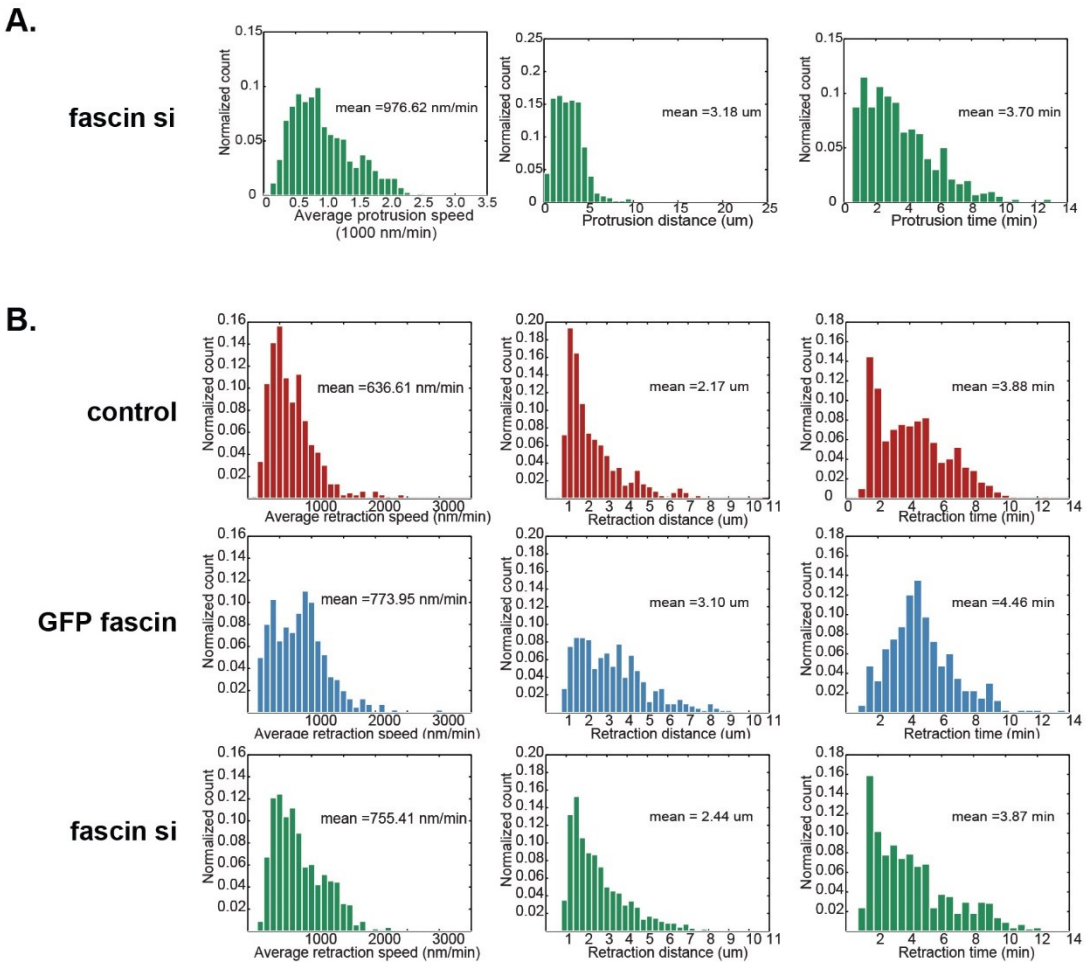

Supplementary Figure 2. (A) Histograms of average protrusion speed, protrusion distance, and protrusion time in fascin si (7 cells, 1339 time series) cells. (B) Histograms of average retraction speed (left column), retraction distance (middle column), or retraction time (right column) in control (top row, 6 cells, 1218 time series), GFP fascin (middle row, 6 cells, 1299 time series), and fascin si (bottom row, 7 cells, 1339 time series) cells. All conditions were repeated in at least 3 independent experiments.

Appendix 2:
Mechanosensitivity in the Cooperative Dynamics of Actin Nucleators During Epithelial Cell Protrusion

Summary

Many cellular functions rely on the integration of biochemical pathways with mechanical force. The dissection of mechanosensitive pathways has remained a challenge in biological investigation due to the interplay of multifactorial and partially redundant processes in space and time[1]. One example is cell migration, which is driven by actin polymerization in the lamellipodium[2,3]. Current models focus on the Arp2/3 complex as the initiator of lamellipodial actin filament assembly[4]. However, other nucleators including formins have been reported as contributors to lamellipodial network formation[5-7]. Although the biochemical modes of action of these molecules are well understood, it has remained largely unknown in what way they are coordinated. Here, we establish that the activation of actin nucleators is mechano-responsive. We developed a statistical approach based on local image sampling and registration that exploits constitutive protrusion/retraction fluctuations to identify the differential recruitment of partially redundant actin nucleators/modulators. The formin mDia1 is recruited to the leading edge before protrusion onset along with components of nascent adhesions. Together these processes initiate cell edge advancement by promoting linear growth of the lamellipodial network. In contrast, Arp2/3, VASP, cofilin and the formin mDia2 are sequentially recruited only after protrusion initiation, where they promote sustained exponential network growth. Temporal correlation analysis of mDia1 and Arp2/3 in conjunction with pharmacological inhibition of formin supports the dependence of Arp2/3 recruitment on the initiation process. Perturbing the homeostasis of membrane tension revealed that Arp2/3 recruitment is

mechano-responsive. Together these experiments suggest that migrating cells adjust the molecular strategy for actin-based protrusion in response to mechanical cues on a ten-second time scale. Our data are consistent with an Initiation-Reinforcement model where mDia1-activation starts new protrusions, while Arp2/3, mDia2, and other modulators function to upregulate actin polymerization to sustain edge advancement against increasing cell membrane tension.

Contribution

My major contribution to this paper is the development of a working protocol for the traction force microscopy (TFM) experiments and the subsequent of doing of the experiments. The propulsive and contractile forces generated by cells are coupled to the substrate via cell-matrix adhesions, and this force that an adherent cell exerts on the underlying substrate is known as traction force. TFM allows one to measure such force by tracking the deformations on a soft substrate resulting from the traction force of a cell when it migrates. The difficulty in setting up this experiment was that the imaging chamber needed to be sealed in order to protect cells from photodamage but allow for subsequent trypsin treatment. I achieved the two goals by developing a perfusion system that included a dish cover fitted with an inlet and an outlet tubing. The dish was then sealed with valap and filled with imaging media using a syringe. The ability to perform such TFM experiments was critical in observing the tight coordination of traction force, adhesion formation, and edge motion at length and time scale of single microns and seconds. Such observations then led to the hypothesis that spatiotemporal variation in edge motion and thus in traction force is directly coupled to variation in the rates of lamellipodial actin network assembly.

In addition, I performed Western blots to check expression levels of various actin nucleators.

Mechanosensitivity in the Cooperative Dynamics of Actin Nucleators During Epithelial Cell Protrusion

Kwonmoo Lee[a,c], Hunter L. Elliott[a], Youbean Oak[a], Chih-Te Zee[b], Alex Groisman[b], Jessica D. Tytell[a], Gaudenz Danuser[a,d]

[a]Department of Cell Biology, Harvard Medical School, Boston, Massachusetts, 02115, USA.

[b]Department of Physics, University of California San Diego, La Jolla, California, 92093, USA.

[c]Present Address: Department of Biomedical Engineering, Worcester Polytechnic Institute, Massachusetts, 01609, USA

[d]Present Address: Department of Cell Biology, University of Texas Southwestern Medical Center, Texas, 75235, USA

Classification: Biological Science, Biophysics and Computational Biology

Corresponding Authors: Gaudenz Danuser, Department of Cell Biology, University of Texas Southwestern Medical Center, Texas, 75235, USA, Telephone: (214) 648-3835, Email: Gaudenz.Danuser@UTSouthwestern.edu; Kwonmoo Lee, Department of Biomedical Engineering, Worcester Polytechnic Institute, Massachusetts, 01609, Telephone: (508) 831-4904, Email: klee@wpi.edu

Key Words: Cell Migration, Cytoskeleton, Computational Image Analysis, Mechanobiology

Abstract:

Dissection of cellular processes that are dictated by high nonlinearity and redundancy between multiple pathways has remained a challenge. In particular, genetic and molecular perturbations induce complex process responses that are nearly impossible to interpret in terms of the function of the targeted component in the unperturbed pathway. One example is the protrusion of migrating cells, driven by actin polymerization in the lamellipodium. Current models focus on the Arp2/3 complex as the initiator of lamellipodial actin filament assembly. However, other nucleators, including formins, have been reported as additional contributors The modes of their coordination has remained largely unknown. Here, we introduce a statistical approach based on local image sampling and registration that exploits constitutive protrusion/retraction fluctuations in the unperturbed cell to identify the differential recruitment of actin nucleators/modulators. The formin mDia1 is recruited to the leading edge before protrusion onset along with components of nascent adhesions. This initiates cell edge advancement by linear growth of the lamellipodial network. Arp2/3, VASP, cofilin and the formin mDia2 are recruited only after protrusion initiation, where they promote sustained exponential network growth. Changes in membrane tension revealed that Arp2/3 recruitment is mechano-responsive. Together these experiments suggest that migrating cells adjust the molecular strategy for actin-based protrusion in response to mechanical cues on a ten-second time scale. Our data are consistent with an Initiation-Reinforcement model where mDia1-activation starts new protrusions, while Arp2/3, mDia2, and other modulators function to upregulate actin polymerization to sustain edge advancement against increasing cell membrane tension.

Significance Statement:

The non-invasive quantitative imaging approach presented here allows us to probe a highly-redundant system of actin nucleation pathways, where experimental intervention primarily leads to a 'redistribution of workload between redundant pathways', i.e. system adaptation. Using this method we were able to define a hierarchy of nucleator recruitment and we discovered that the actin nucleation pathways are highly mechanosensitive to rapid and local fluctuation in membrane tension.

Introduction

Many cellular functions rely on the integration of biochemical pathways with mechanical force. The study of the effects of forces on the molecular regulation of cell function is complicated because of the intrinsic non-linearity and the redundancy (Kafri et al., 2009) of mechano-responsive pathways. In this scenario, genetic and molecular perturbation approaches are limited in their ability to probe the system as they tend to lead to system adaptations that obscure the bona fide function of the targeted component under unperturbed conditions. A classic example of a mechano-responsive process with non-linearity and redundancy is actin-based cell protrusion (Lauffenburger and Horwitz, 1996b; Ponti et al., 2004). This machinery needs constant adaptation to ever-changing mechanical (and chemical) inputs. Current models focus on the Arp2/3 complex as the initiator of lamellipodial actin filament assembly (Pollard and Borisy, 2003). Increasing evidence suggests, however, that even under global deregulation of Arp2/3 activity, cells still protrude efficiently (Suraneni et al., 2012a; Wu et al., 2012). These data show that filament growth mediated by other factors such as the members of the formin family of actin nucleators (Block et al., 2012; Yang et al., 2007; Zaoui et al., 2008) or actin modulators like VASP or cofilin (Bear et al., 2002; Ghosh et al., 2004; Lacayo et al., 2007; Rottner et al., 1999) alone are competent to drive cell protrusion. Whether there is any functionally-critical coordination among the nucleator/modulator activities has never been addressed. Because of functional overlap and potential feedback among them, answers to this question require an analysis of nucleator dynamics in an unperturbed system. An analysis of multiple actin modulators has recently been achieved by *in vitro* reconstitution of filopodia-like structures, where the stereotypical growth of actin filament bundles revealed temporal coordination and cooperation between Arp2/3 and mDia formins (Lee et al., 2010). These reconstitution systems, however, do not readily show how mechanical forces

may influence the mutual dynamics. The goal of the present study was to perform this type of analysis *in situ* for more complex mechanochemical processes such as the protrusion of an entire cell edge.

Results

Traction force dynamics at the leading edge of migrating PtK1 epithelial cells. Our analyses relied on the spontaneous protrusion-retraction cycles observed in epithelial cells undergoing a wound healing response (Fig. 8A). We used automatic tracking of the leading edges of PtK1 epithelial cells and identified the state of protrusion and retraction locally in 500 nm-long sectors along the leading edge (Elliott, 2012). For each sector, we determined the protrusion or retraction velocity and the time since protrusion/retraction onset (Fig. 8B, C and Supplementary Movie 1 and 2). Fast and slow protruding sectors, or protruding and retracting sectors alternate over distances as short as 2 – 3 μm. Accordingly, we expected that the regulation of actin assembly dynamics, which controls the state of edge motion, would vary on similar time and length scales.

To investigate the functional integration of multiple actin nucleators/modulators with the generation of mechanical force and edge motion, we recorded time series of molecular/cellular events such as the recruitment of a particular actin nucleator and spatiotemporal fluctuations in the traction force levels in probing windows of about 1 μm^2, which tracked the cell edge (Fig. 8D; Supplementary Movie 3). The size of the windows was chosen to be several-fold smaller than the 2 – 3 μm length scale of protrusions, yet large enough to reduce by averaging the pixel-by-pixel noise of molecular events. Because of the intrinsic variation of molecular events within an area of ~1 μm^2, each time series provided one instantiation of a random process that relates these events

to cell edge motion. Therefore, to answer questions like 'when does a particular event happen relative to the onset of a protrusion, or relative to another event', it was necessary to average over many time-series. To this end, we brought the time series into register using one of three edge motion events as a temporal fiduciary: retraction onset, protrusion onset, and instance of maximal protrusion velocity (Fig. 8E-G). Subsequently, we averaged the intensity time series, first over all windows within a cell, and then across multiple cells. Of note, the accuracy of these final cell-population time series is highest about the event used for alignment and decreases with time before and after the event due to molecular and temporal variation between individual protrusion segments.

To convert actin assembly into edge protrusion, propulsive forces generated by growing filaments must be balanced by adhesions that generate traction on the substrate. Therefore, the coordinated action of actin nucleators/modulators is predicted to produce coupled variations in traction force and adhesion assembly. To test this, we first applied our local sampling and registration approach to traction force microscopy (Fig. 8H, Supplementary Movie 4) and investigated how traction forces are coordinated with edge motion during protrusion-retraction cycles. We also monitored the assembly of adhesions by recruitment of HaloTag-TMR-labeled paxillin (Supplementary Movie 5) as a canonical marker for nascent adhesion formation (Nayal et al., 2006). Both traction forces and paxillin intensity were quantified in a 'cell frame of reference', where probing windows tracked the motion of the leading edge (Fig. 8I, Supplementary Movie 3 and 6 (yellow windows)), and in a 'laboratory frame of reference', where probing windows were dynamically placed at the locations of protrusion onset but then left stationary to monitor the force evolution and protein recruitment at newly forming immobilized adhesions (Fig. 8J and Supplementary Movie 6 (red windows)). Traction force levels at the cell edge had a basal level of

~350Pa and fluctuated ~50Pa about this value (Fig. 8K – M). This is consistent with previous traction force measurements in the same model cell, which suggested that overall the cell cortex is pre-stressed by actomyosin contractility with superimposed smaller force variations that are associated with the dynamics of the actin protrusion machinery(Gardel et al., 2008). Specifically, in the cell frame of reference, traction forces at the leading edge started to increase at retraction onset (Fig. 8K) until they dropped 25 sec after protrusion onset (Fig. 8L). They displayed a significant dip when registered with respect to maximal protrusion velocity (Fig. 8M), suggesting that adhesion sites are translocated away from the advancing edge. These events were paralleled by paxilin intensity (Fig. S1A-C). In the laboratory frame of reference, traction forces (Fig. 8N and O) and paxillin intensity (Fig. S1D and E) showed sustained increases as edge protrusion proceeded. From this data, we concluded that nascent adhesion formation is initiated before protrusion onset at the retracting edge and then immobilized at protrusion initiation sites to counteract the propulsive forces generated at the advancing edge. Importantly, nascent adhesion formation happens only once at the onset of the protrusion cycle. The actin filament network formed after protrusion onset remains without substrate engagement until the onset of the next protrusion segment. Further support for this model was provided by analysis of the retrograde flow of actin filaments(Ponti et al., 2004) (Supplementary Note 1).

Next, we investigated how traction forces are temporally coordinated with edge motions. We first selected in the cell frame of reference the time series during retraction and calculated Pearson's correlation coefficient between edge velocity and traction force as a function of the time lag between the time series. We found a significant positive correlation at -10 seconds time lag (Fig. 8P) indicating that the retraction slows down 10 seconds after traction force begins to increase. We performed the same correlation analysis for the protrusion phase in the laboratory frame of

reference (where the traction force develops). Using the time series from protrusion onset to 50 seconds before maximal protrusion velocity, no significant correlation between edge velocity and traction force was observed (Fig. 8Q). However, when the time series were extended to 50 seconds after maximal protrusion velocity occurs, a significant correlation maximum occurred at 40 seconds time lag (Fig. 8R), meaning that traction force increases 40 seconds after the edge velocity increases. Thus, while the initial protrusion phase is nearly free of mechanical load on the growing actin filaments and coupled adhesions, beyond a critical point further edge advancement expands the plasma membrane under increasing tension. The adhesion marker paxillin displayed similar coordination with edge motion (Fig. S1K-M). Taken together, our local image sampling and registration of traction forces and adhesion recruitment indicated a tight coordination of traction force, adhesion formation, and edge motion at length and time scale of single microns and seconds.

Recruitment of actin nucleators to lamellipodium. We hypothesized that spatiotemporal variation in edge motion and thus in traction force is directly coupled to variation in the rates of lamellipodial actin network assembly. To test this, we micro-injected trace amounts of Alexa 568 labeled actin into PtK1 cells and monitored by live cell imaging fluctuations in fluorescence intensity as a proxy for actin recruitment to the lamellipodium (Supplementary Movie 7). As expected, the fluorescence decreased/increased after retraction/protrusion onset (Fig. 9A and B). Importantly, these dynamics were opposite to those observed for a diffuse fluorescent tag (HaloTag-TMR) (Supplementary Note 2, Fig. S2A-C, Supplementary Movie 8), indicating that the fluorescence signal from low amounts of Alexa 568 labeled actin predominantly reports the fraction of actin monomers incorporated in the filament network. Registration of the signal relative to maximal protrusion velocity displayed a sharp peak 10 sec after the reference event (Fig. 9C), which is consistent with previous quantitative Fluorescent Speckle Microscopy analyses showing

that the rate of actin assembly peaks after the time point of fastest protrusion (Gardel et al., 2008). Next, we asked whether the temporal variation in actin filament assembly is related to temporal variations in recruitment and activation of actin nucleators/modulators. For this purpose we expressed HaloTag fusions to nucleators/modulator proteins and labeled them with TMR (Tetramethylrhodamine) ligands. First applied to the Arp3 component of the Arp2/3 complex(Pollard and Borisy, 2003), we found an almost identical recruitment pattern to actin (Fig. 9D-F, Supplementary Movie 9) with the exception that the actin signal increased significantly just before protrusion onset, while the HaloTag-TMR-Arp3 signal began to increase only 10 – 20 s after protrusion onset (cf. Fig. S2D vs. Fig. S2E). This suggests that in spontaneous edge protrusions during epithelial wound healing Arp2/3 is not the initiator of lamellipodial actin filament assembly.

The involvement of Arp2/3 as a nucleator of lamellipodial actin filament assembly is well-established in PtK1 cells, but the roles of other nucleators such as formin family members have not been addressed systematically. Previous work suggested that formins were absent from the lamellipodium (Gupton et al., 2007). However, by reverse transcription PCR, Western blot (Fig. S3A and B), and immunofluorescence imaging (Fig. 10G-I) we found both mDia1 and mDia2 expressed and localized to the leading edge, along with Arp2/3 (Fig. S3C and D). Therefore, we investigated the recruitment dynamics of mDia1 and mDia2 (Supplementary Movies 10, 11). In contrast to Arp2/3, the fluorescence of HaloTag-TMR labeled mDia1 decreased after retraction onset but then consistently increased after 50 sec (Fig. 9J) and plateaued before protrusion onset (Fig. 9K). Hence mDia1 arrives at the leading edge much earlier than Arp2/3. Moreover, mDia1 recruitment underwent a transient dip ~15 sec after maximal protrusion velocity (Fig. 9L), when Arp2/3 recruitment exhibited a sharp peak (Fig. 9I), suggesting a hand-over from mDia1-based to

Arp2/3-based actin nucleation during fast protrusion (Fig. S4, Supplementary Note 3). Similar to mDia1, mDia2 fluorescence decreased after retraction onset (Fig. 9M), but unlike mDia1, it significantly increased only 30 sec after protrusion onset (Fig. 9N) with a distinct peak (rather than a dip) 40 sec after maximal protrusion velocity (Fig. 9O). Hence mDia2 is recruited to the lamellipodium 30 sec after Arp2/3, similar to *in vitro* measurements (Lee et al., 2010) and consistent with the idea that formins can elongate Arp2/3-nucleated actin filaments(Block et al., 2012; Lee et al., 2010; Yang et al., 2007). VASP and cofilin dynamics were similar to Arp2/3 (Fig. S5, Supplementary Movies 12, 13), with the exception that cofilin recruitment peaked 30 sec after maximal protrusion velocity, i.e. 20 sec later than actin, Arp2/3 and VASP (Fig. S5F). Importantly, none of the HaloTag-TMR labeled proteins exhibited the behaviors of diffuse HaloTag-TMR, implying that the level of labeling was low enough to specifically highlight the fraction of protein immobilized by association with the actin filament network. Taken together, our analyses revealed a differential recruitment of actin nucleators/modulators during distinct phases of the protrusion-retraction cycle. Of all the measured factors, mDia1 was the only one to arrive at the leading edge before protrusion. All other polymerization promoters followed after protrusion onset in the order Arp2/3, VASP, cofilin, and mDia2.

Roles of mDia1 in membrane protrusions of migrating epithelial cells. To further investigate functional significance of mDia1 as an initiator of lamellipodial network assembly and cell protrusion, we performed dual-color live cell imaging of EGFP- mDia1 and SNAP-tag-TMR-actin. By exploiting the spatiotemporal variation of the fluorescence signal associated with constitutive protrusion and retraction activity, we established statistical relationships between the two recruitment processes. In agreement with the recruitment sequence derived from single channel imaging of actin and actin nucleators, the dynamics of simultaneously imaged mDia1 and actin

recruitment exhibited close similarity prior to protrusion onset, but they diverged afterwards (Fig. S6A-C). Correlation analysis between EGFP-mDia1 and SNAP-tag-TMR-actin time series aligned relative to protrusion onset showed significant correlation values in the upper triangle of the pairwise correlation matrix (Fig. 10A, Fig. S6D; Methods), indicating that mDia1 systematically preceded actin polymerization and suggesting that mDia1 drives actin assembly before protrusion onset. To test how the coupling of mDia1 and actin recruitment prior to protrusion influences lamellipodial and edge motion dynamics during protrusion, we correlated the mean EGFP-mDia1 intensity in a probing window during retraction with the mean SNAP-tag-TMR-actin intensity in the same window during protrusion. This analysis revealed that the level of mDia1 recruitment during retraction has a significant correlation (0.27, $p= 2.3 \times 10^{-20}$) with the amount of actin polymerization during protrusion (Fig. 10B). For comparison, we did not find significant correlation between mDia1 during protrusion and actin during retraction (0.02, $p= 0.5$). On the other hand, we also found a significant correlation between actin recruitment during retraction and actin recruitment during protrusion (Fig. 10C). Together, these analyses suggest that mDia1-mediated actin assembly prior to protrusion determines the amount of actin assembly during protrusion.

The recruitment sequence of actin nucleators derived from single channel imaging also indicated that actin polymerization after protrusion onset is dominated by Arp2/3. Thus, our correlation analyses between mDia1 and actin recruitment implies a connection between mDia1-mediated actin assembly prior to and Arp2/3 activation after protrusion onset. To test this, we performed dual-color imaging of EGFP-mDia1 and Arp3-HaloTag-TMR, and correlation analysis between the mDia1 mean intensity during retraction and the Arp2/3 mean intensity during protrusion (Fig. 10D). Indeed, we found a significant correlation between the two variables (0.20,

$p = 3.5 \times 10^{-14}$) compared to a much weaker correlation between mDia1 during protrusion and Arp2/3 during retraction (0.05, $p = 0.04$).

Our statistical analyses thus far suggest that early recruitment of mDia1 may nucleate the growth of linear actin structures that are anchored to the substrate by nascent adhesions before protrusion starts and that this process plays an important role in coordinating the recruitment of Arp2/3, which enhances filament growth after protrusion onset. To confirm the coordination between mDia1 and Arp2/3 directly, we treated PtK1 cells with 20μM SMIFH2, a chemical inhibitor of formin FH2 domains (Rizvi et al., 2009). Formin-inhibited cells had less protrusive activity than cells under control conditions (Fig. 10E and F), with a much tighter distribution of net distances travelled over the course of an entire movie (Fig. S7A). This suggests that formin plays a role in controlling the distance range of protrusion-retraction cycles. To investigate this further we identified protrusion and retraction segments for each probing window (Fig. S7B) and calculated their duration and average velocity. The marginal distributions of the two parameters in control and formin-inhibited cells showed only weakly significant differences (Fig. S7C and D). However, the joint distribution revealed that with formin-inhibition fast protrusion segments lasted for only a short time, while long-lasting protrusion segments tended to be slow. In control cells the two parameters were less correlated (Fig. 10G). As a result, the distance traveled over one protrusion segment was significantly reduced by formin inhibition (Fig. 10H and Fig. S7E). Formin-inhibition also constrained the distance edge windows traveled over retraction segments (Fig. S7F-I). This explains why, when integrated over the course of an entire movie the leading edge of formin-inhibited epithelial cells traveled the same net distance as control cells.

To confirm the predicted role of mDia1 in modulating Arp2/3 recruitment we compared Arp2/3 dynamics in cells without and with SMIFH2 treatment. Because the expression levels of

Arp2/3-HaloTag-TMR varied between cells we normalized the Arp2/3 intensity in the lamellipodium to the Arp2/3 intensity in the region 1.5 – 2 μm from the cell edge. Under formin inhibition, Arp2/3 levels did not significantly increase after protrusion onset and, compared to control cells, they exhibited only minor fluctuations after the time points of retraction onset and maximal protrusion velocity (Fig. 10I and J; Fig. S8A). Consistent with the dynamic analysis, the overall levels of Arp2/3 in the lamellipodium at maximal protrusion velocity were substantially reduced with SMIFH2 treatment, but they remained unchanged over the entire lamella region located behind the lamellipodium (>2 μm from the cell edge) (Fig. 11K). Similar analysis of paxillin recruitment demonstrated a critical role of mDia1 in adhesion formation (Supplementary Note 4, Fig. 10L, Fig. S8B).

Mechanosensitivity of Arp2/3 dynamics during cell protrusion. Combining our observations of traction force fluctuations with the coordination of actin nucleators/modulators led to the hypothesis that the Arp2/3 recruitment after protrusion onset could be controlled by the increasing force levels in nascent adhesions. Since these forces balance propulsive forces by actin polymerization at the cell edge, this would provide a mechanism for a mechano-responsive positive feedback, in which initial protrusion mediated by mDia1-driven filament assembly promotes the recruitment of Arp2/3 (and other nucleators) in order to increase the rate of actin-based propulsion against increasing membrane tension and further reinforcement of Arp2/3 recruitment. Accordingly, the rate of Arp2/3 recruitment is predicted to depend on the rate of plasma membrane tension increase. To test this prediction, we altered the membrane tension levels and used our statistical image analysis to determine how the recruitment of Arp2/3 and mDia1 was affected. Two approaches have been established to manipulate membrane tension: active methods, which apply pulling force on the membrane (Houk et al., 2012; Raucher and Sheetz, 2000) and

passive pharmacological methods (Gauthier et al., 2011; Raucher and Sheetz, 2000; Sedzinski et al., 2011), which alter the structure of the membrane. Both techniques result in equilibration of tension state over short time scales (Houk et al., 2012). To enable high resolution imaging in a closed chamber while manipulating tension level, we chose to perturb tension homeostasis by established passive methods that apply 400 μM Deoxycholate (Raucher and Sheetz, 2000) or 1 μg/ml Concanavalin A (Con A) (Sedzinski et al., 2011) to globally reduce or increase membrane tension. We validate the effect of perturbing membrane tension on the overall force levels by traction force measurements after Deoxycholate treatment. The experiment demonstrated that membrane tension is required for the correlation between edge motion and traction force variation at the leading edge (Supplementary Note 5, Fig. S9A). In previous studies variation in membrane tension was associated with increased (low tension) or decreased (high tension) efficiency of the load-dependent polymerization ratchet (Gauthier et al., 2011; Mogilner and Oster, 1996c; Raucher and Sheetz, 2000). Consistent with this inference, we found that reduced membrane tension using Deoxycholate significantly increased protrusion segmental velocity (Fig. 11A). However, increased membrane tension under Con A treatment also increased protrusion segmental velocity (Fig. 11B). This would support a tension-induced positive feedback in the activation of actin nucleators/modulators that compensates and even overcomes the load-dependent efficiency drop of the polymerization ratchet (Mogilner and Oster, 1996c). To test this model we investigated the changes in actin nucleator recruitment dynamics elicited by changes in membrane tension. Reducing membrane tension abolished the recruitment peak of Arp2/3 ~10 s after maximal protrusion velocity (Fig. 11C). Together with the traction force measurements (Fig. S9A), this suggests that during a protrusion cycle the membrane tension and the traction force at the leading edge increase, which is responsible for Arp2/3 activation during reinforcement of cell protrusion.

Increasing membrane tension did not alter the timing of the Arp2/3 peak after maximal protrusion velocity, but it significantly raised the rate of Arp2/3 recruitment prior to this time point (Fig. 11D). Consistent with these recruitment patterns, the average edge velocity before maximal protrusion velocity was not greatly changed by lowering tension (Fig. 11E), but was increased significantly by raising tension (Fig. 11F). We also tested the mechanosensitivity of mDia1 formin. In contrast to Arp2/3, we did not find significant differences of mDia1 dynamics between control conditions and conditions of altered membrane tension (Fig. 11G-H). Finally, we repeated the same analysis for the Rho family GTPase Rac1, which is an upstream activator of the Arp2/3 complex (Machesky and Insall, 1998) (Supplementary Note 6, Fig. S9B-C). The recruitment of Rac1 to the region of nascent adhesions at the leading edge also depended on membrane tension, suggesting that mechano-sensitivity in Rac1 signaling may mediate the transient activation of Arp2/3.

Discussion

Taken together, our data indicate that Arp2/3 recruitment, but not mDia1 recruitment, is controlled, at least in part, by the level of membrane tension. This mechanism is elicited either globally by manipulations of tension homeostasis, or dynamically during spontaneous protrusion-retraction cycles where membrane tension changes transiently with the level of edge advancement. Hence, these results show a rapid adaptation of the actin assembly machinery to variable force levels. We propose that this mechanism is the core component of an Initiation-Reinforcement cycle of actin filament assembly that drives persistent cell protrusion (Fig. 11I): mDia1 is first recruited to the plasma membrane and activated during cell edge retraction to nucleate linear actin structures. These early actin assembly events generate a filament scaffold for the recruitment of molecular components into nascent adhesions (Choi et al., 2008b). At this point it is possible that other

members of the formin family may be involved in this process (Iskratsch et al., 2013), with the exception of mDia2 that has been characterized as a late factor. At protrusion onset, adhesions are spatially immobilized and Arp2/3 recruitment is activated. Arp2/3 binds to early -nucleated mother filaments and promotes the exponential growth of a lamellipodial network in dendritic branches (Initiation). This accelerates membrane protrusion. As protrusion proceeds increasing membrane tension slows down edge advancement while activating the mechano-responsive Arp2/3 recruitment to sustain actin filament assembly (Reinforcement) (Gardel et al., 2008). To corroborate heightened polymerization during Reinforcement, additional factors like VASP and mDia2, which compete with polymerization-blocking capping proteins for free filament ends, are recruited after the time point of maximal protrusion velocity. The transition from Initiation to Reinforcement happens over 10 seconds and depends on the mechanical conditions. While the molecular details of this switch remain to be determined, previous data suggest that both the decrease in RhoA activity and the increase in Rac1/Cdc42 activity during a protrusion/retraction cycle are coupled to adhesion-substrate engagement (Machacek et al., 2009; Tkachenko et al., 2011) and force transduction (Tkachenko et al., 2011). Thus, we expect that the protein components and the timing of the Initiation and Reinforcement phases vary between different modes of cell migration and between different microenvironments. The here presented statistical framework for the analysis of dynamic image events will greatly accelerate determination of functional links between extracellular and intracellular mechananochemical guidance cues and the fine coordination of several redundant actin assembly pathways required for efficient cell protrusion during directed migration.

Materials and Methods

Live cell imaging PtK1 cells were imaged at 5 s interval for 1000 s using a 60x, 1.4 NA Plan Apochromat objective with 1.5x optovar, (for traction force microscopy no optovar was used) for spinning disk confocal microscopy and using 100x, 1.49 NA Plan Apochromat objective for TIRF microscopy.

mDia formin inhibition PtK1 cells were incubated with 20 μM SMIFH2 (Sigma-Aldrich) for 1 hour. For analysis of protrusion dynamics, cells were stained using CellMask Orange after incubation with SMIFH2. For HaloTag fusion proteins, HaloTag was labeled with TMR ligands after incubation with SMIFH2.

Membrane tension perturbation PtK1 cells were incubated with either 400 μM Dexoycholate (Sigma-Aldrich) for 30 minutes (decreasing membrane tension) or 1 μg/ml Concanavalin A (Invitrogen) for 10 minutes (increasing membrane tension) and washed by the media before imaging. HaloTag labeling with TMR ligands was done before membrane tension perturbation.

Traction force microscopy Preparation of soft substrates with far-red fluorescent beads for traction force microscopy is described elsewhere (Gutierrez et al., 2011). Cell traction forces were calculated by comparing images of tracer particles with and without cells on the substrate using Fourier transform traction cytometry method (Butler et al., 2002).

Image Analysis Cell edges were segmented by intensity thresholding, cell edge displacements were tracked, and probing windows were generated with a window size of 500 nm by 500 nm for fluorescence intensity/actin flow analysis and 1 μm by 1 μm for traction force analysis (Elliott, 2012). Protrusion and retraction segments were identified on a per-window basis using a filtered edge displacement time series (Fig. S2A). Time-series of normalized fluorescence intensities,

traction forces, actin retrograde flow sampled in individual windows were aligned relative to retraction/protrusion onsets and the instance of maximal protrusion velocity and averaged over all windows from multiple cells. The 95% confidence intervals about the average series were obtained by bootstrap resampling of the individual time series. All procedures are detailed in Supplementary Methods.

References

1. Kafri R, Springer M, & Pilpel Y (2009) Genetic redundancy: new tricks for old genes. (Translated from eng) *Cell* 136(3):389-392 (in eng).
2. Lauffenburger DA & Horwitz AF (1996) Cell migration: a physically integrated molecular process. (Translated from eng) *Cell* 84(3):359-369 (in eng).
3. Ponti A, Machacek M, Gupton SL, Waterman-Storer CM, & Danuser G (2004) Two distinct actin networks drive the protrusion of migrating cells. (Translated from eng) *Science* 305(5691):1782-1786 (in eng).
4. Pollard TD & Borisy GG (2003) Cellular motility driven by assembly and disassembly of actin filaments. (Translated from eng) *Cell* 112(4):453-465 (in eng).
5. Wu C*, et al.* (2012) Arp2/3 is critical for lamellipodia and response to extracellular matrix cues but is dispensable for chemotaxis. (Translated from eng) *Cell* 148(5):973-987 (in eng).
6. Suraneni P*, et al.* (2012) The Arp2/3 complex is required for lamellipodia extension and directional fibroblast cell migration. (Translated from eng) *J Cell Biol* 197(2):239-251 (in eng).
7. Zaoui K, Honore S, Isnardon D, Braguer D, & Badache A (2008) Memo-RhoA-mDia1 signaling controls microtubules, the actin network, and adhesion site formation in migrating cells. (Translated from eng) *J Cell Biol* 183(3):401-408 (in eng).
8. Yang C*, et al.* (2007) Novel roles of formin mDia2 in lamellipodia and filopodia formation in motile cells. (Translated from eng) *PLoS Biol* 5(11):e317 (in eng).
9. Block J*, et al.* (2012) FMNL2 drives actin-based protrusion and migration downstream of Cdc42. (Translated from eng) *Curr Biol* 22(11):1005-1012 (in eng).
10. Lacayo CI*, et al.* (2007) Emergence of large-scale cell morphology and movement from local actin filament growth dynamics. (Translated from eng) *PLoS Biol* 5(9):e233 (in eng).
11. Ghosh M*, et al.* (2004) Cofilin promotes actin polymerization and defines the direction of cell motility. (Translated from eng) *Science* 304(5671):743-746 (in eng).
12. Bear JE*, et al.* (2002) Antagonism between Ena/VASP proteins and actin filament capping regulates fibroblast motility. (Translated from eng) *Cell* 109(4):509-521 (in eng).

13. Rottner K, Behrendt B, Small JV, & Wehland J (1999) VASP dynamics during lamellipodia protrusion. (Translated from eng) *Nat Cell Biol* 1(5):321-322 (in eng).
14. Lee K, Gallop JL, Rambani K, & Kirschner MW (2010) Self-assembly of filopodia-like structures on supported lipid bilayers. (Translated from eng) *Science* 329(5997):1341-1345 (in eng).
15. Elliott HL, S. Chen, K. Lee, M. Mendoza, S. Besson, G. Danuser (2012) Quantification of image patterns in dynamic and variable cell shapes. *Submitted*.
16. Nayal A*, et al.* (2006) Paxillin phosphorylation at Ser273 localizes a GIT1-PIX-PAK complex and regulates adhesion and protrusion dynamics. (Translated from eng) *J Cell Biol* 173(4):587-589 (in eng).
17. Gardel ML*, et al.* (2008) Traction stress in focal adhesions correlates biphasically with actin retrograde flow speed. (Translated from eng) *J Cell Biol* 183(6):999-1005 (in eng).
18. Gupton SL, Eisenmann K, Alberts AS, & Waterman-Storer CM (2007) mDia2 regulates actin and focal adhesion dynamics and organization in the lamella for efficient epithelial cell migration. (Translated from eng) *J Cell Sci* 120(Pt 19):3475-3487 (in eng).
19. Rizvi SA*, et al.* (2009) Identification and characterization of a small molecule inhibitor of formin-mediated actin assembly. (Translated from eng) *Chem Biol* 16(11):1158-1168 (in eng).
20. Raucher D & Sheetz MP (2000) Cell spreading and lamellipodial extension rate is regulated by membrane tension. (Translated from eng) *J Cell Biol* 148(1):127-136 (in eng).
21. Houk AR*, et al.* (2012) Membrane tension maintains cell polarity by confining signals to the leading edge during neutrophil migration. (Translated from eng) *Cell* 148(1-2):175-188 (in eng).
22. Gauthier NC, Fardin MA, Roca-Cusachs P, & Sheetz MP (2011) Temporary increase in plasma membrane tension coordinates the activation of exocytosis and contraction during cell spreading. (Translated from eng) *Proc Natl Acad Sci U S A* 108(35):14467-14472 (in eng).
23. Sedzinski J*, et al.* (2011) Polar actomyosin contractility destabilizes the position of the cytokinetic furrow. (Translated from eng) *Nature* 476(7361):462-466 (in eng).
24. Mogilner A & Oster G (1996) Cell motility driven by actin polymerization. (Translated from eng) *Biophys J* 71(6):3030-3045 (in eng).
25. Machesky LM & Insall RH (1998) Scar1 and the related Wiskott-Aldrich syndrome protein, WASP, regulate the actin cytoskeleton through the Arp2/3 complex. (Translated from eng) *Curr Biol* 8(25):1347-1356 (in eng).
26. Choi CK*, et al.* (2008) Actin and alpha-actinin orchestrate the assembly and maturation of nascent adhesions in a myosin II motor-independent manner. (Translated from eng) *Nature cell biology* 10(9):1039-1050 (in eng).
27. Iskratsch T*, et al.* (2013) FHOD1 is needed for directed forces and adhesion maturation during cell spreading and migration. (Translated from eng) *Dev Cell* 27(5):545-559 (in eng).
28. Machacek M*, et al.* (2009) Coordination of Rho GTPase activities during cell protrusion. (Translated from eng) *Nature* 461(7260):99-103 (in eng).

29. Tkachenko E*, et al.* (2011) Protein kinase A governs a RhoA-RhoGDI protrusion-retraction pacemaker in migrating cells. (Translated from eng) *Nature cell biology* 13(6):660-667 (in eng).
30. Gutierrez E*, et al.* (2011) High refractive index silicone gels for simultaneous total internal reflection fluorescence and traction force microscopy of adherent cells. (Translated from eng) *PLoS One* 6(9):e23807 (in eng).
31. Butler JP, Tolic-Norrelykke IM, Fabry B, & Fredberg JJ (2002) Traction fields, moments, and strain energy that cells exert on their surroundings. (Translated from eng) *American journal of physiology. Cell physiology* 282(3):C595-605 (in eng).

Acknowledgements: K.L. was the recipient of Ruth L. Kirschstein NRSA Postdoctoral Fellowship from NIH. This work was funded by NIH grants GM071868 and GM098412. We thank Art Alberts for the gift of mDia2 antibody, Martin Schwartz for SNAP-tag-actin plasmids, J. Lim for helping with actin speckle imaging, A. Besser for providing the traction force microscopy software package, K. Jaqaman for the algorithm for segmentation of focal adhesions, and S. Besson for general software support. We thank J. Waters and Nikon Imaging Center at Harvard Medical School.

FIGURE LEGENDS

Figure 8. Traction force dynamics at the leading edge of migrating PtK1 epithelial cells. A, Positions (blue, early; red, late time points) of the leading edge of a PtK1 cell stained with CellMask Orange membrane marker undergoing a wound healing response. Inset: Overview of epithelial cell sheet with protruding region highlighted by yellow box. **B**, Protrusion (green to red colors) and retraction (green to blue colors) velocities tracked in edge sectors of 500 nm length. **C**, Normalized times since protrusion (green to red colors)/retraction (green to blue colors) onset for each sector tracked in (**B**). A value 0 means the sector starts to protrude/ retract. A value 1/-1 means the sector terminates a protrusion/retraction segment. Scale bars: 10 μm. **D-G**, Registration of spatially localized time series reporting molecular/cellular activities by motion event alignment. (**D**) Left: Quantification of cell edge motion and molecular/cellular activities in 500 by 500 nm probing windows tracking the cell movement (see also Supplementary Movie 3). Right: Space-time map of instantaneous edge velocity (top) and activity (in this example, normalized fluorescence) (bottom); each row represents the velocity and activity time series, respectively, of one probing window. Registration of velocity map (top) and activity map (bottom) with respect to retraction onsets (t=0) (**E**), protrusion onsets (t=0) (**F**), and maximal protrusion velocity (t=0) (**G**). **H**, Traction force magnitude map in a PtK1 cell with 1 by 1μm probing windows at the leading edge. Scale bar: 5 μm. **I**, Definition of a cell frame of reference in which probing windows track the leading edge. **J**, Definition of a laboratory frame of reference in which probing windows are placed at sites of protrusion initiation and remain stationary afterwards to track activities associated with newly formed adhesions. **K-O**, Traction force time series in cell or laboratory frames of reference registered with respect to retraction onset, protrusion onset or maximal protrusion velocity. **P-R**, Pearson's cross-correlation of

traction force and edge velocity as a function of the time lag between the two variables using time series acquired during retraction phases in the cell frame of reference (**P**), and time series acquired during early (from protrusion onset to 50 sec before maximal protrusion velocity), (**Q**) and overall (from protrusion onset to 50 sec after maximal protrusion velocity) (**R**) protrusion phases in the laboratory frame of reference. Inset: The gray areas indicate the periods of the time series used for correlation analysis. For each condition the number *n* of time series sampled in 9 cells pooled from 3 independent experiments is indicated. Solid lines indicate population averages. Error bands about the population averages indicate 95% confidence intervals computed by bootstrap sampling. Dotted lines indicate the significant correlation level with 95% confidence.

Figure 9. Recruitment of actin nucleators to lamellipodium. A-F, **J-O**, Normalized fluorescence intensity time series acquired in the cell frame of reference registered with respect to retraction onset, protrusion onset or maximal protrusion velocity. Time axis spans average duration of protrusion/retraction segments (see Fig. S7C and Fig. S8B). For each condition the number *n* of time series sampled in *m* cells pooled from multiple independent experiments (3 for actin, 4 for Arp2/3, 4 for mDia1, and 4 for mDia2) is indicated. Solid lines indicate population averages. Error bands about the population averages indicate 95% confidence intervals computed by bootstrap sampling. **G-I**, Immuno-localization of formins mDia1 (**C**), mDia2 (**D**), phalloidin-actin (**E**). Scale bars: 5 μm.

Figure 10. Roles of mDia1 in membrane protrusions of migrating epithelial cells. A, Pairwise Pearson's correlation coefficients of EGFP-mDia1- and SNAP-tag-TMR-actin-fluorescence intensity time series registered relative to protrusion onset (1148 time series from 9 cells pooled from 2 independent experiments). **B-D**, Scatter plots and Pearson's correlation

coefficients of mean normalized intensities of; mDia1 during retraction and of actin during protrusion (sample sizes as in Fig. 10A) (**B**); actin during retraction and actin during protrusion (sample sizes as Fig. 10A) (**C**), and mDia1 during retraction and Arp2/3 during protrusion (1716 time series from 11 cells pooled from 2 independent experiments). P-values are calculated using Fisher transformation; **E-F**, Positions (blue, early; red, late time points) of leading edge of cells stained with CellMask Orange membrane marker and treated with DMSO (control) (**E**) and 20 μM SMIFH2 (formin inhibitor) (**F**). Scale bars: 5 μm. **G**, Velocity vs. duration of individual protrusion segments in DMSO- (n = 950 segments from m = 9 cells pooled from 3 independent experiments) and SMIFH2- (n = 399 segments from m = 9 cells pooled from 3 independent experiments) treated-cells. **H**, Distance traveled by individual protrusion segments in DMSO- (n = 950 segments from m = 9 cells pooled from 3 independent experiments) or SMIFH2- (n = 399 segments from m = 9 cells pooled from 3 independent experiments) treated cells. **I-J**, Time series of Arp2/3 intensity in the lamellipodium, normalized to the Arp2/3 intensity in the region 1.5 – 2 μm from the cell edge, registered with respect to protrusion onset or maximal protrusion velocity in DMSO- or SMIFH2-treated-cells. (**I**) n = 556 time series sampled in m = 10 cells for DMSO and n = 602 time series sampled in m = 11 cells for SMIFH2, pooled from 3 independent experiments. (**J**) n = 1468 time series sampled in m = 10 cells for DMSO and n = 1467 time series sampled in m = 11 cells for SMIFH2, pooled from 3 independent experiments. **K**, Spatial modulation of Arp2/3 fluorescence at time point of maximal protrusion velocity in DMSO- and SMIFH2-treated cells as a function of distance from the leading edge. **L**, Normalized paxillin fluorescence intensity time series acquired in the cell frame of reference in DMSO- or SMIFH2-treated cells registered with respect to protrusion onset. n = 556 time series sampled in m = 8 cells for DMSO and n = 331 time series sampled in m = 11 cells for SMIFH2, pooled from 3

independent experiments. Solid lines indicate population averages. Error bands about population averages indicate 95% confidence intervals computed by bootstrap sampling.

Figure 11. Mechanosensitivity of Arp2/3 dynamics during cell protrusion. A-B. Protrusion segmental velocity in control cells vs. cells treated with , 400 μM Deoxycholate to decrease membrane tension (**A**) (*n* = 1950 time series sampled in *m* = 11 cells for control and *n* = 2555 time series sampled in *m* = 12 cells for Deoxicholate, pooled from 3 independent experiments) or cells treated with 1 μg/ml Concanavalin A to increase membrane tension (**B**) (*n* = 1796 time series sampled in *m* = 12 cells for control and *n* = 1995 time series sampled in *m* = 10 cells for Concanavalin A, pooled from 3 independent experiments). **C-D.** Time series of Arp2/3 intensity in the lamellipodium, normalized to the Arp2/3 intensity in the region 1.5 – 2 μm from the cell edge registered with respect to maximal protrusion velocity in control vs. Deoxycholate-treated cells (**C**) (*n* = 1040 time series sampled in *m* = 6 cells for control and *n* = 1448 time series sampled in *m* = 8 cells for Deoxycholate, pooled from 2 independent experiments) or control vs. Concanavalin A-treated cells (**D**)(*n* = 1095 time series sampled in *m* = 8 cells for control and *n* = 1054 time series sampled in *m* = 6 cells for Concanavalin A, pooled from 2 independent experiments). **E.** Average edge velocity between protrusion onset and maximal protrusion velocity vs. between maximal protrusion velocity and protrusion end in control vs. Deoxycholate-treated cells. **F.** Average edge velocity between protrusion onset and maximal protrusion velocity vs. between maximal protrusion velocity and protrusion end in control vs. Concanavalin A-treated cells. **G-H.** Normalized fluorescence intensity time series of mDia1 registered with respect to maximal protrusion velocity in control vs. Deoxycholate- vs. Concanavalin A-treated cells. (**G**) *n* = 1182 time series sampled in *m* = 8 cells for control and *n* =

1149 time series sampled in $m = 7$ cells for Deoxycholate, pooled from 2 independent experiments. (**H**) $n = 1089$ time series sampled in $m = 8$ cells for control and $n = 1325$ time series sampled in $m = 8$ cells for Concanavalin A, pooled from 2 independent experiments. Solid lines indicate population averages. Error bands about population averages indicate 95% confidence intervals computed by bootstrap sampling. **I**, Model of initiation and reinforcement of actin assembly during cell protrusions.

Figure 8

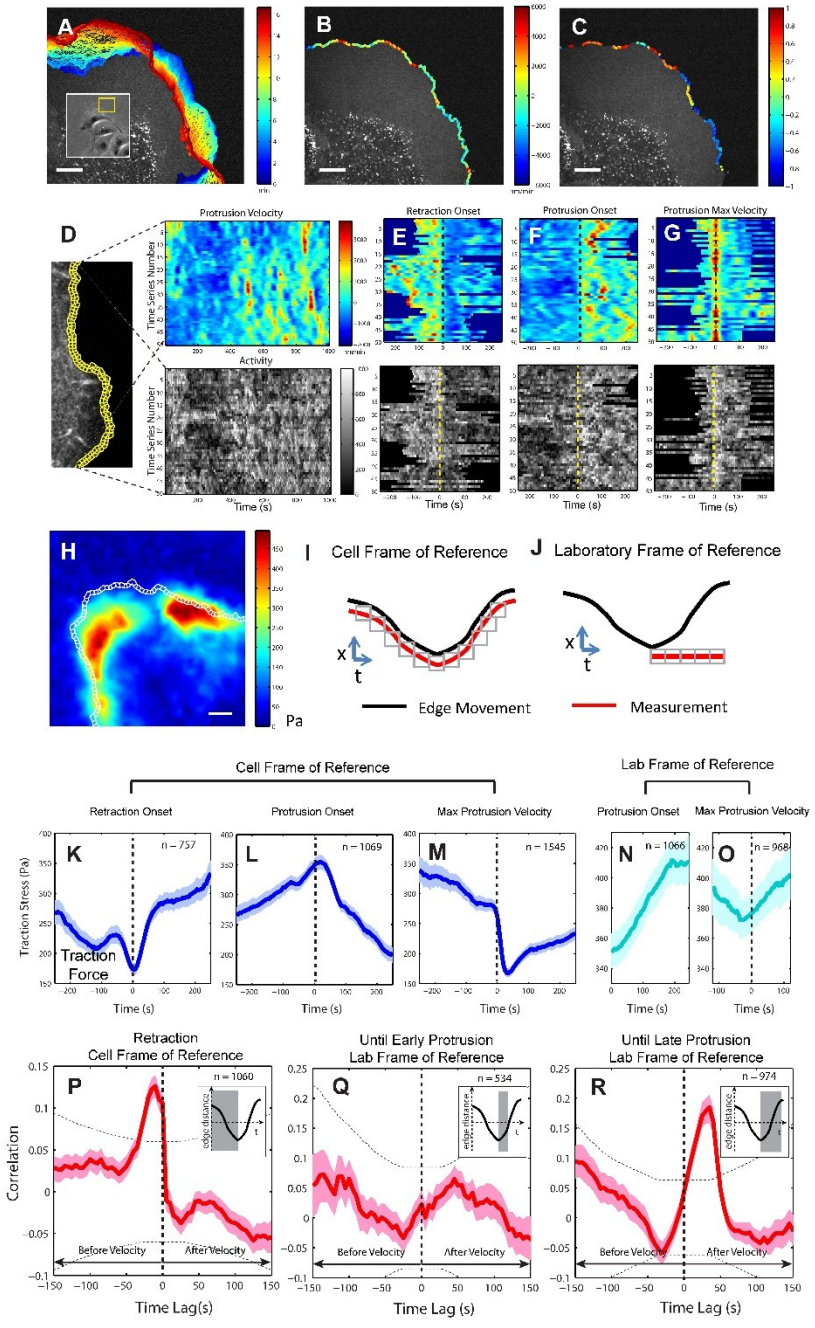
A
B
C
D
Protrusion Velocity
Retraction Onset
Protrusion Onset
Protrusion Max Velocity
E
F
G
Time Series Number
Activity
Time (s)
H
Pa
I Cell Frame of Reference
J Laboratory Frame of Reference
x
t
Edge Movement
Measurement
Cell Frame of Reference
Lab Frame of Reference
Retraction Onset
Protrusion Onset
Max Protrusion Velocity
Protrusion Onset
Max Protrusion Velocity
K
n = 757
L
n = 1069
M
n = 1545
N
n = 1066
O
n = 968
Traction Stress (Pa)
Traction Force
Time (s)
Retraction
Cell Frame of Reference
Until Early Protrusion
Lab Frame of Reference
Until Late Protrusion
Lab Frame of Reference
P
n = 1060
Q
n = 534
R
n = 974
edge distance
Correlation
Before Velocity
After Velocity
Time Lag(s)
Time Lag (s)

Figure 9

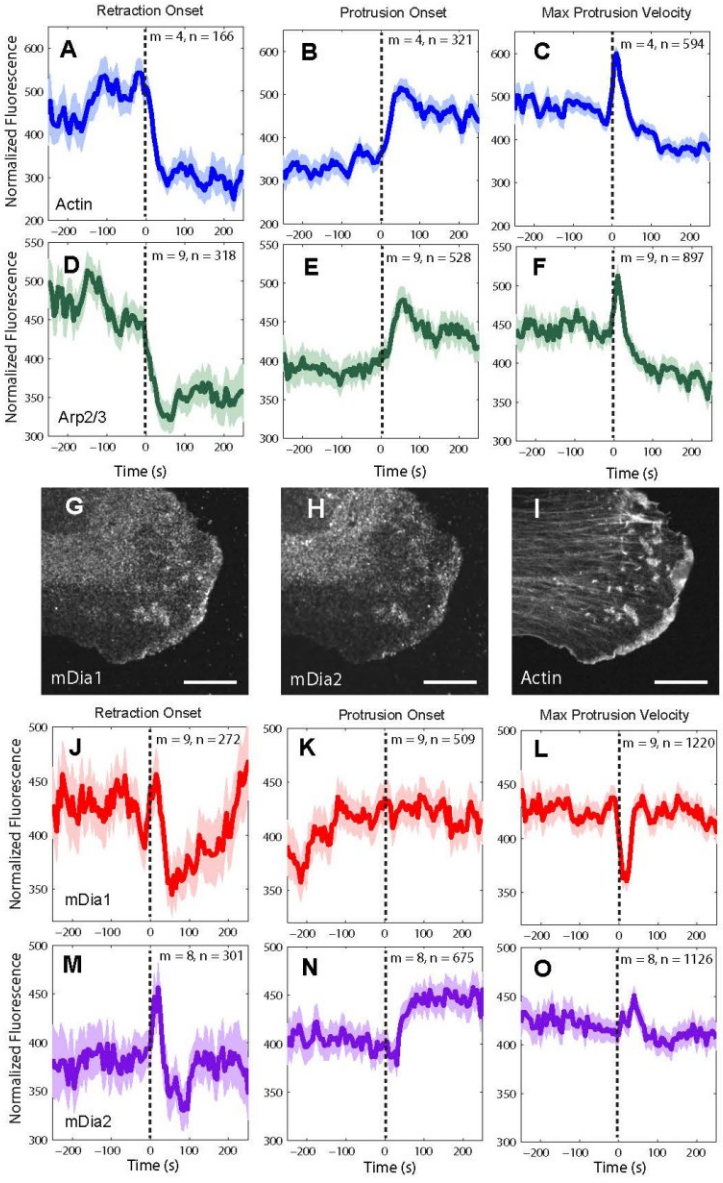
Retraction Onset
Protrusion Onset
Max Protrusion Velocity
A
m = 4, n = 166
Actin
B
m = 4, n = 321
C
m = 4, n = 594
D
m = 9, n = 318
Arp2/3
E
m = 9, n = 528
F
m = 9, n = 897
Normalized Fluorescence
Time (s)
G
mDia1
H
mDia2
I
Actin
J
m = 9, n = 272
mDia1
K
m = 9, n = 509
L
m = 9, n = 1220
M
m = 8, n = 301
mDia2
N
m = 8, n = 675
O
m = 8, n = 1126

Figure 10

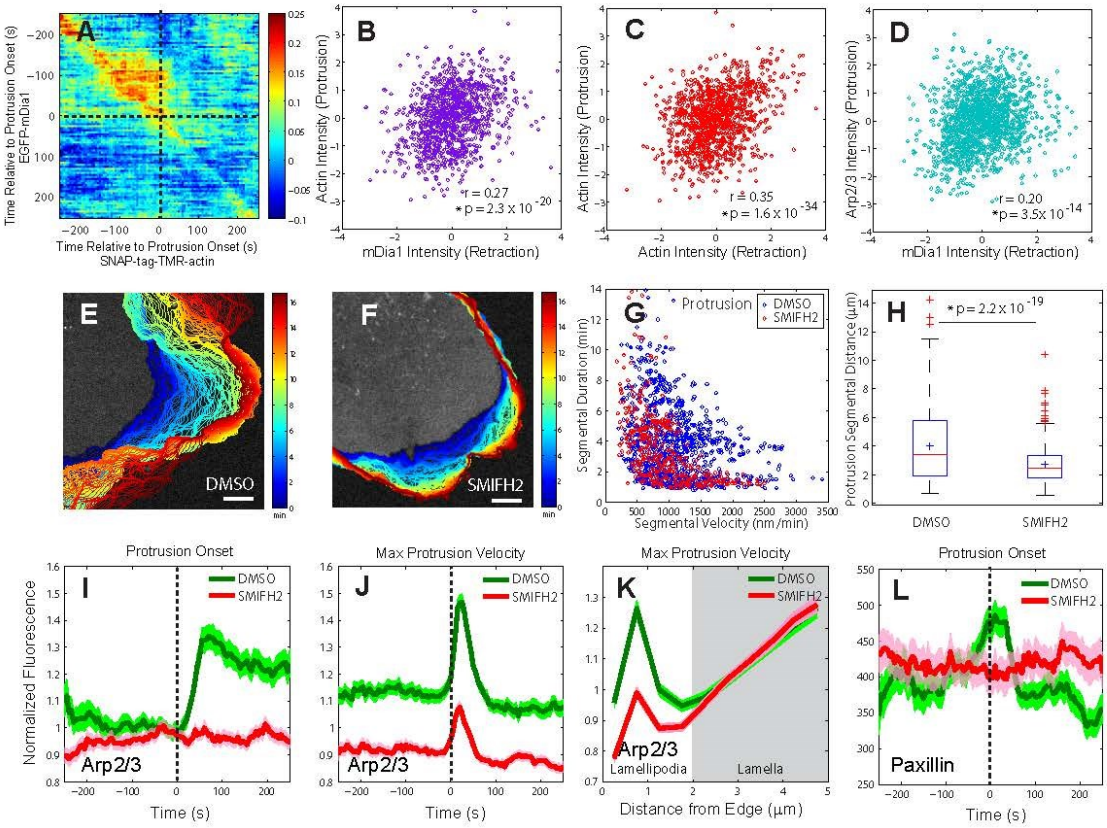
A
Time Relative to Protrusion Onset (s)
EGFP-mDia1
Time Relative to Protrusion Onset (s)
SNAP-tag-TMR-actin
B
Actin Intensity (Protrusion)
mDia1 Intensity (Retraction)
r = 0.27
*p = 2.3 x 10^-20
C
Actin Intensity (Protrusion)
Actin Intensity (Retraction)
r = 0.35
*p = 1.6 x 10^-34
D
Arp2/3 Intensity (Protrusion)
mDia1 Intensity (Retraction)
r = 0.20
*p = 3.5x 10^-14
E
DMSO
F
SMIFH2
G
Protrusion
DMSO
SMIFH2
Segmental Duration (min)
Segmental Velocity (nm/min)
H
*p = 2.2 x 10^-19
Protrusion Segmental Distance (µm)
DMSO
SMIFH2
Protrusion Onset
I
DMSO
SMIFH2
Normalized Fluorescence
Arp2/3
Time (s)
Max Protrusion Velocity
J
DMSO
SMIFH2
Arp2/3
Time (s)
Max Protrusion Velocity
K
DMSO
SMIFH2
Arp2/3
Lamellipodia
Lamella
Distance from Edge (µm)
Protrusion Onset
L
DMSO
SMIFH2
Paxillin
Time (s)

Figure 11

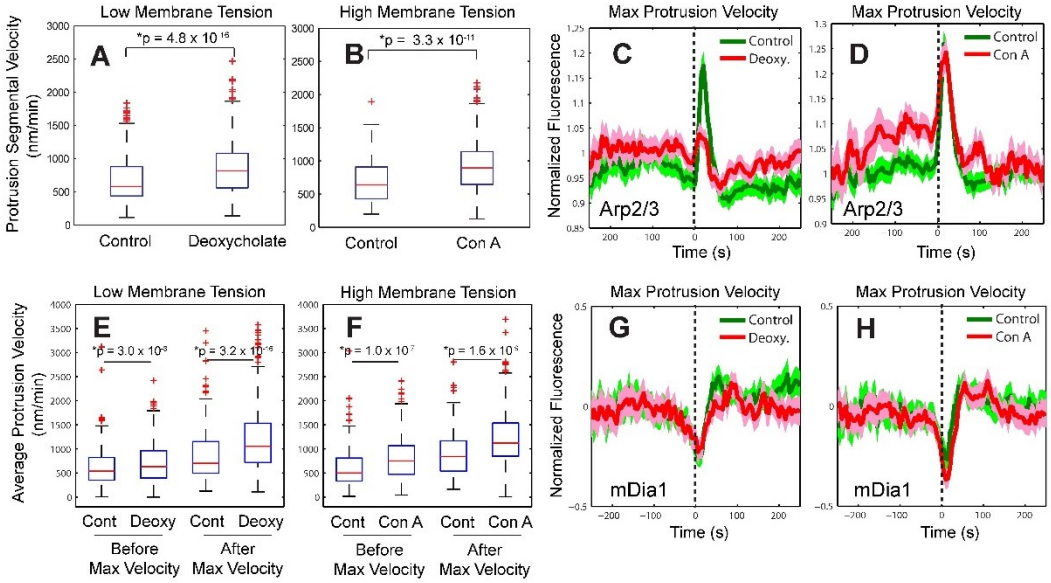
Low Membrane Tension
High Membrane Tension
Max Protrusion Velocity
Max Protrusion Velocity
Protrusion Segmental Velocity (nm/min)
A
B
C
D
*p = 4.8 x 10 -15
*p = 3.3 x 10-11
Control
Deoxycholate
Control
Con A
Normalized Fluorescence
Control
Deoxy.
Control
Con A
Arp2/3
Arp2/3
Time (s)
Time (s)
Low Membrane Tension
High Membrane Tension
Max Protrusion Velocity
Max Protrusion Velocity
Average Protrusion Velocity (nm/min)
E
F
G
H
*p = 3.0 x 10-9
*p = 3.2 x 10-6
*p = 1.0 x 10-7
*p = 1.6 x 10-3
Cont Deoxy Cont Deoxy
Before Max Velocity
After Max Velocity
Cont Con A Cont Con A
Before Max Velocity
After Max Velocity
Normalized Fluorescence
Control
Deoxy.
Control
Con A
mDia1
mDia1
Time (s)
Time (s)

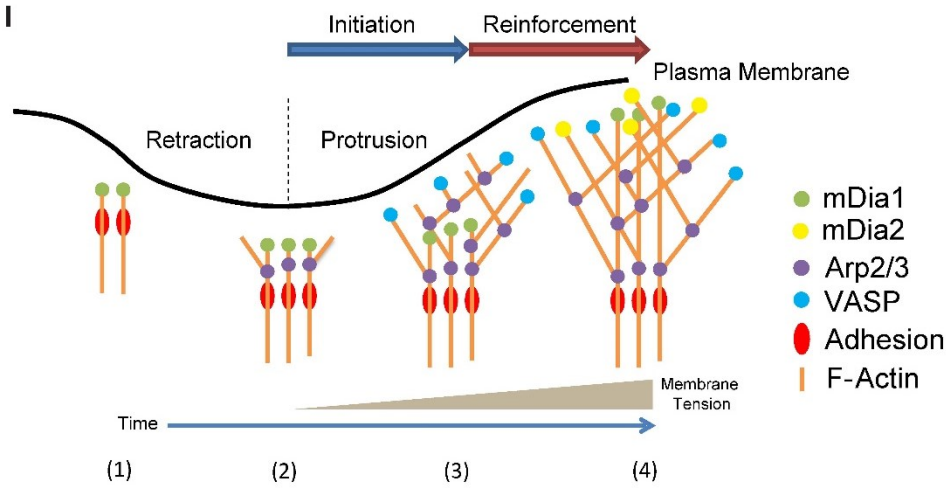
I
Initiation
Reinforcement
Plasma Membrane
Retraction
Protrusion
mDia1
mDia2
Arp2/3
VASP
Adhesion
F-Actin
Membrane Tension
Time
(1)
(2)
(3)
(4)

Appendix 3:
Traction force microscopy to identify force modulation in sub-resolution adhesions

Summary

Traction force microscopy (TFM) is a widely-used method for measuring the forces exerted at cell-matrix adhesions. The method has been limited to force detection in relatively large and strong adhesions because the underlying force reconstruction algorithms are sensitive to noise and tend to underestimate the force magnitude. Here, we present a TF reconstruction algorithm that overcomes these limitations and resolves forces within small nascent adhesions (NAs). The enabling numerical innovations we report include the introduction of a sparsity regularization technique to the solution of the inverse problem and application of sub-pixel correlation methods to map substrate deformation under the impact of cellular forces. Combining these advances with improved tracking of individual NAs, we show that the rate of load application to NAs determines the fate of NA maturation and therefore the spatial organization of cellular adhesions.

Contribution

My major contribution to this project was the design and execution of all live cell experiments. We wanted a set of experiments that would best show the features of the new algorithm, especially the ability to resolve forces within small nascent adhesions, and at the same time be able to make meaningful biological conclusions. By transfecting PtK1 cells with paxillin and performing traction force microscopy with an added paxillin channel, we were able to obtain time-lapse information of both traction stress and adhesion dynamics. This live cell experiment was instrumental in seeing that the force growth rate of a nascent adhesion in its earliest state determines its maturation into a focal adhesion and provided statistical evidence that the maturation of nascent adhesions is directly coupled to the development of the transmitted force.

Traction force microscopy to identify force modulation in sub-resolution adhesions

Sangyoon J. Han[1], Youbean Oak[1], Alex Groisman[2] and Gaudenz Danuser[1]

[1]Department of Cell Biology, Harvard Medical School, Boston, Massachusetts, USA,
[2]Department of Physics, University of California San Diego, La Jolla, California, USA

Introduction

Cell-matrix adhesions are mediated by engagement of integrins, which yields recruitment of additional adhesion proteins[1]. As adhesions assemble, mechanical forces generated by actomyosin contraction or propulsion of the growing actin meshwork are transmitted toward the extracellular matrix (ECM)[2]. These traction forces play an important role in promoting integrin signaling, environmental sensing, and directed migration[3,4]. Traction forces are not only the result of inside-out coupling of cytoskeletal activities to the ECM, but they are also the effector for adhesion maturation[5], as studied extensively at the level of large focal adhesions (FAs)[6]. How much force adhesions transmit during their nascent state and whether the fate of nascent adhesions (NAs) also depends on force transduction has remained unknown because of the technical difficulties of resolving traction forces in adhesion structures whose size is below the diffraction limit.

Traction forces exerted by cells onto their environment can be derived from the displacement of fluorescent beads embedded in deformable gel substrates[7], which requires the inversion of the deformation field into the generating force field as the critical numerical step. Such inverse problems are inherently ill-posed, i.e. relatively small noise contributions to the deformation field can generate out-of-bound force values. Pioneered by Dembo *et al.*[8], numerous algorithmic variants have been proposed to solve these issues and they have been used to study overall force distributions of migrating cells[4], the effect of mechano-chemical properties of the ECM on

cellular contractility[9], and overall contractility in diseased cells[10]. However, it has been physically and computationally challenging to resolve small forces from small adhesions because of noise in the bead tracking data and the spatial smoothing associated with the so-called regularization process that turns the ill-posed inverse problem into a stable force reconstruction[11,12]. In particular, the noise suppression works at the cost of a marked reduction of the force estimate on both large FAs and small NAs, with the result that most existing TFM maps significantly underestimate cellular forces and forces in NAs become indistinguishable from background[12].

Here, we innovate the TFM algorithm with L1-regularization[13], a numerical scheme that has recently found broad applications to inverse problems in the compressive sensing field[14] but has not been exploited for TFM. We show that L1-regularization enables the reconstruction of force fields without underestimation or spatial smoothing and with remarkably low background in the non-adhesion area. Together, this allows us to detect forces in small adhesions. We further improve the performance of the force reconstruction by reducing the noise in the raw measurement of the bead displacements by two orders of magnitude using subpixel correlation (SPC) tracking. Combining these computational advances with recent developments of TFM substrates that are compatible with high-resolution imaging of adhesions by total internal reflection fluorescence (TIRF) microscopy[15] and an image tracking algorithm that follows the temporal dynamics of NAs, we show that NAs exert small but significant forces on the substrate, and that the rate in force increase at individual NAs determines their fate of maturation.

Results

Improved accuracy in displacement field calculation using subpixel correlation (SPC) tracking

The accuracy in measuring bead displacements critically determines the accuracy in the force field calculation. With small forces exerted in small adhesion areas, displacements often fall below the noise level of conventional pixel correlation (PC) tracking[11]. Using synthetic bead images (Online Methods) we found that the uncertainty of PC tracking can reach up to 0.2 pixels (Supplementary Fig. 3a-e, Supplementary Note 1). To reduce this uncertainty, we implemented a subpixel correlation (SPC) tracking method that enhances the detection limit of bead displacements by two orders of magnitude over the existing methods (Supplementary Fig. 3e-i, Supplementary Note 2, Online Methods). Accordingly, this enhances the detection limit of forces in small adhesions (Supplementary Fig. 3j-u, Supplementary Note 3). SPC also allows the use of a smaller support area (template window) than PC, which permits finer resolution of spatial gradients in the displacement field (Supplementary Fig. 3v,w, Supplementary Note 4). Taken together, SPC shows clear superiority over PC in terms lower error, higher force detectability, and spatial resolution.

Ambiguity in the selection of the regularization parameter with L2-regularization

Once the displacement field is obtained, the force field is reconstructed by minimizing the difference between the prediction of the corresponding displacement field and the measured displacement field. The relation between force field and predicted displacement field is determined by a convolution of the former with the Greens function defining the displacement field generated by a unit force concentrated in one surface location of the deformable substrate

(Online Methods). Obtaining the force field out of the measured displacement field, or so-called the inverse problem is ill-posed, that is, small changes in the displacement field can produce vastly different force field reconstructions. A well-established remedy to this is the addition of a regularization term to the minimization problem, which penalizes large fluctuations in the force field. Specifically, the objective function that minimizes the norm of the difference between predicted and measured displacement fields, referred to as the residual norm, is complemented with the semi norm of the force field, e.g. its 0^{th} order (magnitude) norm. The relative importance of the two norms within the overall objective function is controlled by the regularization parameter λ[16] (Online Methods). To date, most TFM algorithms have used the Euclidian norm, or L2 norm, for minimization of both norms, which is referred to as Tikhonov regularization[8,12,16-18]. In nearly all TFM applications, the selection of λ has been subjective [2,19,20], despite the well-established L-curve criterion used in other fields to objectively set the regularization strength[16]. The L-curve relates the residual norm to the corresponding semi norm and the best λ-value is determined by the position along the curve where the combined differential between the norms is maximal (referred to as the L-corner).

To examine how susceptible the reconstructed force field is with respect to the choices of the regularization parameter and if the L-curve criterion can be used as a good reference with L2-regularization, we simulated bead images reflecting the deformation of a virtual substrate on which multiple force impact regions of varying sizes exert forces of varying magnitudes (Fig. 12a). We then measured bead displacements by SPC tracking, and solved the inverse problem with a range of regularization parameters using L2-regularization (Fig. 12b,d,e). The resulting L-curve displayed a convex shape with an L-corner (Fig. 12b). Although barely noticeable by the human eye, the L-corner could be found by numerical evaluation of the second derivative of the

semi norm with respect to the residual norm ($\lambda_{L\text{-corner}}$, Supplementary Fig. 4). The stress field determined with $\lambda_{L\text{-corner}}$ showed substantial underestimation of the stress magnitude compared to the simulated reference stress field (Fig. 12d), implying that for TFM using L2-regularization the L-corner criterion is not applicable. To estimate the optimal regularization parameter, we defined λ_{FGmin} that minimizes the reconstruction error in the force impact regions (Supplementary Fig. 5). The value of λ_{FGmin} (5.6×10^{-8}) was about 3-orders of magnitude less than that of $\lambda_{L\text{-corner}}$ (4.2×10^{-5}, Supplementary Fig. 5), and the stress field reconstructed based on λ_{FGmin} indeed showed values in the force impact regions comparable to the simulated reference stresses (Fig. 12e). However, λ_{FGmin} also increased the noise level in the background, including localized apparent forces with a magnitude similar to the forces generated by small force impact regions (Fig. 12e *inset, red arrowheads*). Thus, the choice of λ to minimize the error on large force impact regions (e.g. FAs) precludes the reconstruction of forces in small force impact regions (e.g. NAs). Another choice of λ_{BGmin} that minimizes background noise -- a criterion previous TFM studies relying on visual inspection for the definition of the regularization parameter may have used – also produced underestimated and distorted force maps (Supplementary Fig. 5, Supplementary Note 5). Together, we concluded that L2-regularization makes it difficult to choose the right regularization parameter: parameters derived from the L-corner or minimization of background stresses lead to strong under-estimation of the stress field, whereas a parameter derived from minimization of the error in adhesion stresses increases the background level, which obscures real forces from small adhesions.

L1-regularization avoids underestimation of force levels and is insensitive to background noise, thus lowering the detection limits for small and weak adhesions

A key feature of L1-regularization is that it performs favorably with sparse solutions[21]. Therefore, we hypothesized that L1-regularization, i.e. minimization of L1-norm of the semi norm (Online Methods), may be the more appropriate form of regularization for TFM as the majority of the traction force field is at the background level with a few sparsely located force impacts at discrete adhesions[13,22]. To test this, we reconstructed the stress field with a range of regularization parameters and examined L-curve and reconstruction accuracy (Fig. 12c,f). Contrary to L2-regularization, the L-curve associated with L1-regularization displayed a salient corner ($\lambda_{L\text{-corner}}$, Fig. 12c). Using $\lambda_{L\text{-corner}}$ for L1-regularization, stresses at both small and big force impact regions were restored to the level of the simulated input stress field (Fig. 12f,g). Moreover, compared to the reconstruction based on L2, λ_{FGmin}, the background force levels were small (Fig. 12f,h), which increases the likelihood of detecting weak forces in small impact regions (Fig. 12f, *inset, yellow arrow head*). Indeed, simulations with multiple force magnitudes applied in impact region of different sizes showed that L1-regularization affords a significantly lower detection limit for stress magnitude and force impact region size compared to that found in L2-regularization (Fig. 12i).

Of note the choice of $\lambda_{L\text{-corner}}$ as the regularization parameter yielded a best-matching stress field that preserved forces at NAs (Supplementary Fig. 6) even compared to force maps from regularization parameters that minimized force errors on either force impact regions or background (λ_{FGmin} or λ_{BGmin}, respectively). This indicates that L1-regularization provides an objective way to choose the best regularization parameter also in real-world experiments where the parameters λ_{FGmin} or λ_{BGmin} cannot be defined. Nonetheless, even with L1-regularization we found some small force impact region missing (Fig. 12f, *inset*, *white arrowhead*). In this case, the bead closest to the force impact was too distant to provide sufficient signal for a force

reconstruction in this region. Thus, the bead distribution remains a limiting factor for the detection of small force impact regions even with L1-regularization, but L1-regularization along with SPC tracking significantly enhances the resolution of TFM and removes subjectivity in the selection of the regularization parameter.

L1-regularization reveals NAs in a PtK1 cell exert independent forces

To assess the performance of L1 SPC TFM in reconstructing traction forces in live cell imaging experiments, especially at the sites of NAs, we filmed migrating PtK1 epithelial cells expressing TMR-paxillin on 8 kPa silicone gels with beads covalently-bonded on the top[15]. For testing spatial resolution, we used a single frame that contained a partial view of the protruding cell edge and compared the localization of adhesions as visualized by the paxillin channel image (Fig. 13a) with force maps that were reconstructed under L2-$\lambda_{L\text{-}corner}$ (Fig. 13b), L2- $\lambda_{optimal}$ (Fig. 13c) and L1 $\lambda_{L\text{-}corner}$ regularization (Fig. 13d). The regularization parameter $\lambda_{optimal}$ in L2-regularization was estimated by finding a parameter value that yielded a local minimum in the third-derivative of the L-curve, which was determined in a synthetic test to be close to the regularization parameter that minimized the reconstruction error on adhesions (λ_{FGmin}) (Supplementary Fig. 4). As expected, the overall stress magnitude obtained from L2-$\lambda_{L\text{-}corner}$ (Fig. 13b) was much lower than the one obtained from L2-$\lambda_{optimal}$ (Fig. 13c) or L1-$\lambda_{L\text{-}corner}$ (Fig. 13d). At the location of adhesions, the stress magnitudes obtained from L2-$\lambda_{optimal}$ and L1-$\lambda_{L\text{-}corner}$ were similar. However, the L1 displayed markedly less reconstruction noise in the background (Fig. 13c,d).

We examined in more detail a cell region rich in focal adhesions (FAs) (Fig. 13a, *box 1* and 13e) and a region rich in NAs (Fig. 13a, *box 2* and 13j). We developed an image segmentation method that differentially detected in the paxillin-channel focal complexes (FCs), FAs, along with the diffraction-limited NAs, and then co-localized the adhesions with the traction stress field (Fig. 13f,k, see Online Methods). In the FA-rich region, the stress field reconstructed by L2-$\lambda_{L\text{-corner}}$ was blurred and the stress magnitude substantially underestimated (~800 Pa at maximum; Fig. 13g). Both L2-$\lambda_{optimal}$ and L1-$\lambda_{L\text{-corner}}$ reconstruction showed much tighter co-localization with the adhesion sites and stress magnitudes reached maximal values of ~1600 Pa (Fig.13h,i). In the NA-rich region, L2-$\lambda_{L\text{-corner}}$ showed consistently low stress (~350 Pa at maximum) and lacked details in stress distribution (Fig. 13l). The stress field from L2-$\lambda_{optimal}$ showed a more prominent variation around the segmented NAs, with stress maxima reaching 600 Pa. However, the adjacent extracellular region displayed spikes in the background with magnitudes similar to those associated with NAs (Fig. 13m), making it difficult to distinguish bona fide stress values at NAs from random stress maxima induced by the regularization. The L1-$\lambda_{L\text{-corner}}$ reconstruction displayed background stress levels that were much lower than the stresses associated with NAs (Fig. 13n). We quantified these observations by comparing the stress magnitudes at the sites of NAs to the magnitude of local stress maxima in the background outside the cell (Fig. 13o). Although the forces at NAs were higher in magnitude than the background also in the L2-$\lambda_{L\text{-corner}}$ reconstruction (Fig. 13o), only ~20% of the NAs were associated with a local maximum in the force reconstruction (as opposed to ~60% in the L1-$\lambda_{L\text{-corner}}$ reconstruction; Fig. 13p). Simulations revealed that at the bead density used in these experiments, up to 13% of adhesions with small forces can be missed due to random bead distribution (Supplementary Fig. 7). These results and analysis suggest that more than a half of

NAs transmit independent forces that L2-regularization could not identify, and some (~27%) population of NAs might not be involved in force transmission. Furthermore, both L2-$\lambda_{optimal}$ and L1-$\lambda_{L\text{-}corner}$ reconstructions showed significant differences among the forces in NAs, FCs and FAs (Fig. 13q). However, the dynamic range of these differences is substantially higher with L1-based reconstruction. Together, these investigations document the limitation of L2-regularization in recognizing forces from NAs and propose L1-norm regularization as remedy.

Force growth rate of NA in its earliest state determines its maturation into a FA

Exploiting the enhanced resolution of the L1 SPC TFM, we studied force modulation at individual adhesions by tracking each NA (Supplementary Video 1, Online Methods). We tracked the forces in NAs that transitioned into FCs and eventually FAs (Fig. 14a) and in NAs that disassembled before maturation (average lifetime of ~2 minutes; Fig. 14b). Intriguingly, in NAs that underwent the maturation process the traction stress increased over time (Fig. 14c) whereas it remained constant in NAs that did not mature (Fig. 14d). Irrespective of the fate of the NA, the stress magnitude at the time point of NA appearance in the paxillin channel was significantly higher than stresses in the background or even stresses in the 1 μm vicinity outside the cell edge (Fig. 14e). Hence, forces measured in emerging NAs are above the noise level. In fact, they might be required for the assembly of NAs. A population analysis of failing vs. maturing NA tracks over the first two minutes of their lifetime (Fig. 14f) indicated that NAs that eventually mature undergo on average a two-fold higher rate in stress increase than failing NAs (Fig. 14g). They also start at higher stress levels (Fig. 14h), which suggests that sufficient tension – from probably actin retrograde flow – is a pre-condition for adhesion maturation. Together,

these data provide solid statistical evidence that the maturation of NAs is directly coupled to the development of the transmitted force.

Discussion

Our work demonstrates a significant computational improvement in traction force microscopy, which permits identification of forces in nascent adhesions. The key ingredients of this method are L1- regularization that does not underestimate forces while being insensitive to noise; and sub-pixel correlation (SPC) tracking of the substrate deformation which permits the use of smaller template windows for bead tracking and thus higher spatial resolution in the reconstruction. The robustness of L1-regularization arises from the underlying assumption of sparsity in the solution, i.e. instead of minimizing the magnitudes or derivatives of the solution the L1-norm tends to minimize the amount of non-zero coefficients in the solution[13]. L1-regularization has a fairly long history that goes back to the earliest numerical approaches to solving inverse problems[23]. However, it was only recently that L1-regularization was theoretically justified as equivalent to L0-regularization[13]. This led to a burst of applications of this regularization in MRI, electron tomography, network traffic and information technology[14]. Our results demonstrate that L1-regularization has also substantial advantages in TFM (Figs. 12 and 13), including increased fidelity in the estimate of force magnitude and impact location and the provision of an objective reference for selecting the regularization parameter (Fig. 12c). Hence, with the application of L1-based TFM it should now be possible to obtain reproducible and mutually comparable force fields.

Previous TFM studies have suffered from underestimation of the force magnitude and spatial smoothing of the force distribution. These limitations have been potentiated by an often arbitrary selection of regularization parameter, which can dramatically distort the reconstructed force

field. Nonetheless, these reconstructions seem accurate enough for the comparison of subcellular force gradients (e.g. front vs. back) on a relative scale [24], of whole-cell traction stress between cancer cells with different levels of malignancy[10], or of forces at large FAs in normal vs. vinculin knock-out cells[25]. In general, due to the limitations in reconstruction sensitivity, in the past TFM had to be limited to the analysis of forces at micron-sized FAs[20,25-27]. One of the interesting findings in these studies was the dependency of FA growth on tension, generated mainly by actin retrograde flow[6,27]. Whether this tension-dependency can be applied to early NAs has been impossible to show. Now with the greater sensitivity and precision of L1 SPC TFM, we could demonstrate that the fate of NA maturation correlates with the rate of tension increase (Fig. 14).

Our result is consistent with reports based on traction reconstruction using point forces (TRPF)[28]. As discussed by Sabass *et al*.[12], while TRPF seems an attractive approach to overcome some of the resolution limitations of regular TFM, it relies on the strong assumption that all adhesions generate forces. Our results show that only 60 % of NAs spatially coincide with local force maxima (Fig. 13p). Thus, constraining the locations of force transmission can lead to significant inaccuracy.

Although the application examples of this study focus on forces in NAs in order to showcase the gain in sensitivity and spatial resolution, L1 SPC TFM offers a more accurate resolution of force distributions in general. This will allow now for the systematic study of molecular mechanisms that regulate cell-matrix adhesion, from the earliest lay-down of NAs to their maturation into and disassembly of larger adhesion structures.

Acknowledgement

S.J.H is grateful to Sunyoung Ahn for support, encouragement and inspiration. The authors thank Hunter Eliot, François Aguet, Kwonmoo Lee, Assaf Zaritsky for helpful discussions. S.J.H., Y.O., A.G and G.D. are supported by National Institutes of Health Project Program Grant P01 GM098412.

Author contributions

S.J.H designed and implemented the algorithms for TFM and adhesion tracking, analyzed live cell data, and wrote the majority of the manuscript. Y.O. acquired live cell images of PtK1 cells and Alexa-Fluor 647-conjugated beads on gel surface. A.G. provided TFM gel substrates. G.D. initiated the study and helped edit the manuscript.

Online Methods

Software

TFM software featuring SPC bead tracking modules and force reconstruction based on L1 or L2 norm regularization is available as Supplementary Software 1 and at http://lccb.hms.harvard.edu/software.html; adhesion tracking software is also available at the same website.

Correlation-based tracking of substrate deformation

The displacement field was measured by tracking each bead via correlation-based image tracking between two images: an image reflecting the bead positions in the deformed substrate (f_{def}) and one reflecting the bead positions in a relaxed substrate (f_{und}) after release of cell

adhesions by trypsinization. As used in previous TFM studies[8,12,17], correlation –based tracking relies on the computation of a correlation score S between a static square template with side length $2L+1$ and placed at position (x_0,y_0) of a particular bead in f_{und} and a moving template of the same size that is initially placed in f_{def} at the same position (x_0,y_0) and then shifted pixel-by-pixel to positions $x_0 + u_x$ and $y_0 + u_y$, respectively:

$$S(f_{def},u_x,u_y)\big|_{x_0,y_0}=\frac{\sum_{i,j=-L}^{L}\left(I(f_{und},i,j)\big|_{x_0,y_0}-\bar{I}(f_{und})\right)\left(I(f_{def},i+u_x,j+u_y)\big|_{x_0,y_0}-\bar{I}(f_{def})\right)}{\sqrt{\sum_{i,j=-L}^{L}\left(I(f_{und},i,j)\big|_{x_0,y_0}-\bar{I}(f_{und})\right)^2}\sqrt{\sum_{i,j=-L}^{L}\left(I(f_{def},i,j)\big|_{x_0,y_0}-\bar{I}(f_{def})\right)^2}} \quad (1)$$

Here $I(f,i,j)|_{x0,y0}$ denotes the image intensity at pixel position $(x_0+ i,y_0+j)$ within the template derived from image f and $\bar{I}(f)$ is the mean intensity of the template. As shown previously[12], subtraction of the mean intensity and normalization of the correlation score relative to the intensity standard deviations eliminates effects from brightness variation between the images of the relaxed and deformed substrate.

The template size critically influences the position of the peak score. In an implementation of correlation-based tracking of fluorescent speckle flows, where the image contrast can be extremely heterogeneous, we optimized the template size for each speckle on the fly[29]. However, applied to TFM this would mean that displacement vectors across the field of view originate from a different level of granularity, which can introduce significant error in the force reconstruction. Thus, we maintained a fixed template size for all beads. In the case the score function computed at the default template size showed multiple strong maxima, we increased the template size until the ambiguity disappeared. We then returned to the default template size and searched among candidate peaks in the score function the one closest to the unique peak found at the larger template size. Subpixel localization of the maximal score value was accomplished by

parabolic fitting of the 9 score values about the maximum of the pixel-based score function. Of note, albeit the final displacement was thus defined with sub-pixel precision, we refer to this approach as pixel correlation (PC). This is in contrast to the subpixel correlation (SPC) approach, developed by Gui *et al*. for particle image velocimetry[30], which relies on linearly pre-interpolated templates:

$$S(f_{def}, Ru_x, Ru_y)\Big|_{x_0,y_0} = \frac{\sum_{i,j=-RL}^{RL} \left(I_R(f_{und}, i, j)\Big|_{x_0,y_0} - \overline{I}(f_{und})\right)\left(I_R(f_{def}, i+Ru_x, j+Ru_y)\Big|_{x_0,y_0} - \overline{I}(f_{def})\right)}{\sqrt{\sum_{i,j=-RL}^{RL} \left(I_R(f_{und}, i, j)\Big|_{x_0,y_0} - \overline{I}(f_{und})\right)^2} \sqrt{\sum_{i,j=-RL}^{RL} \left(I_R(f_{def}, i, j)\Big|_{x_0,y_0} - \overline{I}(f_{def})\right)^2}}, \quad (2)$$

where R is the refinement factor (e.g. 10) and I_R is an image enlarged by linear interpolation,

$$\begin{aligned} I_R(f,i,j) = (1-x)\cdot(1-y)\cdot I\left(f, i_R, j_R\right) + x\cdot(1-y)\cdot I\left(f, i_R+1, j_R\right) \\ +(1-x)\cdot y\cdot I\left(f, i_R, j_R+1\right) + x\cdot y\cdot I\left(f, i_R+1, j_R+1\right) \end{aligned}, \quad (3)$$

where i_R and j_R are the largest integers not greater than i/R and j/R, and x and y are the fractional part of i/R and j/R, respectively such that $i/R=i_R+x$, $j/R=j_R+y$. To minimize the increased computational cost associated with the image enlargement, we limited the range of u_x and u_y to $<u_{x,PC}-1, u_{x,PC}+1>$ and $<u_{y,PC}-1, u_{y,PC}+1>$, respectively, where $u_{x,PC}$ and $u_{y,PC}$ denote the position of the correlation maximum identified by PC. In SPC, the template window shifts by $1/R$. From the score, maximum peak was found and more precision was achieved by interpolation through parabolic fitting with nine points around the new peak. Other types of image interpolation methods, including cubic or spline interpolations were also tested using Matlab's 'griddata' function.

Our SPC is different from the approach described in Gui *et al.*[30] in that we interpolate the template window at both the images of relaxed and deformed substrate, whereas Gui *et al.* interpolated only the template derived from the target image (equivalent to the image of the

deformed substrate) and matched it with an non-interpolated template derived from the source image (equivalent to the image of the relaxed substrate). For TFM applications, it turns out that the latter produces a correlation score that is identical to the one from PC except for its refined shift in u_x and u_y, probably due to differences in bead density and diameter, image signal-to-noise between TFM and PIV.

Solution of inverse problem

2D TFM assumes that forces from cell adhesions on a gel are exerted in parallel to the gel surface, with negligible force in the normal direction[31]. Under these conditions the displacement field $\mathbf{u}(\mathbf{x})$ is the product of a convolution between the traction force field $\mathbf{f}(\boldsymbol{\xi})$ and a Green's function $\mathbf{g}(\mathbf{x},\boldsymbol{\xi})$:

$$u_i(\mathbf{x}) = \int_{\Omega} \sum_j g_{ij}(\mathbf{x},\boldsymbol{\xi}) f_j(\boldsymbol{\xi}) d\boldsymbol{\xi} \quad , \tag{4}$$

where Ω is the domain within the cell boundary, where traction is generated. Eq. 4 describes the substrate displacement in i-th direction at the location $\mathbf{x}=(x_1,x_2)$ as a result of the superposition of all the traction forces generated in Ω, where the contribution of a force in location $\boldsymbol{\xi}=(\xi_1,\xi_2)$ is defined by Green's function. Under the assumption of 2D TFM, Green's function is given by the Boussinesq solution[32]:

$$g_{ij}(\mathbf{x},\boldsymbol{\xi}) = \frac{(1+\nu)}{\pi E}\left[\frac{(1-\nu)\delta_{ij}}{|\mathbf{x}-\boldsymbol{\xi}|} + \frac{\nu(x_i-\xi_i)(x_j-\xi_j)}{|\mathbf{x}-\boldsymbol{\xi}|^3}\right], \tag{5}$$

where E denotes Young's modulus of the gel, ν denotes the Poisson ratio, δ_{ij} is the Kronecker delta function, and $|\mathbf{x}-\boldsymbol{\xi}|$ is the Euclidian distance between $\mathbf{x}$ and $\boldsymbol{\xi}$. To infer $\mathbf{f}(\boldsymbol{\xi})$ from a measured displacement field $\mathbf{u}(\mathbf{x})$, we used the boundary element method (BEM), which approximates a

force field on discrete nodes[8]. For each node we define a pyramidal-shaped basis function $\mathbf{h}(\mathbf{x})$ that is 1 in the node location itself and drops linearly to zero in all adjacent nodes. Hence the continuous force field is approximated by discrete force coefficients (β) as

$$f_j = \int_{\Omega} \beta_j h_j(x)\,dx \qquad (6)$$

allowing us to rewrite Eq. 4 as

$$u_i = \sum_{j=1}^{n} \beta_j \int_{\Omega} g_i(x) h_j(x)\,dx \qquad (7)$$

where n is the number of nodes in Ω. In this notation we can define a discrete forward map in matrix form

$$\mathbf{u} = \mathbf{M}\boldsymbol{\beta} \qquad (8)$$

with matrix coefficients

$$M_{i,j} = \int_{\Omega} g_i(x) h_j(x)\,dx \,. \qquad (9)$$

In this notation, $\mathbf{u}$ is a $2m\times1$ vector containing the displacement $\mathbf{u}_1$ and $\mathbf{u}_2$ of m beads and $\boldsymbol{\beta}$ is a $2n\times1$ vector containing the force coefficients $\boldsymbol{\beta}_1$ and $\boldsymbol{\beta}_2$ for x- and y- directions. For a general mesh, calculating $\mathbf{M}$ is computationally expensive. We simplified this process by creating an evenly spaced square mesh so that equation (9) can be transformed and calculated in the frequency domain. This is reminiscent of the approach taken in the Fourier Transform Traction Cytometry; however, we still solve the inverse problem in the spatial domain. Thus, we refer to this type of BEM as FastBEM.

The goal of traction force reconstruction is to solve Eq. 8 for $\boldsymbol{\beta}$, given a bead displacement field $\mathbf{u}(\mathbf{x})$. Due to measurement noise, the inversion of Eq. 8 is ill-posed (see main text).

Therefore, it is necessary to introduce a regularization scheme and solve a minimization problem of the kind:

$$\hat{\beta} = \underset{\beta}{\operatorname{argmin}} \left[\left\| \mathbf{M}\boldsymbol{\beta} - \mathbf{u} \right\|_2^2 + \lambda^2 \left\| \mathbf{R}\boldsymbol{\beta} \right\|_2^2 \right]. \qquad (10)$$

The first term in Eq.10 defines the residual norm between the measured and predicted displacement fields. The second term defines a semi norm, i.e. a norm of low-level spatial derivatives of the force coefficients that are encoded by finite differences in the matrix **R**. The regularization parameter λ determines how much the semi norm penalizes the minimization of the residual norm. For a semi-norm with 0^{th} order derivatives and a regular mesh, **R** is the identity matrix. **R** can also accommodate 1^{st} or 2^{nd} order derivatives of the force coefficients, which would implement the assumption that the spatial variation of the traction force field is small at the length scale of the mesh size. However, traction stresses are transmitted at discrete spots, which inherently large spatial variation. Accordingly, it has been shown before[12] that the use of a semi-norm with 0^{th} order derivatives better preserves punctate patterns of force impact. Thus, our implementation of TFM relies on 0^{th} order derivatives.

In general, TFM reconstructions have minimized the semi norm $\left\| \mathbf{R}\boldsymbol{\beta} \right\|_2$ (see Eq. 10), which is referred to as L2 regularization. In combination with 0^{th} order derivatives (**R**=**I**) in the semi-norm this type of regularization is known as Tikhonov regularization[16]. Tikhonov regularization suppresses the magnitude of the forces, leading to an inherent underestimation of the traction force level (see Fig. 12).

The regularization scheme involving minimization of $\left\| \mathbf{R}\boldsymbol{\beta} \right\|_1$ is called L1 regularization or sparsity regularization, which can be formulated with an objective function,

$$\hat{\beta} = \underset{\beta}{\operatorname{argmin}}\left[\left\|\mathbf{M}\boldsymbol{\beta} - \mathbf{u}\right\|_2^2 + \lambda\left\|\mathbf{R}\boldsymbol{\beta}\right\|_1\right]. \quad (11)$$

Ideal sparsity regularization would be minimizing $\left\|\mathbf{R}\boldsymbol{\beta}\right\|_0$ which is the number of nonzero entries in force coefficients $\boldsymbol{\beta}$ while minimizing the residual norm. However, this kind of optimization problem is extremely difficult to solve. L1 regularization (Eq. 11) has been proposed as a numerically feasible alternative to L0-regularization[33] that provides solutions close to the ideal L0-regularization. To solve Eq. 11, we used an iterative least squares method presented in Aster *et al.* [34]. It is worth noting that only because of our choice of the FastBEM, which solves the inverse problem in the spatial domain, is it possible to introduce non-linear regularization like the L1 norm. Other numerical schemes like the FTTC cannot accommodate non-linear regularization terms.

Force simulation for the generation of synthetic displacement fields

To validate the force reconstruction by synthetic data, we generated a circular area of radius r with force impact only in y-direction:

$$f_y(x,y) = f\exp\left(-\frac{\left((x-x_0)^2+(y-y_0)^2\right)}{2\sigma^2}\right)H\left(r^2 - \left((x-x_0)^2+(y-y_0)^2\right)\right). \quad (12)$$

Here, (x_0,y_0) denote the center position of the circle, f is the maximal stress in the center, and σ is the standard deviation of the Gaussian force distribution controlling the force gradient. For all simulations it was set to σ=1.1r. The purpose of introducing the Heaviside function H is to set the force to zero outside the circle. To test the effect of the template side length on force detectability, we chose an input stress f of 2 kPa and a force impact region diameter of 6 pixel. To test the effect of the force impact region diameter, an input stress f of 400 Pa was used.

Eventually we used a range of f (200 Pa – 4 kPa) and d (2 – 12 pixel) for force reconstructions under both L2-regularization and L1-regularization (see Fig. 12i).

Synthetic bead images were created by randomly placing 2D Gaussian image signals with normalized amplitudes varying from 0.3 to 1. The standard deviation of Gaussian was set to match a Gaussian approximation of the microscope point spread function[35]. The bead image of the deformed substrate was created with new bead positions calculated by forward Boussinesq solution in equation (4) for a given force distribution. With these two images, displacement field was measured using correlation-based tracking, and traction force fields were calculated based on L2 or L1 regularization. To validate the displacement measurements or force reconstructions, we defined the force detectability Ψ as

$$\psi = \frac{\left\| \bar{f}_{reconstr} \right\|_{@A_0}}{\max\left(\left\| \bar{f}_{reconstr} \right\|_{@A_{Background}} \right)} \qquad (13)$$

where the numerator is the average force in the circular force impact region (A_0), and the denominator is the maximal force magnitude among all forces in the background. The RMS error of the force reconstruction was estimated as $\zeta = \left\| \bar{f}_{reconstr} - \bar{f}_0 \right\|_2$.

For validations with multiple force impact regions, reflecting the presence of multiple adhesions, we first superimposed the force fields of all hypothetical adhesion sites and then continued with the same procedures for displacement field simulation and force reconstruction as discussed for the single force impact regions. To better reflect the co-existence of NAs and FAs, we introduced force impact regions with different sizes and different levels of anisotropy.

Nascent adhesion (NA) detection, focal adhesion (FA) segmentation, and adhesion tracking

NAs in paxillin images were detected using an existing algorithm from single particle tracking[36,37]. Briefly, TMR-paxillin images were filtered using the Laplacian of Gaussian filter followed by local maximum detection. Each local maximum was then fitted with an isotropic Gaussian function (standard deviation: 2.1 pixel) and tested with a goodness of fit test (p=0.05) for outlier removal. NAs and local force maxima were considered colocalized (Fig. 13p) if they were less than 0.5 μm apart, which is the length scale of the mesh used for force reconstruction. FA segmentation was performed based on a combination of Otsu and Rosin thresholding after image preprocessing with noise removal and background subtraction. Segmented areas were categorized as focal contacts (FCs) or FAs based on the area following the criteria prescribed by Gardel et al.[5] (0.24 μm^2 for FCs, 0.6 μm^2 for FAs). NAs ware tracked by the uTrack software[37] using gap closing option (maximum gap = 5 frames) and a Brownian search band of 2-5 pixels. Each track was examined to see if it overlapped with a FC or FA, and if so, the track was labeled as a maturing adhesion. Otherwise, the track was labeled as a failing adhesion.

Cell culture

PtK1 cells were grown in Ham's F-12 Nutrient Mix supplemented with 10% fetal bovine serum and 1% penicillin/streptomycin. The cells were cultured in humid atmosphere containing 5% CO_2 at 37°C.

Gel substrate preparation

Silicone gel substrates were prepared in glass-bottomed 35-mm dishes as described in Gutierrez *et al.*[15]. To facilitate cell adhesion, the substrates were coated with fibronectin (FN) by incubating with 50 μg/ml of FN and 100 μg/ml 1-Ethyl-3-(3-dimethylaminopropyl) carbodiimide

in PBS, pH 7.4 for 15 min at room temperature. The coated dishes were washed 3 times with PBS and filled with cell media before cell seeding. Cells were transfected with HaloTag-paxillin using the Neon Transfection System (Invitrogen, Carlsbad, CA, USA) right before being seeded. After 48 h in the incubator, cells were labeled by incubation with 5 μM HaloTag TMR ligand (Promega, Madison, WI, USA) for 15 min at 37°C with 5% CO_2. Cells were then washed three times with warm growth medium. After the final wash, cells were incubated in fresh growth medium for 30 min in the incubator to wash unbound ligands. Right before imaging, in order to protect cells from photo-damage during live imaging but allow for subsequent trypsin treatment, the imaging chamber was fitted with an inlet and an outlet tubing, sealed with Valap[38], and filled with imaging media – Leibovitz's L-15 medium (Life technology, Framingham, MA, USA) without phenol red supplemented with 1% penicillin-streptomycin, 10% FBS, 0.45% glucose and 1% oxyrase– using a 10-mL syringe.

Live cell imaging

Cells were imaged enclosed in a 37°C, 5% CO_2 incubation chamber. Images were taken on the 561 nm (paxillin TMR) and the 642 nm (beads) channels every 5 seconds with 500 ms exposure time for 200 frames on the Nikon Ti Total Internal Reflection Fluorescence (TIRF) at 90x magnification with Hamamatsu ORCA-D2 CCD camera (Hamamatsu Corporation, Bridgewater. NJ, USA, final resolution: 72 nm/pixel). To obtain a bead image from the undeformed substrate, cells were removed by injecting a high dose (0.5%) of 5 mL Trypsin/EDTA (Invitrogen) for 30 min.

Figures

Figure 12

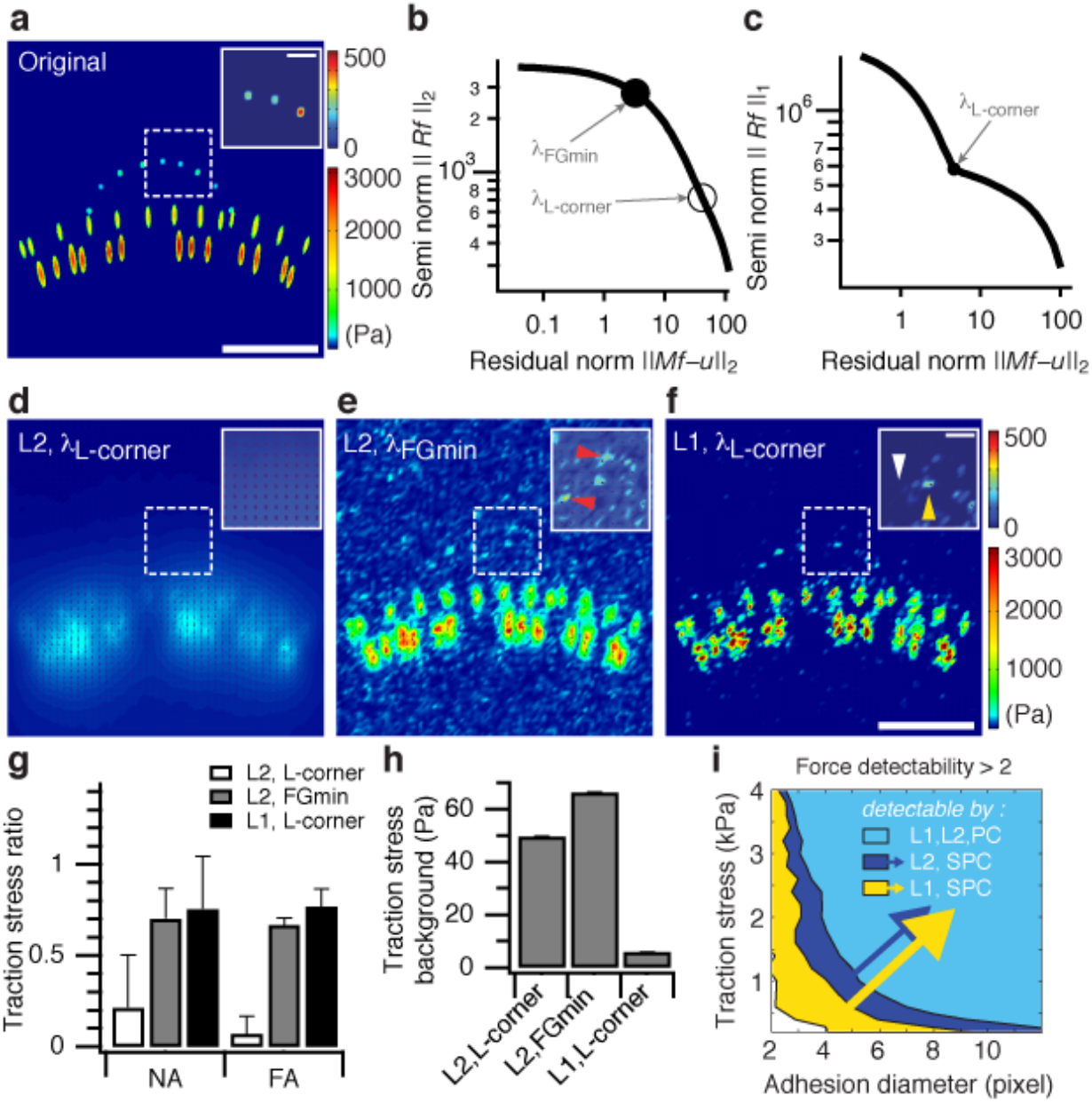

Figure 13

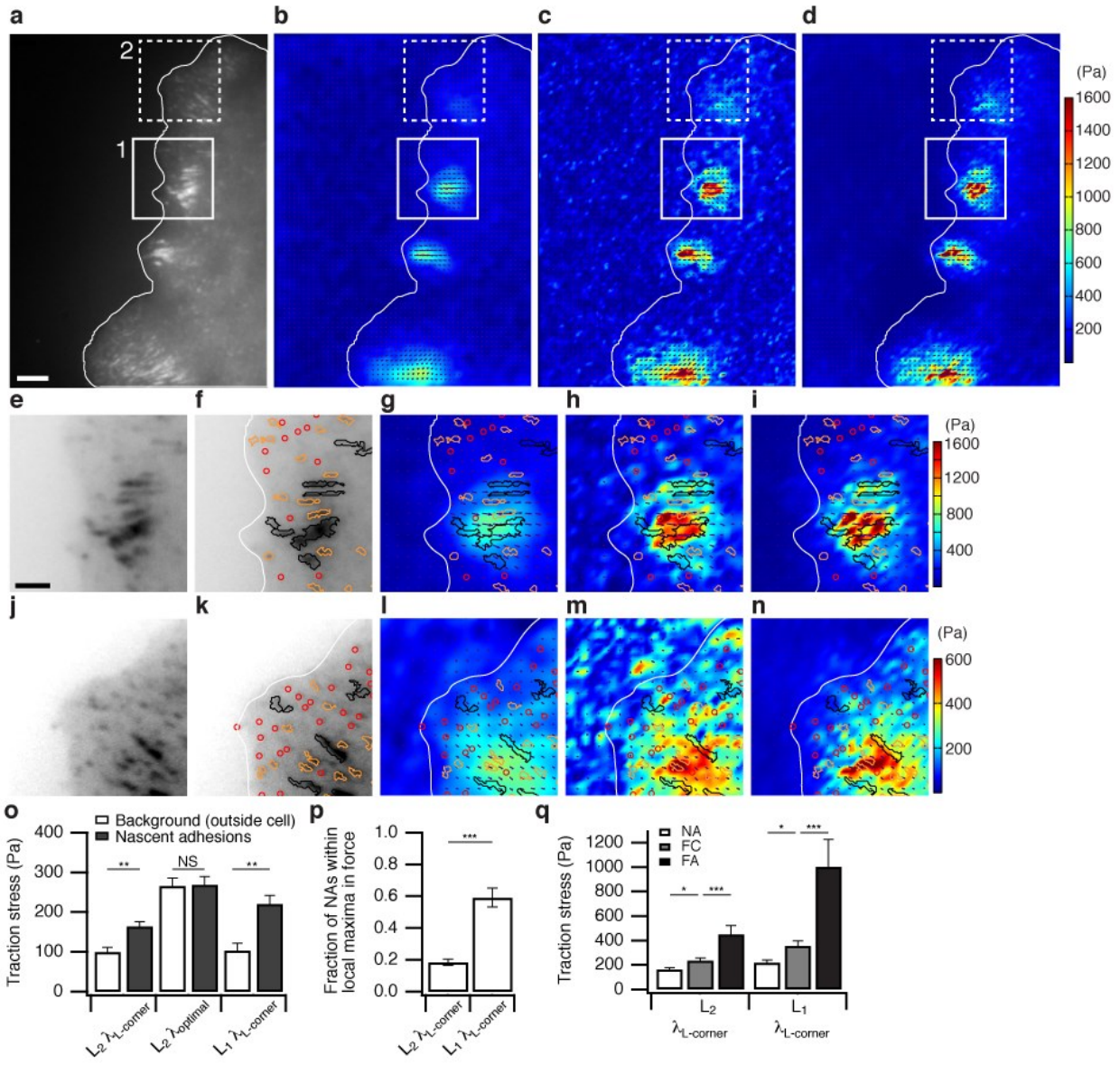
a
b
c
d
2
1
(Pa)
1600
1400
1200
1000
800
600
400
200
e
f
g
h
i
(Pa)
1600
1200
800
400
j
k
l
m
n
(Pa)
600
400
200
o
Background (outside cell)
Nascent adhesions
Traction stress (Pa)
400
300
200
100
0
**
NS
**
L2 λL-corner
L2 λoptimal
L1 λL-corner
p
Fraction of NAs within local maxima in force
1.0
0.8
0.6
0.4
0.2
0.0
***
L2 λL-corner
L1 λL-corner
q
NA
FC
FA
Traction stress (Pa)
1200
1000
800
600
400
200
0
*
***
*
***
L2
L1
λL-corner
λL-corner

Figure 14

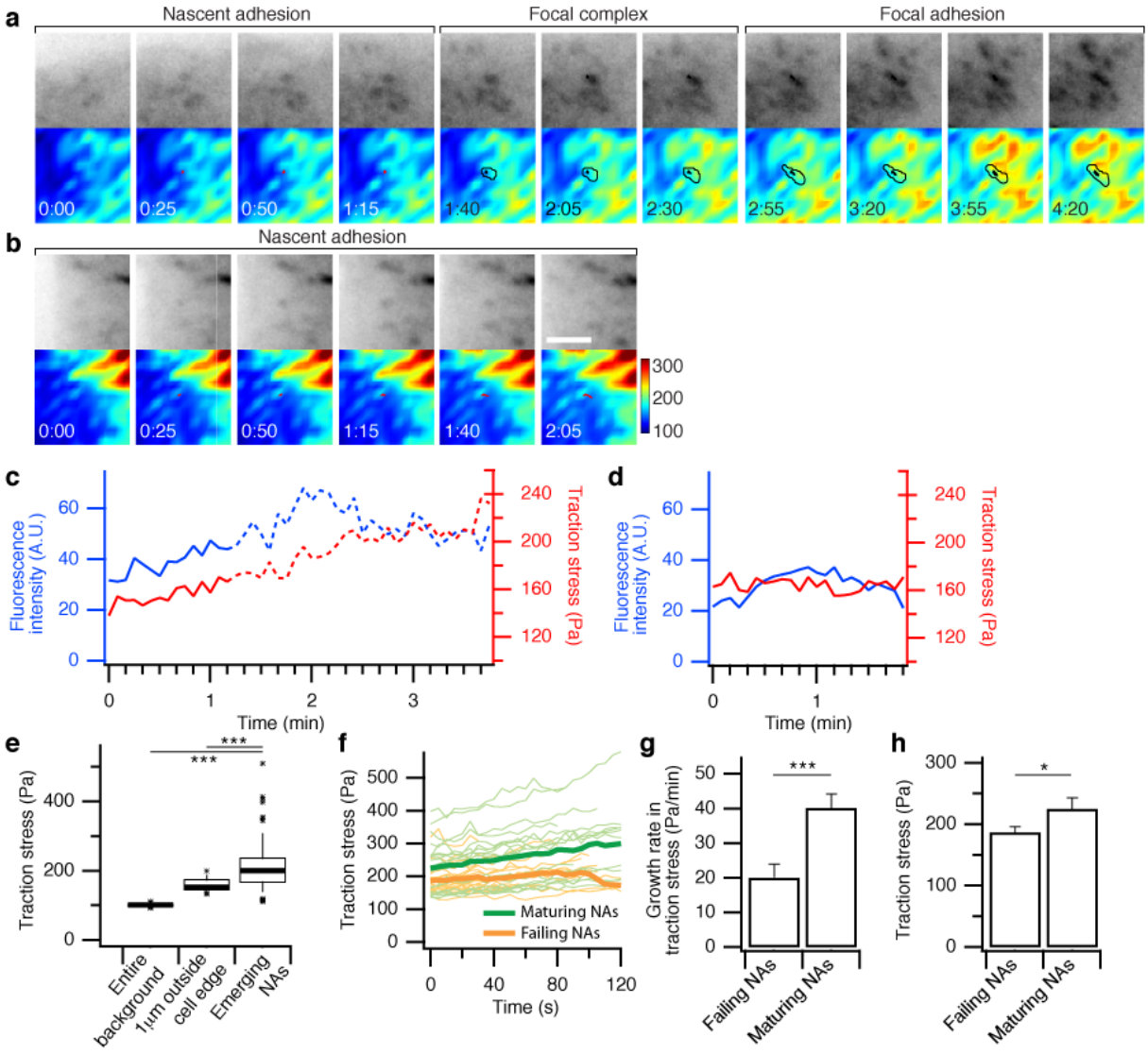
a
Nascent adhesion
Focal complex
Focal adhesion
0:00
0:25
0:50
1:15
1:40
2:05
2:30
2:55
3:20
3:55
4:20
b
Nascent adhesion
0:00
0:25
0:50
1:15
1:40
2:05
300
200
100
c
Fluorescence intensity (A.U.)
Traction stress (Pa)
Time (min)
d
Fluorescence intensity (A.U.)
Traction stress (Pa)
Time (min)
e
Traction stress (Pa)
***
***
Entire background
1μm outside cell edge
Emerging NAs
f
Traction stress (Pa)
Maturing NAs
Failing NAs
Time (s)
g
Growth rate in traction stress (Pa/min)
***
Failing NAs
Maturing NAs
h
Traction stress (Pa)
*
Failing NAs
Maturing NAs

Figure Legends

Figure 12 L-curve analysis for L2- and L1-regularizations. (**a**) Simulated input force field. Solid outlined inset: rescaled force map visualizing small force impact regions in a dashed window. (**b**) L-curve for L2-regularization. $\lambda_{L\text{-}corner}$ is determined by the second derivative of the semi norm with respect to the residual norm (Supplementary Fig. 4). The regularization parameter λ_{FGmin} is chosen to minimize the error in the force impact regions (Supplementary Fig. 5). (**c**) L-curve for L1-regularization. (**d**-**f**) Force maps reconstructed under L2, $\lambda_{L\text{-}corner}$ (**d**), L2, λ_{FGmin} (**e**), and L1, $\lambda_{L\text{-}corner}$ (**f**) regularization. Solid outlined insets: rescaled force maps in small force impact regions in dashed windows. Scale bar: 10 μm. (**g**) Traction stress ratio, i.e. magnitude ratio of reconstructed forces to the original forces in small force impact regions (NAs) and in large force impact regions (FAs). $n = 9$ for NAs, $n = 26$ for FAs; error bars show s.d. (**h**) Average traction stress background outside force impact regions. $n = 229{,}255$ pixels in non-adhesion area; error bars show s.e.m. (**i**) Regimes of traction stress detectability as a function of adhesion diameter (72 nm/pixel) and stress magnitude for reconstructions under L1 or L2 regularization combined with PC or SPC tracking.

Figure 13 Colocalization of traction forces with adhesions. (**a**) Snap-shot of HaloTag-TMR-paxillin at the leading edge of a protruding PtK1 cell. Scale bar: 10 μm. (**b**-**d**) Force maps reconstructed under L2, $\lambda_{L\text{-}corner}$ (**b**), L2, λ_{FGmin} (**c**), and L1, $\lambda_{L\text{-}corner}$ (**d**) regularization. See text and Supplementary Fig. 4 for determination of $\lambda_{optimal}$. (**e**-**i**) Colocalization analysis in FA-rich region (box 1 in **a**-**d**). (**j**-**n**) Colocalization analysis in NA-rich region (box 2 in **a**-**d**). (**e**,**f**,**j**,**k**) Inverted HaloTag-TMR-paxillin image without (**e**,**j**), and with (**f**,**k**) tracked NAs (*red circles*), FCs (*orange outlines*), and FAs (*black outlines*). Scale bar in **e**: 5 μm. See also Supplementary Movie 1. (**g**-**i**, **l**-**n**) Traction stress maps (overlaid by tracked adhesion regions) reconstructed under L2-$\lambda_{L\text{-}corner}$ (**g**,**l**), L2-$\lambda_{optimal}$ (**h**,**m**), and L1-$\lambda_{L\text{-}corner}$ (**i**,**n**) regularization. (**o**) Traction stress magnitude in NAs compared to the magnitude of local stress maxima outside the cell. $n = 10, 27, 14$ for background peaks in b, c, d, respectively, $n = 67$ each for NAs in b, c, d; error bars show s.e.m. (**p**) Fraction of NAs colocalized with local traction stress maxima in L2-$\lambda_{L\text{-}corner}$ and L1-$\lambda_{L\text{-}corner}$ reconstruction. $n = 7653$ NAs from 100 frames; error bars show s.e.m. (**q**) Traction stress in NAs, FCs and FAs reconstructed under L2-$\lambda_{L\text{-}corner}$ and L1-$\lambda_{L\text{-}corner}$ regularization. $n = 31, 68, 14$ for NAs, FCs, FAs, respectively; error bars show s.e.m. ***: $p < 0.001$, *: $p < 0.05$.

Figure 14 Live traction stress analysis in individual NAs of a PtK1 cell. (**a**,**b**) Time-lapse images of paxillin (*top*) and traction stress map reconstructed under L1 SPC TFM (*bottom*) for a maturing NA (**a**) and a failing NA (**b**), which are representative examples from all adhesion tracks in Supplementary Movie 1. Scale bar: 2 μm. (**c**,**d**) Fluorescence intensity (*blue*) and traction stress (*red*) as a function of time in **a**,**b**, respectively. (**e**) Comparison of traction stresses in emerging NAs ($n = 158$), in a 1 μm-wide band outside the cell edge ($n = 332$), and in the entire area outside the cell edge ($n = 735$). (**f**) Time courses of traction stress in maturing NA tracks (*green lines*, $n = 20$) and failing NA tracks (*orange lines*, $n = 23$;); thick lines represent average time course. (**g**,**h**) Comparison of rate of traction stress increase (**g**) and

traction stress magnitude in the time point of initial appearance (**h**) between failing NA tracks and maturing NA tracks. Sample numbers are the same as in **f**. ***: $p < 0.001$, *: $p < 0.05$.

Supplementary Figure 3

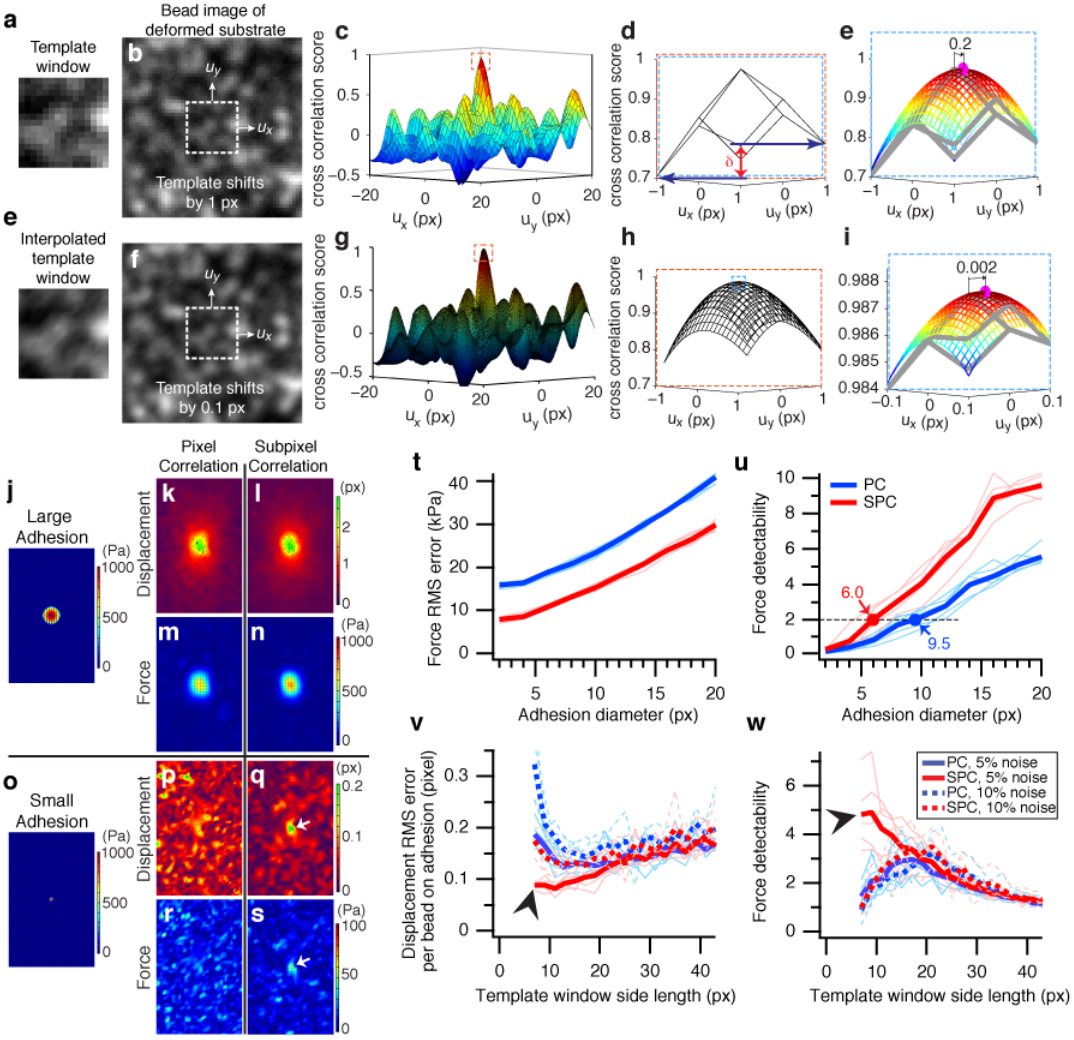

Supplementary Figure 3 Bead tracking by subpixel correlation (SPC). (a-e) Pixel-based correlation (PC) tracking process. (a) 15 × 15 pixel template window displaying beads in an undeformed substrate. (b) Beads in a deformed substrate; dashed box indicates a template window at (u_x, u_y) = (0,0). For cross-correlation score calculation the template window is shifted by 1 pixel over -20 ≤ u_x, u_y ≤ 20. (c) Cross-correlation score. (d) Scores in 3 × 3 neighborhood around the peak found in c (orange dotted box). (e) Interpolation of maximum score position using 3 × 3 neighborhood around the peak. Due to interpolation error, the peak of the parabola (magenta dot) is 0.2 pixel away from ground truth. (e-i) SPC tracking process. (e) 150 × 150 pixel template window resampled from a using linear interpolation. (f) 10-fold resampled images of beads in deformed substrate. Thus, 1 pixel shift of the template corresponds to 0.1 pixel shift in the original image. (g) Cross-correlation scores on 400 × 400 grid for the same range as in c. (h) Scores in 21 × 21 neighborhood around the peak, corresponding to the 3 × 3 neighborhood shown in d. (i) Interpolation of maximum score position using 3 × 3 neighborhood around the peak. The remaining interpolation error is 0.002 pixel. (j-s) Single force experiment with a large (20 pixel in diameter, j-n) and a small (4 pixel in diameter, o-s) force impact region. (j,o) Simulated force field. (k,l,p,q) Displacement field measured by PC (k,p) or SPC (l,q) tracking. (m,n,r,s) Force fields reconstructed from displacement fields in k,l,p,q, respectively. (t,u) force RMS error (t) and force detectability (ratio between peak force and maximum force in background, u) as a function of force impact region diameter for PC (*blue*) and SPC (*red*) tracking. Data from five different simulations; thick lines represent average for each condition. (v,w) Displacement RMS error (v) and force detectability (w) as a function of template window side length for PC tracking (*blue*) and SPC (*red*), and bead images with 5 % (*solid line*) and 10 % (*dotted line*) white noise. Arrowheads highlight exceptional performance of SPC in 5 % noise regime. See Supplementary Note 1 for details.

Supplementary Figure 4

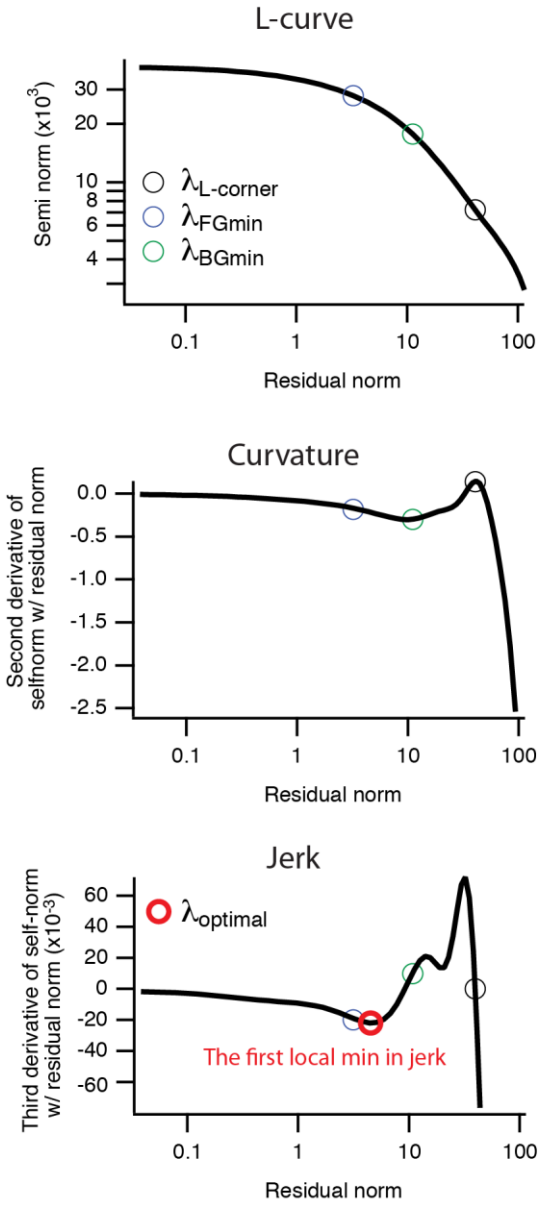

Supplementary Figure 4 Identification of L-corner and definition of $\lambda_{optimal}$ in L2-regularization. (Top) L-curve (the residual norm vs. semi norm in equation (10) in main text). Regularization parameters λ_{FGmin}, λ_{BGmin} are defined in a way that minimizes the force RMS errors on or outside force impact region. (Middle) Curvature (second derivative of semi norm with respect to residual norm). The regularization parameter that yields the maximum of the curvature is defined as $\lambda_{L\text{-}corner}$. (Bottom) Jerk (the third derivative of semi norm with respect to residual norm) defining $\lambda_{optimal}$ as the regularization parameter value producing the first local minimum.

Supplementary Figure 5

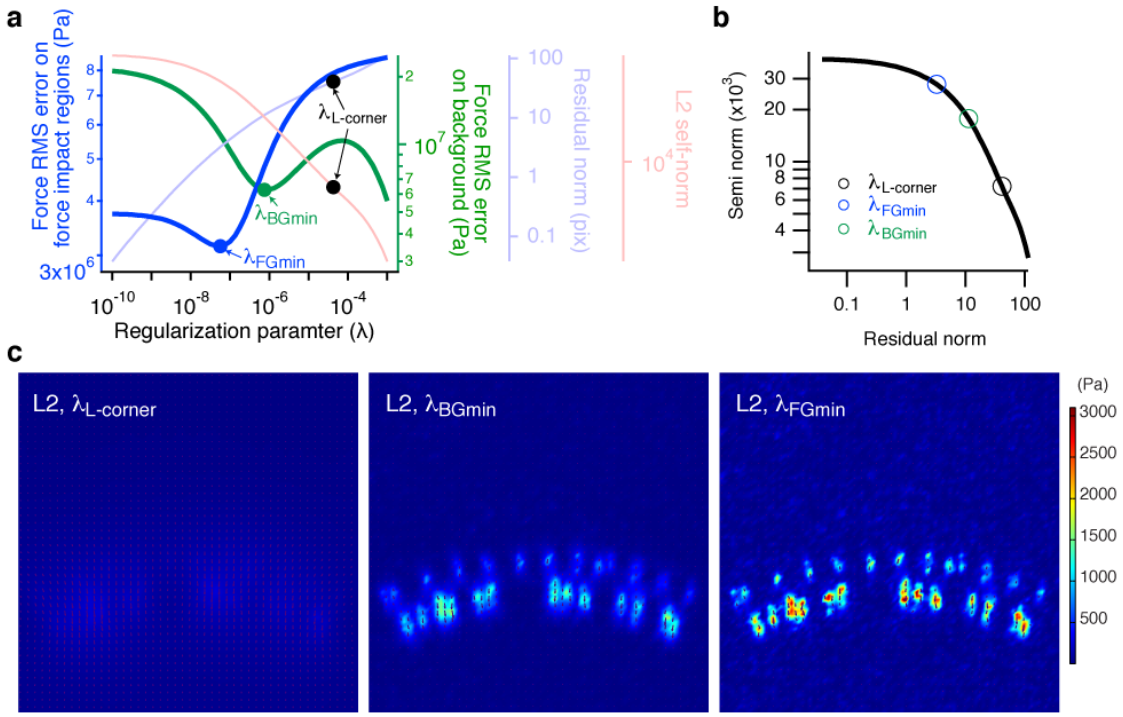

Supplementary Figure 5 L-curve analysis with $\lambda_{L\text{-corner}}$, λ_{BGmin}, and λ_{FGmin} in L2-regularization. (a) Log-scale plot of force RMS error on (blue) and outside (green) force impact regions, residual norm (light purple) and L2 self-norm (light red) as a function of λ. Local minima in force RMS error curves (filled circles) define λ_{FGmin}, and λ_{BGmin}. Black filled circles represent $\lambda_{L\text{-corner}}$ on residual norm and L2 self norm. (b) L-curve of L2-regularization. (c) Force maps by L2-regularization using $\lambda_{L\text{-corner}}$ (left), λ_{BGmin} (center), and λ_{FGmin} (right).

Supplementary Figure 6

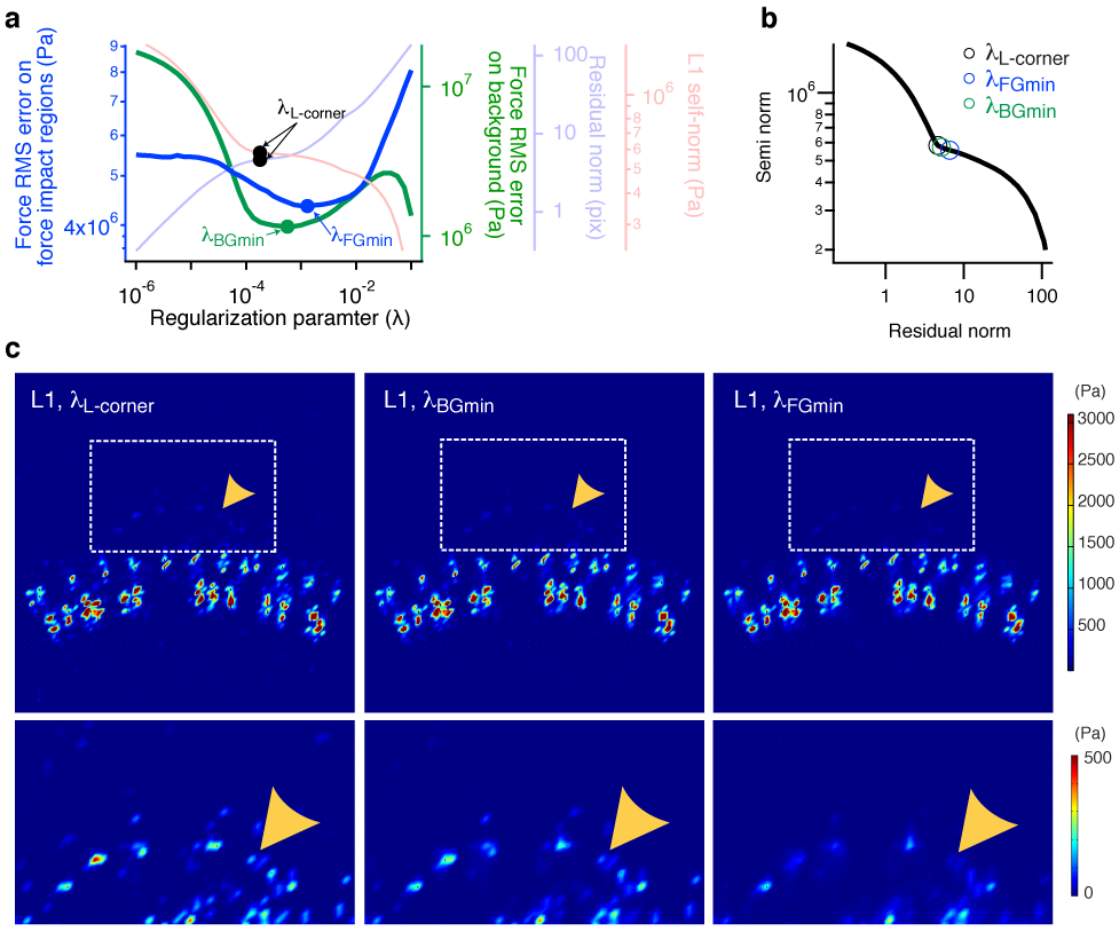

Supplementary Figure 6 L-curve analysis with $\lambda_{L\text{-}corner}$, λ_{BGmin}, and λ_{FGmin} in L1-regularization. (a) Log-scale plot of force RMS error on (blue) and outside (green) force impact region, residual norm (light purple) and L1 self-norm (light red) as a function of λ. Local minima in force RMS error curves (filled circles) define λ_{FGmin}, and λ_{BGmin}. Black filled circles represent $\lambda_{L\text{-}corner}$ on residual norm and L2 self norm. (b) L-curve of L1-regularization. Note that all $\lambda_{L\text{-}corner}$, λ_{BGmin}, and λ_{FGmin} are closely located. (c) Force maps by L1-regularization using $\lambda_{L\text{-}corner}$ (left), λ_{BGmin} (center), and λ_{FGmin} (right). For better visualization, the area with small force impact region (white dashed boxes) is enlarged and rescaled in bottom row. Close examination of the reconstructed force in one region (yellow arrowhead) reveals that force reconstruction under $\lambda_{L\text{-}corner}$ best restores forces in most small adhesions. Forces reconstructed under λ_{BGmin} and λ_{FGmin} are significantly underestimated.

Supplementary Figure 7

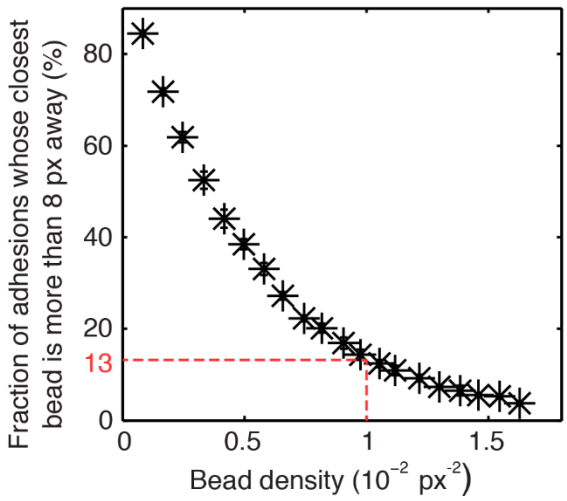

Supplementary Figure 7 Proximity of beads to small force impact region as a function of bead density on a gel. The distance threshold of 8 pixels is derived from the criterion that a small force (200 Pa) on an impact region of 8 pixels in diameter yields bead displacement of ≥ 0.1 pixels. That is, if there is no bead within 8 pixel radius, the force from this region may not be reconstructed. Pixel resolution is assumed to be 72 nm/px. Generation of random bead placement and random impact region placement was repeated 1000 times, after which the number of regions with at least one bead closer than 8 px were quantified using k-d tree-based nearest neighbor search. Red dotted line indicates our experimental bead density, which produces ~13 percent of adhesions with no force.

Supplementary Note 1. Conventional pixel correlation tracking generates subpixel noise

To test how much error can occur in our TFM setting, we created synthetic bead images in which Gaussian-profiled beads were randomly placed (Supplementary Fig. 3a). By applying a displacement calculated from a known force field, we also created a bead image of the deformed substrate (Supplementary Fig. 3b). To both images, we added a 5% white noise. Using these images, we calculated a displacement field of all detected beads in the images using conventional pixel-based correlation (PC) (Supplementary Fig. 3a-e). After a correlation score is computed on pixel-grid (Supplementary Fig. 3c), nine points (3x3 pixels) about the correlation maximum (Supplementary Fig. 3d) were used for parabolic fitting to interpolate the position of the maximum score and thus the template displacement shift with sub-pixel precision (Supplementary Fig. 3e). Even in the case of a zero displacement, i.e. using identical bead positions PC generates errors of up to 0.2 pixel due to asymmetry in the sub-sampled correlation scores (Supplementary Figs. 3d,e). This error was maintained or even increased when other fitting surfaces (e.g. Gaussian or cosinusoidal) were used for interpolation (data not shown).

Supplementary Note 2. Subpixel correlation (SPC) tracking produces less measurement uncertainty than pixel correlation (PC) tracking

The correlation peak is usually very sharp if small correlation window is used (Fig. 12a, c-e). Whereas the sharpness of the peak produces a more accurate tracking result at the pixel-level resolution, it causes larger uncertainty in the subpixel interpolation step [39]The interpolation accuracy increases with finer sampling of the score function about the peak position. To supply denser sampling, we applied subpixel correlation (SPC), in which both the reference (in the image of the relaxed substrate) (Supplementary Fig. 3e) and target (in the image of the deformed substrate) templates (Supplementary Fig. 3f) were enlarged by a factor of ten by linear interpolation. Accordingly, correlation scores can be calculated on a grid with a spacing of 0.1 pixel (Supplementary Fig. 3g) to generate ten−fold increase in sampling about the correlation peak (Supplementary Fig. 3h). A side effect of SPC is that the score function is also smoother than the one in PC. Thus, as second order approximation of the score function by a parabolic fit is appropriate to determine the sub-sampled location of the score maximum. We performed parabolic interpolation with only 9 points (0.3 x 0.3 pixel) around the peak, which yields an error of up to 0.002 pixel, two orders of magnitude smaller than the error in PC (Supplementary Fig. 3i). It is worth noting that linear interpolation of the image was tested to yield the best accuracy among linear, cubic and spline interpolation, and image enlargement by a factor larger than ten did not further improve the tracking result (data not shown).

Supplementary Note 3. Adhesion forces in small impact regions (<d=0.5 μm) are identifiable only by tracking with SPC

To investigate how the increased precision of bead displacement measurements by SPC boosts the resolution of forces from small adhesions vis-à-vis the forces derived from PC-based displacement measurements, we simulated a variety of stress fields containing a single circular area of force impact, or a force impact region. We varied the force magnitude and diameter of the area to synthesize bead images at rest and under load and tracked the deformation by PC or SPC (Supplementary Fig. 3j-w, Online Methods). We reconstructed the stress field using conventional TFM method[6,12] – L2 norm-based, 0th order regularization – with a constant regularization parameter in order to be consistent among all measured displacement fields. In the case of a large force impact region (e.g. d = 20 pix = 1.4 μm), displacements measured were similar for both PC and SPC (Supplementary Fig. 3k vs. 3l), and so did reconstructed force fields (Supplementary Fig. 3m vs. 3n). However, when a force with the same magnitude is applied over a small region (e.g. d = 4 pix = 0.3 μm, Supplementary Fig. 3o), the displacement field tracked by PC in the background had some spikes whose magnitudes were comparable to those found in the force impact region (Supplementary Fig. 3p). In contrast, SPC displayed significantly less displacement in the background, providing sufficient foreground to background contrast for detection of the original force impact (Supplementary Fig. 3q), and so did in reconstructed force maps (Supplementary Fig. 3r vs. 3s).

To assess the quality of each tracking method, we measured the root-mean-squared (RMS) error in the reconstructed stress relative to the simulated reference stress field (Supplementary Fig. 3t). As expected, the stress field reconstructed based on SPC tracking data was much more accurate than the one reconstructed based on PC tracking data. The RMS error increased with force impact region diameter because the number of non-negligible force vectors increased with increasing force impact area.

The force RMS error represents an overall deviation but does not quantify how much the force on the adhesion is above the forces on non-adhesion area. To quantitate this, we defined force detectability as the ratio between stress magnitude in the center of a force impact region and the maximal stress in the background (Online Methods). We determined the detectability for a range of force impact region diameters, each loaded with a constant stress of f = 400 Pa. While for both PC and SPC tracking methods the force detectability increased with the adhesion diameter (Supplementary Fig. 3u), the rate of increase was higher for SPC than for PC: Using SPC tracking data, stresses on a force impact region as small as 6 pixel or 0.43 μm were detectable at a foreground to background ratio of at least 2 whereas forces reconstructed from PC tracking data were only detectable in force impact regions bigger than 9.5 pixel or 0.68 μm in diameter (Supplementary Fig. 3u, arrows).

Supplementary Note 4. SPC allows for less correlation length that guarantees better accuracy in tracking

Correlation-based tracking of the bead displacements requires an optimal choice of the template size. Too large windows lead to over-smoothing of the displacement field, whereas too small windows are accompanied by ambiguity in tracking and higher susceptibility to image noise. To determine the optimal template size, we measured the RMS error of the displacement field on the force impact region – tracked with PC or SPC – for a range of sizes where 5 % or 10 % of white noise was added to synthetic bead images. The optimal template size with PC tracking was 15 pixels in 5 % noise (side length with lowest RMS; Supplementary Fig. 3v, *blue solid line*). Surprisingly, with SPC tracking the RMS error continually decreased with templates of a side length down to 7 pixels (Supplementary Fig. 3v, *red solid line*, *arrowhead*). This shows that, in a low noise regime (5%), SPC tracking reduces the ambiguity of the displacement measurement. In a high-noise regime (10%), the optimal template side length for SPC tracking was higher (13 pixel), but still less than the one for PC tracking (17 pixel side length), and the optimal SPC template generated significantly lower RMS error than the optimal PC template (Supplementary Fig. 3v, *dashed lines*). Hence, SPC tracking increases the precision and spatial resolution of the bead displacement field. Accordingly, in both the 5 % and 10 % noise regimes the force detectability over a range of template sizes was substantially higher when using SPC tracking (Supplementary Fig. 3w). With 5 % noise, SPC tracking yielded high force detectability at small template sizes (Supplementary Fig. 3w, *arrowhead*), implying that at reasonably low noise levels, SPC tracking provides excellent performance for tracking both large displacements in the force impact area while reducing subpixel uncertainties associated with very small displacements in the background.

Supplementary Note 5. Choice of a regularization parameter that minimizes the background error and its effect on force map

One could choose a regularization parameter subject to minimizing the force in the background. We suspect that most TFM studies, in which λ usually is set by visual assessment of the reconstructed stress field, target low stress levels in the non-adhesion area. We determined the regularization parameter λ_{BGmin} that minimized forces in the background and inspected the corresponding reconstructed stress levels in the simulated force impact regions (Supplementary Fig. 5). The value of λ_{BGmin} (7.5×10^{-7}) was more than an order of magnitude higher than that of λ_{FGmin}, but two orders of magnitude below $\lambda_{L\text{-}corner}$. Therefore, the stress magnitude at the force impact regions was under-estimated by 1.7 times compared to the stresses reconstructed based on λ_{FGmin} (Supplementary Fig. 5c, *middle*). Thus, background suppression not only interferes with the detectability of weak and small force impacts, but it markedly distorts the reconstruction of stresses in larger adhesion areas.

References

1 Geiger, B. & Bershadsky, A. Assembly and mechanosensory function of focal contacts. *Curr Opin Cell Biol* **13**, 584-592 (2001).

2 Gardel, M. L. *et al.* Traction stress in focal adhesions correlates biphasically with actin retrograde flow speed. *J Cell Biol* **183**, 999-1005, doi:10.1083/jcb.200810060 (2008).

3 Discher, D. E., Janmey, P. & Wang, Y. L. Tissue cells feel and respond to the stiffness of their substrate. *Science* **310**, 1139-1143 (2005).

4 Munevar, S., Wang, Y. & Dembo, M. Traction force microscopy of migrating normal and H-ras transformed 3T3 fibroblasts. *Biophys J* **80**, 1744-1757 (2001).

5 Gardel, M. L., Schneider, I. C., Aratyn-Schaus, Y. & Waterman, C. M. Mechanical integration of actin and adhesion dynamics in cell migration. *Annu Rev Cell Dev Biol* **26**, 315-333, doi:10.1146/annurev.cellbio.011209.122036.

6 Stricker, J., Aratyn-Schaus, Y., Oakes, P. W. & Gardel, M. L. Spatiotemporal constraints on the force-dependent growth of focal adhesions. *Biophys J* **100**, 2883-2893, doi:S0006-3495(11)00593-5 [pii] 10.1016/j.bpj.2011.05.023.

7 Han, S. J. & Sniadecki, N. J. Nanotechnology Usages for Cellular Adhesion and Traction Forces. *Cellular and Biomolecular Mechanics and Mechanobiology* **4**, 177-200, doi:10.1007/8415_2010_26 (2010).

8 Dembo, M. & Wang, Y. L. Stresses at the cell-to-substrate interface during locomotion of fibroblasts. *Biophys J* **76**, 2307-2316, doi:S0006-3495(99)77386-8 [pii] 10.1016/S0006-3495(99)77386-8 (1999).

9 Reinhart-King, C. A., Dembo, M. & Hammer, D. A. The dynamics and mechanics of endothelial cell spreading. *Biophys J* **89**, 676-689 (2005).

10 Paszek, M. J. *et al.* Tensional homeostasis and the malignant phenotype. *Cancer Cell* **8**, 241-254 (2005).

11 Westerweel, J., Dabiri, D. & Gharib, M. The effect of a discrete window offset on the accuracy of cross-correlation analysis of digital PIV recordings. *Experiments in Fluids* **23**, 20-28, doi:10.1007/s003480050082 (1997).

12 Sabass, B., Gardel, M. L., Waterman, C. M. & Schwarz, U. S. High resolution traction force microscopy based on experimental and computational advances. *Biophys J* **94**, 207-220, doi:S0006-3495(08)70780-X [pii] 10.1529/biophysj.107.113670 (2008).

13 Candes, E. J., Romberg, J. & Tao, T. Robust uncertainty principles: Exact signal reconstruction from highly incomplete frequency information. *Ieee Transactions on Information Theory* **52**, 489-509, doi:10.1109/tit.2005.862083 (2006).

14 Candes, E. J. & Wakin, M. B. An introduction to compressive sampling. *Ieee Signal Processing Magazine* **25**, 21-30, doi:10.1109/msp.2007.914731 (2008).

15 Gutierrez, E. *et al.* High refractive index silicone gels for simultaneous total internal reflection fluorescence and traction force microscopy of adherent cells. *PLoS One* **6**, e23807, doi:10.1371/journal.pone.0023807 PONE-D-11-07205 [pii] (2011).

16 Hansen, P. C. *Rank-deficient and discrete ill-posed problems : numerical aspects of linear inversion*. (SIAM, 1998).

17 Butler, J. P., Tolic-Norrelykke, I. M., Fabry, B. & Fredberg, J. J. Traction fields, moments, and strain energy that cells exert on their surroundings. *Am J Physiol Cell Physiol* **282**, C595-605, doi:10.1152/ajpcell.00270.2001 (2002).

18 Schwarz, U. S. *et al.* Calculation of forces at focal adhesions from elastic substrate data: the effect of localized force and the need for regularization. *Biophys J* **83**, 1380-1394, doi:S0006-3495(02)73909-X [pii] 10.1016/S0006-3495(02)73909-X (2002).

19 Beningo, K. A., Dembo, M., Kaverina, I., Small, J. V. & Wang, Y. L. Nascent focal adhesions are responsible for the generation of strong propulsive forces in migrating fibroblasts. *J Cell Biol* **153**, 881-888 (2001).

20 Plotnikov, S. V., Pasapera, A. M., Sabass, B. & Waterman, C. M. Force fluctuations within focal adhesions mediate ECM-rigidity sensing to guide directed cell migration. *Cell* **151**, 1513-1527, doi:10.1016/j.cell.2012.11.034 (2012).

21 Candes, E. J. & Romberg, J. Quantitative robust uncertainty principles and optimally sparse decompositions. *Found Comput Math* **6**, 227-254, doi:Doi 10.1007/S10208-004-0162-X (2006).

22 Parsons, J. T., Horwitz, A. R. & Schwartz, M. A. Cell adhesion: integrating cytoskeletal dynamics and cellular tension. *Nat Rev Mol Cell Biol* **11**, 633-643, doi:nrm2957 [pii] 10.1038/nrm2957 (2010).

23 Claerbou.Jf & Muir, F. ROBUST MODELING WITH ERRATIC DATA. *Geophysics* **38**, 826-844, doi:10.1190/1.1440378 (1973).

24 Munevar, S., Wang, Y. L. & Dembo, M. Distinct roles of frontal and rear cell-substrate adhesions in fibroblast migration. *Mol Biol Cell* **12**, 3947-3954 (2001).

25 Thievessen, I. *et al.* Vinculin-actin interaction couples actin retrograde flow to focal adhesions, but is dispensable for focal adhesion growth. *J Cell Biol* **202**, 163-177, doi:10.1083/jcb.201303129 (2013).

26 Stricker, J., Sabass, B., Schwarz, U. S. & Gardel, M. L. Optimization of traction force microscopy for micron-sized focal adhesions. *J Phys Condens Matter* **22**, 194104, doi:10.1088/0953-8984/22/19/194104 (2010).

27 Stricker, J., Beckham, Y., Davidson, M. W. & Gardel, M. L. Myosin II-mediated focal adhesion maturation is tension insensitive. *PLoS One* **8**, e70652, doi:10.1371/journal.pone.0070652 (2013).

28 Schafer, C. *et al.* The key feature for early migratory processes: Dependence of adhesion, actin bundles, force generation and transmission on filopodia. *Cell adhesion & migration* **4**, 215-225 (2010).

29 Ji, L. & Danuser, G. Tracking quasi-stationary flow of weak fluorescent signals by adaptive multi-frame correlation. *Journal of microscopy* **220**, 150-167, doi:10.1111/j.1365-2818.2005.01522.x (2005).

30 Gui, L. & Wereley, S. T. A correlation-based continuous window-shift technique to reduce the peak-locking effect in digital PIV image evaluation. *Experiments in Fluids* **32**, 506-517, doi:10.1007/s00348-001-0396-1 (2002).

31 del Alamo, J. C. *et al.* Three-dimensional quantification of cellular traction forces and mechanosensing of thin substrata by fourier traction force microscopy. *PLoS One* **8**, e69850, doi:10.1371/journal.pone.0069850 (2013).

32 Landau, L. D. & Lifshitz, E. M. *Theory of elasticity*. 3rd English edn, (Pergamon Press, 1986).

33 Bruckstein, A. M., Donoho, D. L. & Elad, M. From Sparse Solutions of Systems of Equations to Sparse Modeling of Signals and Images. *SIAM Rev.* **51**, 34-81, doi:10.1137/060657704 (2009).

34 Aster, R. C., Thurber, C. H. & Borchers, B. *Parameter estimation and inverse problems*. (Elsevier Academic Press, 2005).

35 Aguet, F., Geissbuhler, S., Marki, I., Lasser, T. & Unser, M. Super-resolution orientation estimation and localization of fluorescent dipoles using 3-D steerable filters. *Optics express* **17**, 6829-6848 (2009).

36 Aguet, F., Antonescu, C. N., Mettlen, M., Schmid, S. L. & Danuser, G. Advances in analysis of low signal-to-noise images link dynamin and AP2 to the functions of an endocytic checkpoint. *Dev Cell* **26**, 279-291, doi:10.1016/j.devcel.2013.06.019 (2013).

37 Jaqaman, K. *et al.* Robust single-particle tracking in live-cell time-lapse sequences. *Nature methods* **5**, 695-702, doi:10.1038/nmeth.1237 (2008).

38 Chazotte, B. Mounting live cells onto microscope slides. *Cold Spring Harbor protocols* **2011**, pdb prot5554, doi:10.1101/pdb.prot5554 (2011).

39 Prasad, A. K., Adrian, R. J., Landreth, C. C. & Offutt, P. W. EFFECT OF RESOLUTION ON THE SPEED AND ACCURACY OF PARTICLE IMAGE VELOCIMETRY INTERROGATION. *Experiments in Fluids* **13**, 105-116, doi:10.1007/bf00218156 (1992).